The Pennsylvania State University

The Graduate School

Department of Materials Science and Engineering

VELOCITY DEPENDENCE OF FATIGUE CRACK GROWTH MECHANISMS IN NANOCRYSTALLINE PLATINUM

A Thesis in

Materials Science and Engineering

by

Roi A. Meirom

Submitted in Partial Fulfillment

of the Requirements

for the Degree of

Master of Science

August 2008

The thesis of Roi A. Meirom was reviewed and approved* by the following:

Christopher Muhlstein
Assistant Professor of Materials Science and Engineering
Thesis Advisor

Donald Koss
Professor Emeritus, Materials Science and Engineering

Mark Horn
Associate Professor of Engineering Science and Mechanics

Gary L. Messing
Distinguished Professor of Ceramic Science and Engineering
Head of the Department of Materials Science and Engineering

*Signatures are on file in the Graduate School

ABSTRACT

Thin films are present in virtually every corner of industry, from holding our banking information on a thin magnetic strip, to lining the insides of our soda bottles as invisible diffusion barriers, to acting as switches and actuators in microelectromechanical systems (MEMS) barely visible to the naked eye. Material selection is of prime importance to the end-function of a thin film. Noble metals are a set of metals which have excellent resistance to oxidation, and their high electrical conductivity makes them ideal candidates for use in several MEMS applications. These applications often require the films to be mechanically loaded time and time again, and it is expected that they function reliably throughout their lifetime. The material's response to fatigue must therefore be evaluated in order to ensure that these thin films behave as expected.

Thin film mechanical testing specimens were fabricated as free-standing, 430nm platinum films having primarily (111) oriented columnar grains roughly 25-40 nm in diameter on a 20 nm titanium adhesion layer. These specimens had dog-bone geometry and a notch at the center of the gauge length, allowing for the localization of plastic deformation. The films were established to be fully dense (i.e. no voids or cracks) and no interphase regions between the grains were found. Further analysis confirmed purity of the platinum structural film within the detectability limits of the techniques. A tensile test conducted on one specimen established an upper bound for the ultimate tensile strength of 3.4 GPa, consistent with yield strength values found by nanoindentation and tensile testing studies conducted by others. Four constant stress amplitude (load ratio $\sigma_{min}/\sigma_{max}= R = 0.1$, sinusoidal waveforms at 1 Hz) fatigue tests were also conducted. An extremely limited range of stable fatigue crack growth was observed (< 3 MPa √m) as well as an order of magnitude reduction in K_{max} (4.88 MPa √m) when compared to microcrystalline platinum. The power law exponent , m, associated with the crack growth rates was ~10.5, significantly larger than the microcrystalline platinum at ~3. This study also shows that crack closure does not affect crack advance, and that at low crack growth rates, fatigue damage localizes at grain boundaries, creating intergranular failure surfaces, but transitions to a transgranular crack path at higher velocities. The limited span of stable

fatigue crack growth of the nanocrystalline platinum, in addition to the large m value suggests that the crack growth rate behavior of the nanocrystalline film is more similar to a ceramic or ordered intermetallic than that of a pure bulk metal. This research shows that the atomistic simulations and experimental observations of crack advance in nanograined metals may not be effectively generalized to other pure metal systems such as platinum.

TABLE OF CONTENTS

LIST OF FIGURES

LIST OF TABLES

ACKNOWLEDGEMENTS

First and foremost, my sincere thanks to my advisor, Christopher Muhlstein. His guidance provided the backbone for the research program and this thesis. Thanks, to the members of the Muhlstein research group for lending their assistance a myriad of times throughout the progress of this research. For funding, thanks is due to the Army Research Labs and the Army Research Office, and to their staff, specifically Madan Dubey, Ronald Polcawich, and Jeff Pulskamp for their hard work in fabricating the samples used in this study. Thanks to numerous Pennsylvania State University staff members, in particular, Mark Angelone and John Cantolina for help with the FE-SEM, Trevor Clark for this help with the TEM, EDS and EELS, Josh Meier for TEM prep, Scott Henninger, Eric Sagmuller and the Machine Shop staff for their help in creating and supporting lab equipment and Mike Fleck for his help in creating publishable quality images. Thank you to the committee members, Dr. Koss and Dr. Horn, who have not only taken the time to read through and comment on this thesis, but have also served as professors in classes which shaped my understanding of materials science. And lastly, thanks to my family, to my friends, and to Sarah, who have always supported me.

Chapter 1

Introduction

The first chapter in this thesis will open with a broad introduction to the world of thin films. First, thin films will be defined, and two of the most common methods to fabricate them will be overviewed. Thin film fabrication processes are directly tied to the structure of the films, and in turn their properties. Several techniques to measure properties such thickness, surface topography, grain boundary characterization, dislocations, and other defects such as voids, precipitates, crystallography and composition will be overviewed. To give a reader a sense of the importance and wide use of thin films, the second section of this chapter will list a variety of thin film applications from noteworthy fields of research and industry. These uses will center around the films' range of optical, electrical, magnetic, chemical, mechanical, and thermal properties and uses resulting from those properties. The mechanical behavior of nanocrystalline metallic thin films is the prime interest in this study; as a result the tensile response of micrograined ceramic and metallic materials will be discussed and will be compared to the tensile response of nanocrystalline metals. Following tensile response, a section detailing the fatigue response of micrograined ceramic and metallic materials will follow, with an analogous transition to a discussion of the fatigue nanocrystalline metals. Both mechanical response and testing techniques for the characterization of mechanical behavior will be overviewed. These discussions will highlight an apparent gap in the knowledge of the mechanical response of nanocrystalline thin films which is critical to the long term use and reliability of products which employ them, and will thus provide the motivation for this work. The last part of the chapter will provide an overview of the structure of the rest of this thesis.

1.1 General Properties, Processing and Structure of Thin Films

Thin films of one or more materials deposited on to substrates, on other thin films, or on their own, can have properties which their thicker, micrograined counterparts could never achieve. Their structure and functionality can be catered by changing the processing methodology and technique by which they are made. This allows thin films to attain a variety of useful properties which can in turn be used in a variety of applications. This section will provide a brief introduction to the general properties, processing methodologies and structures of thin films.

Although there is no accepted definition for a thin film, the definition that will adopted for this thesis is that a thin film is a film of any thickness that is produced by a deposition technique in which material from a source transfers individual atoms onto a surface. Techniques which involve liquid precursors and thus transfer molecules or groups of atoms onto a surface at a time will not be discussed. Similarly, techniques involving thermal sprays, which achieve similar transference from a gas phase will also not be detailed. The two most common methods of 'atom by atom' transference are chemical vapor deposition (CVD) and physical vapor deposition (PVD). Whereas CVD is the process in which a volatile gas phase chemically interacts with the deposition surface, PVD involves transference from the gas phase to the substrate by physical means (i.e. without chemical interaction) [1].

Sputtering is one physical vapor deposition technique in which highly accelerated ions and electrons are made to strike a solid source (Figure **1-1**). This bombardment causes atoms from the solid source to be ejected into the gas phase. Once in the gas phase, atoms are free to interact and settle on surfaces they come in contact with. This method can be precisely controlled by tailoring the amount of material ejected from the source (the sputter yield) by varying the source material, bombarding ion energies and masses and source temperature. Because of the kinetics of particle-particle interaction, virtually any material can be used as a sputtering source. Microstructure can be controlled through the use of masks, movement of the source or target, and the energies related to

the deposition impact. This technique is operable at a range of temperatures, creates uniform particle distribution over relatively large areas, and is comparatively cost effective [1].

The properties of the deposited thin films are in direct relation to their structure – this structure spans surface characteristics, to interior structure, to defects and bonding. These structural properties must be investigated in order to determine both the properties of the material system, and the effectiveness of the deposition technique in achieving the desired results with repeatable precision. Thickness is one geometrical component of specimens, and in thin films it is typically the smallest. Typical measurements of thickness for micrograined specimens must be scaled down in order to get an accurate measure of the thickness of thin films. One of the most basic ways to measure thickness in thin films is with the use of a stylus profiler which measures the stylus deflection as it is dragged across the surface of the film with up to 1 nm resolution. Interference oscillations can be used to analyze the thickness of transparent thin films. Ellipsometry can measure both refractive index and thickness of films and can even be applied to multistacked layers, but this is accomplished through mathematical fitting of generated models and is thus not a direct measure and the technique is limited by film opacity and substrate thickness. Eddy current measurements (most useful with conductive thin films on insulating substrates) relate the resistance of the film to its thickness. Cutting a film in a controlled manner such as using a focused ion beam and then studying the resulting cross section may be one the most precise ways to measure thickness, and is particularly effective in measuring the thickness of free floating thin films but it is a time consuming and destructive process [1].

Surface topography, or surface roughness, is also important in a variety of applications, especially in processes which involve thin film stacking. Roughness can be evaluated on qualitative scale using optical microscopy (useful for the detection of bubbles, hillocks and cracks), which is dependant on the wavelength of light and the technique in which light is shone on the surface (i.e. Nomarsky microscopy, optical interferometry etc.). Although optical microscopy can have the best contrast, scanning electron microscopy (SEM) can have significantly improved spatial resolution. In order

to determine the topography in a more quantitative way, the stylus profiler methodology mentioned previously (used to determine thickness) can be used. The atomic force microscope is a rastering stylus which can have a special resolution up to 0.1 nanometers and is commonly used to measure surface roughness in thin films [1].

Another application in which surface topography is critical is in the determination of specimen reflectivity and strain tracking. For example, digital image correlation (DIC) is a technique which allows for a non-contact, non-destructive measurement of strain by way of tracking the relative change of surface features of a sample in consecutive images. In typical tension tests, this method can be coupled with correlating values of stress in order to create stress-strain curves and determine a value of elastic modulus. Clearly, this method is dependant on the presence of optically visible features on the surface of specimens, and is more difficult in samples which have an optically smooth surface.

Characterization of the interior structure of a material can include inspection of crystallography, composition, and any disruptions to the ideal lattice structure such as grain boundaries, dislocations, voids, and precipitates. A generalized illustration of the operating physics behind several characterization tools is shown in Figure **1-2**. One technique for such analysis is X-ray diffraction (XRD). XRD uses the diffraction of X-rays from a sample (caused by incident X-ray radiation) to identify the atomic spacing of planes oriented perpendicular to the surface, degree of crystallinity elemental composition, and residual stresses. This is made possible by the fundamental principle that every element has a unique and distinguishable diffraction pattern as a result of the difference in the atomic properties of elements. Although the technique is more limited in the information it produces when compared to Transmission electron microscopy (TEM), it is typically cheap and fast to run and only minimally destructive. TEM is a technique which utilizes electrons transmitted through an electron transparent section of material (it is commonly necessary to thin down an existing material), allowing characterization of grain boundaries, dislocations and voids; this method can also be used to generate diffraction patterns, allowing the characterization of crystallography with sub nanometer resolution. Unfortunately, this technique usually requires extensive sample preparation which is both time consuming and destructive [1].

The measurement of the composition of a material is often crucial in explaining and predicting its mechanical behavior. There are several ways in which local and global chemical analyses can be performed. Energy dispersive X-ray spectroscopy (EDS or EDX) is one technique that can be used for elemental analysis on samples prepared for TEM. Much like XRD, it analyzes X-ray radiation, but unlike XRD, the X-rays are caused by an incident electron beam (instead of incident X-ray radiation). This technique is often paired with electron energy loss spectroscopy (EELS), as it is also a characterization technique ideally used on samples prepared in the same manner. EELS is based on the principle that a material is exposed to a beam of electrons with a known energy will alter the state of energy of the scattered electrons. The amount of energy loss is measurable and directly tied to an elemental cause. An additional way to determine surface composition is with secondary ion mass spectroscopy (SIMS) which uses sputtered ions to characterize the material they were emitted from. SIMS can be combined with destructive sputtering in order to determine the composition of the film through its thickness. Further details of these tools and their use in characterizing the material reported in this thesis will be detailed in Section **2.1.2**. Other important properties of materials are directly tied to their uses. The following section will detail several thin film properties and their uses in industry [1].

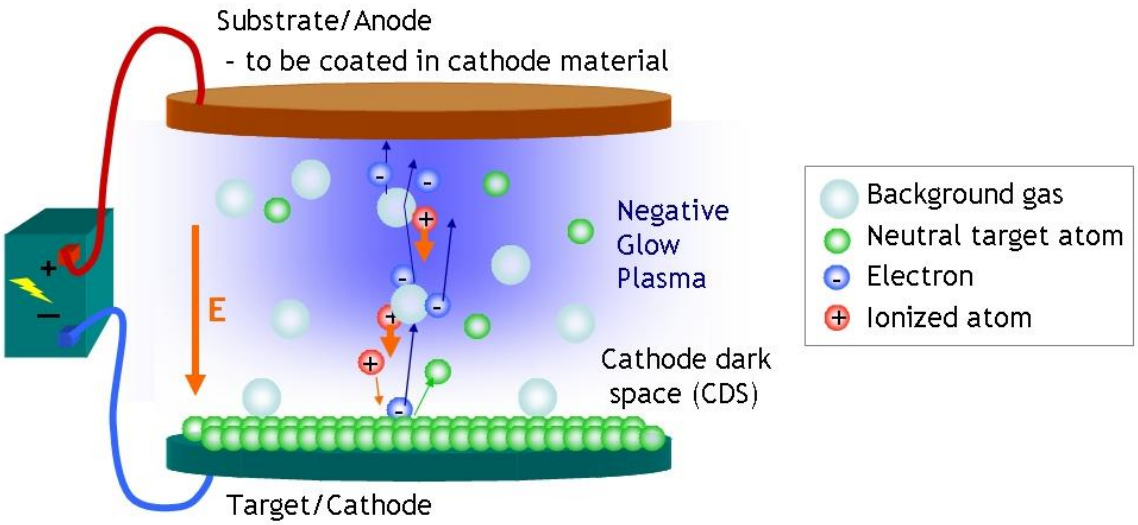

Figure **1-1**: Schematic of a DC plasma sputtering system. The schematic shows electrons and ionized atoms accelerated towards the target, which is made of the source material used in coating the substrate. This resulting impact dislodges target atoms which adhere to the substrate/film. This image was slightly modified from one created for the Opensource Handbook of Nanoscience and Nanotechnology [2].

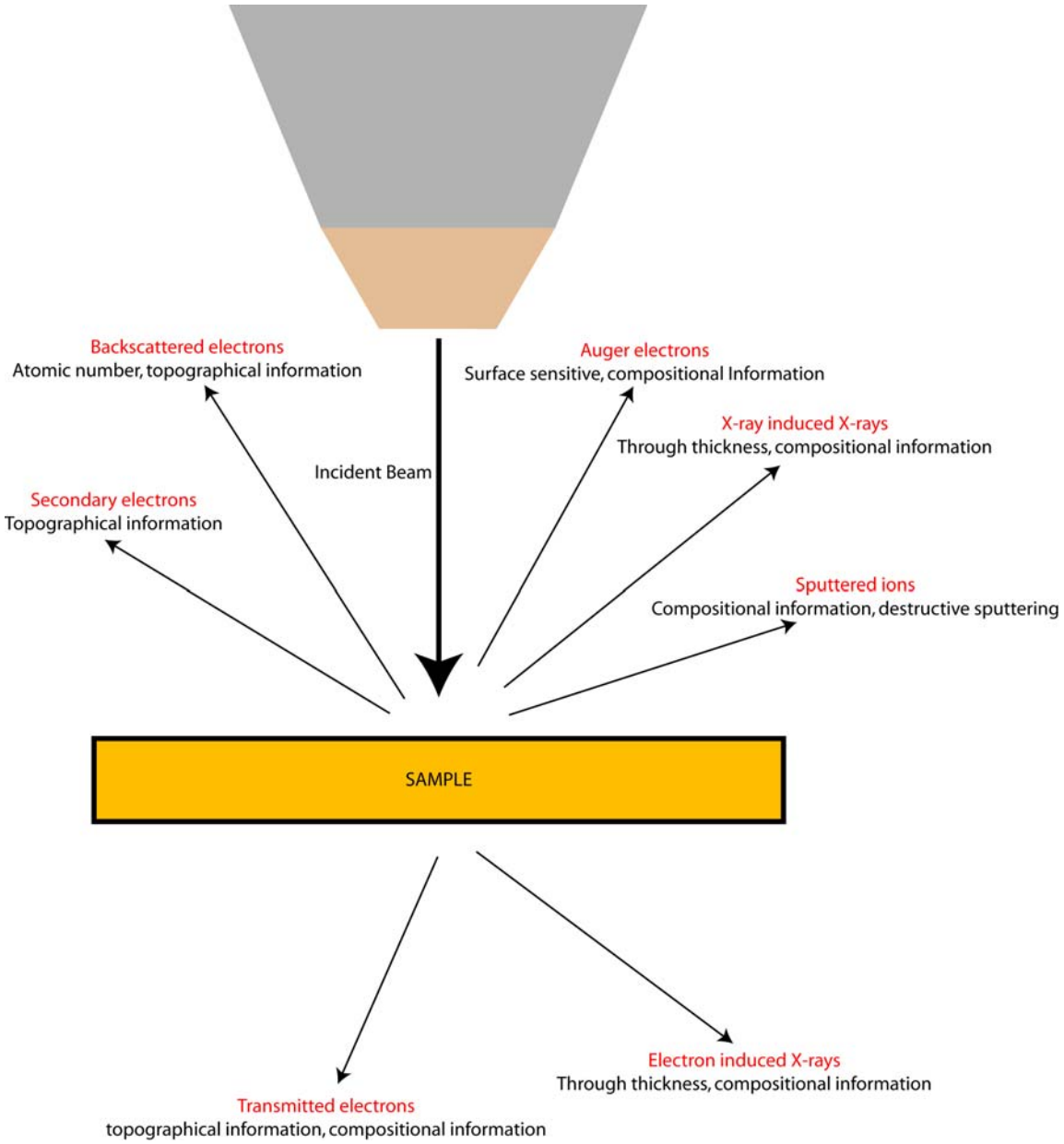

Figure **1-2**: A simplified illustration of the operating physics of some characterization tools. The basic principle is mass or energy in, mass or energy out. FE-SEM generally analyze secondary and backscattered electrons, caused by incident electrons, Auger spectroscopy analyzes auger electrons produced by incident electrons, XRD analyzes X-rays produced by incident X-ray radiation, SIMS analyze sputtered ions produced by incident ions, TEM and EELS analyze incident electrons which were transmitted through the sample, and EDS analyzes X-rays produced by incident electrons.

1.2 Importance and Applications of Thin Films

The modification of the surface properties of a material can be achieved by the application of a thin film on the surface of an existing material. This application of thin films opens up a world of possibility for the creation of materials having specific and controlled surface properties while having different properties for the interior of the material. Properties of films can be grouped into six main categories: optical, electrical, magnetic, chemical, mechanical, and thermal. Each category employs many thin films for common applications. This section will detail many of the applications and uses of thin films in order to highlight their importance in numerous fields.

The optical properties of thin films can be used to alter the behavior of components. Transparent thin films having different refractive indexes can be used in a variety of ways including reflective and antireflective coatings. Multilayers of these transparent films are stacked such that interference patters produced by the transmittance of light is constructive or destructive. Layers stacked such that the interference is destructive are used as antireflective coatings. These coatings are commonly found on the lenses of eye glasses reducing reflection and thus allowing more light to reach the eye [3]. These coatings are also used in similar applications on binocular and telescope lenses, reducing reflection and increasing the contrast. Similarly, layers stacked such that the interference is constructive can be used to create reflective coatings [3]. Selectively reflective coatings, layers stacked so that only a particular range of light passes through them (and the rest reflected) are often used in camera lenses in order to separate the colors of light [3]. Thin film light detectors can be constructed using materials which have an electrical response to exposure to light. These photodetectors are used in a variety of applications, including street lamps which turn on automatically when light is lacking [3].

Much in the same way that micrograined materials can be conductive, insulating, or semiconducting, so too can thin films of equivalent materials. Thin films utilized for their conductive electrical properties can be used as the equivalent of electrical wires in

order to transmit electricity [3]. Thin films utilized for their insulating properties are used as resistors to stifle the flow of current [3]. The accurate control of the dimensions of thin film resistors allows for accurate and reproducible resistance values. Thin films having semiconductive properties can be used in the creation of thin film transistors. The most well known applications of semiconducting thin films in the electrical industry are in the creation of liquid crystals display (LCD) panels [3]. Uses of thin films in this manner hold numerous advantages inherent in miniaturizing components such as reduction in cost and space of equipment. Thin film chemical sensors, such as the carbon monoxide sensors typical in homes operate on the principal that a chemical can change the electrical properties (in particular the conductance) of a thin film resistor, such that the presence of the chemical causes a rise in current passed though the sensor [3].

Chemical properties of thin films are another widespread use for thin film technology. As diffusion barriers, thin films act as a layer which limits the diffusion of particles [3]. Such layers can be found lining the inside of plastic soda bottles, without which, would lose their CO_2 content at a much faster rate. The oxidation resistance of materials such as noble metals can also be used in thin film form. Materials which do not have remarkable oxidation resistance can be coated with a thin film to reduce the oxidation of the surface of the material. In a similar circumstance, corrosion barriers can be coated on materials which would normally be exposed to corrosive environments [3].

Another useful property of materials which can be scaled down for use in thin films is magnetization. As with its thick film counterpart, magnetic thin films are of primary importance in the data storage field [3]. Magnetic thin films are in use today in various forms of magnetic storage such as DVDs and memory discs. Another use of magnetic films with which most people are accustomed to is the thin magnetic film used on items such as key cards and credit cards [3].

Another set of material properties of importance in thin films are properties relating to thermal response. One of the most common applications of thin films engineered specifically for thermal properties is for use as heat sinks [3]. Thin film coatings having high surface area (such as those incorporating spokes) and a high heat capacity serve to transmit the thermal energy from one object into the surrounding

environment. Heat barriers are another application specifically tailored around thermal properties of thin films. By using insulating thin films which can withstand prolonged exposure to high temperature can serve to shield their substrates from the direct temperature. This application has widespread application to turbine blades [3].

Mechanical properties form the last major group of properties which have important applications in thin films. The hardness of a material can be modified by the deposition of a thin film having a different surface hardness (i.e. harder or softer) than the material on which it is deposited. This process is commonplace in tools which are coated with hard materials in order to increase wear and abrasion resistance associated with their use [3]. Another way to alter the mechanical property of a material is by the coating of material having different adhesion or friction properties [3]. Microelectromechanical systems (MEMS) have been developed in recent years, allowing for the creation of mechanical devices typically on the order of several microns. Some of these are sensors as noted previously, but others have novel uses such gears, actuators and switches [4-9]. One such application is the micromachined radio frequency (RF) microelectromechanical switches [10-12] such as those created by the Army Research Laboratories (ARL) in Adelphi MD [13, 14]. These RF electrical switches are similar to the ones in a typical wall socket, but about 100 times smaller. The ARL switch works by allowing the control of two moveable cantilever arms made from lead zirconate titanate (PZT), which when actuated, move a contact pad so that it closes an electrical circuit (Figure **1-3**). In this device, the PZT is stacked between two layers of nanocrystalline platinum acting as co-planar waveguides for the current and a large portion of the device is free from the substrate. Devices such as these are designed to perform their function several times (ideally millions or billions of times) over the course of their lifetime. In order to ensure the reliability of these and similar devices, the mechanical properties of all materials used must be known before they are put into service. The following section will detail the general tensile response of thin films, including methods of testing for these properties.

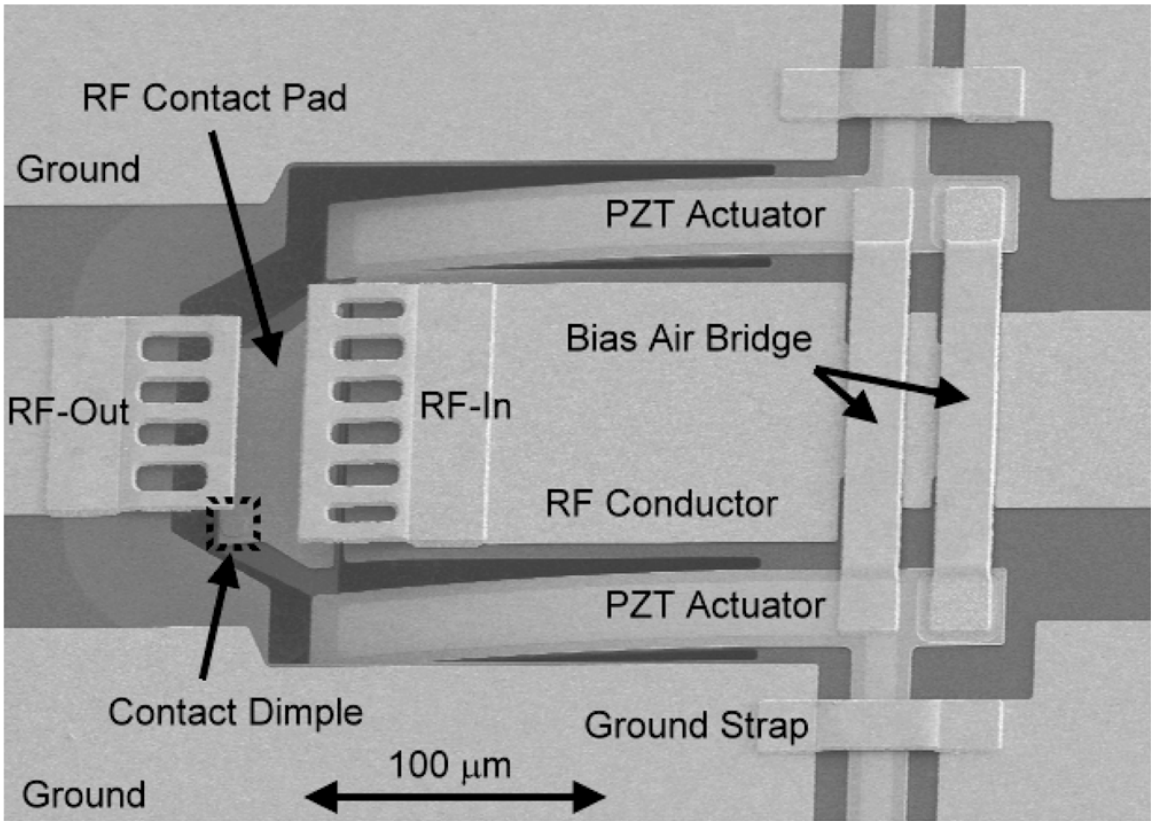

Figure **1-3**: MEMS device used as a microscale switch. This device is composed of stacking of thin films ($Ti/TiO_2/Pt/PZT/Pt$) [13].

1.3 General Tensile Response of Thin Films

Tensile testing is a way of evaluating several aspects of the deformation behavior of a material by applying direct tensile forces to a specimen of known geometry. Tension testing has the advantage of not relying on the application of localized stresses on specimens (as is the case in indentation testing) and results are relatively straight-forward to analyze. This section will discuss tensile testing methodology and typical tensile response of micrograined material systems, and will then transition to the testing methodology of nanocrystalline material systems, highlighting the change in the mechanical response.

In typical tension tests, a specimen of known dimensions is deformed, typically to failure, by the application of an increasing load applied uniaxially to the long axis of the specimen while measuring the resulting specimen behavior. Most often, collected data revolves around the stress and strain response and is typically assembled into a stress-strain curve. ASTM Standard E-8 has detailed standards for the tension testing and of metallic materials including specifications for testing methodology, specimen dimensions (Figure **1-4**) and data interpretation [15]. For the sake of this thesis, terminology will be analogous to that used in the Standard (i.e. definitions for yield stress, ultimate tensile stress, etc).

There are several key features in typical engineering stress-strain curves. Figure **1-5** is an illustration of typical stress-strain curves for (a) a micrograined ceramic and (b) a micrograined metal. Initially, the deformation of materials is elastic, meaning that recovery of strain occurs when the sample is unloaded. In this region, the stress response is linearly proportional to the strain, and the constant of proportionality is known as the elastic (or young's) modulus. The elastic moduli of ceramics are typically higher than those of metals; the elastic modulus of ceramics ranges from 10 to 1000 GPa, while those of metals range from 45 GPa (for magnesium) to 407 GPa (for tungsten) [16]. When the material can no longer accommodate elastic stretching, the linear response ends plastic deformation begins to occur. The point at which irreversible plastic deformation

begins to occur is known as the yield point and it is often estimated using a 0.2% offset from the linear response. Brittle materials, such as most ceramics typically show very little plastic deformation (less than 0.5% plastic strain) prior to failure under room temperature conditions, while ductile materials such as most metals typically undergo larger plastic deformations (greater than 0.5% - brass can accommodate 68% strain for example) prior to failure [16]. The region following the yield point is the plastic region in which plastic (i.e. irreversible) damage accumulates; depending on the material system, there may be some localized necking in the material characterized by a reduction in stress with increasing strain. The material fails when it can no longer accommodate the plastic deformation.

The main difference in the mechanical response under room temperature conditions between ceramics and metals is plastic deformation. There are several plastic deformation mechanisms which can act in micrograined metals and they can be divided into those which operate within the single crystal grains and those which involve transport at grain boundaries. Typically for metals, plastic deformation mechanisms which operate at room temperature are dominated by processes involving dislocation slip (also referred to as dislocation glide). The movement of dislocations through a material is hindered by any obstacle to the lattice such as solute atoms, secondary phases, and grain boundaries. As the size of grains is decreased, grain boundary area in the material increases, reducing dislocation mobility, thereby hindering plasticity and increasing strength. This effect is known as the Hall-Petch relationship and has been shown to follow the relationship in Equation. **1**:

$$\sigma_y = \sigma_0 + \frac{k}{\sqrt{d}} \qquad \mathbf{1}$$

where σ_y is the yield stress of the polycrystalline material, k is the strengthening coefficient of the material, σ_o stress required to move a dislocation in a perfect single crystal region, d is the grain diameter [17]. Under certain conditions, additional plastic deformation mechanisms can also operate. Twinning, the formation of mirroring grain boundaries can occur in metals having BCC and HCP crystal structures when the stress is applied at a high rate and at low temperatures, when deformation by plastic slip is limited

[16]. Additionally, some materials can undergo phase transformation due to applied stresses and strains. At higher temperatures more plastic deformation mechanisms can operate. Creep, time dependent plastic deformation, as well as reorientation, and growth of grains can occur through diffusional processes for which there is generally insufficient energy at room temperature [17]. The result of these deformation mechanisms is that micrograined metals tend to show large strains prior to tensile failure, typically between 20 and 40 percent elongation. The same cannot be said about typical ceramic materials at deformed at room temperatures. Due to their ionic bonding, ceramics tend to have more complicated crystal structures having larger interatomic plane spacing. As a result of this structural difference, plastic deformation mechanisms which act in metals are less likely to occur in ceramics [18]. The result is a more brittle material, showing very little plastic strain prior to failure.

Characteristic behavior of micrograined metals would suggest that as grain structure is refined, metals should have higher yield stresses and higher ultimate tensile stresses. The creation of thin films possessing grain sizes less than 100nm in size achievable by tailoring the deposition parameters of the films, wherein micrograined structures there is a need for post-fabrication modification such as cold working [19]. Unfortunately, attaining a stress-strain curve in thin films is much harder to accomplish than with their micrograined counterparts. In order to accurately test the mechanical behavior of thin films, tests must take care to ensure that no substrate effects are seen. Although there are some testing methods which do allow the mechanical characterization of thin films while they are still connected to the substrate, such as nanoindentation [20], tensile testing of thin films necessitates the creation of free-standing thin films. The creation of free standing thin films which are nominally flat and have a uniform thickness is a challenge on its own.

The modification of conventional tensile testing techniques developed for micrograined specimen testing requires new gripping, loading and measurement techniques. There are physical difficulties associated with properly gripping specimens of small dimensions and with delicate features and in applying uniform loads across specimens which tend to bend and twist out of plane. Complexities also arise from

measuring the stress and strain in the samples with sufficient resolution – forces required to create appropriate stresses are very small (on the order of microNewtons), and requires resorting to novel gripping techniques such as on-chip tensile testing, mechanical clamping, electrostatic gripping, and micro-gluing gripping systems [21, 22]. While relatively simple modifications can be made to gripping and loading, strain measurement requires adaptation of novel techniques because the application of traditional strain gauges is no longer feasible. Several techniques, including x-ray diffraction (XRD), speckle interferometry and digital image correlation (DIC) have been shown to work [22, 23]. X-ray diffraction as detailed previously has the capacity to measure fine changes in lattice spacing but requires testing to be done within the confines of the apparatus and due to the amount of time it takes to establish high quality scans (at several angles and long counts) it precludes the testing of any material which may exhibit creep. Speckle interferometry uses light to generate an image of the displacement fields of features on the surface of a film. This method is dependant on the wavelength of light and surface roughness or surface features of the film, and is further complicated by the fact that rigid body motion can create considerable changes in the displacement fields. DIC is a method in which consecutive images of the surface of strained film are compared to one another or an original image for the analysis of strain. This method is also dependant on surface features of the film and the resolution of the camera recording the images.

Due to the difficulties inherent in mechanical testing of nanocrystalline materials, use of theoretical computations and simulation studies have become prevalent. Although these investigations provide good working models and theories, they must be supplemented by actual experimental investigations in order to be validated. Several investigations utilizing these methods have made predictions regarding the behavior of such materials [24-27]. The consensus within these works is that there will be a measurable increase in hardness, yield strength, and ultimate tensile strength as the grain size is refined down to approximately 50 nm, in close agreement with the Hall-Petch effect described previously. Below 50 nm, most models suggest that there will be a shift in the plastic deformation mechanisms, changing from a grain-interior process dominated

by dislocation slip, to a more grain boundary process dominated by diffusion; this is consistent with reports of inverse Hall-Petch relationship at those grain sizes [28].

Despite the difficulties of experimental testing on such a small scale, there is some data on the mechanical behavior of ultra-fine grained and nanocrystalline metals. Taking FCC metals such as nickel, copper and aluminum for example, an increase in hardness, yield strength, and ultimate tensile strength along with a corresponding decrease in elongation to failure is typically observed [5, 29-36]. Although this data is valid, noted room temperature creep effects, as well as strain rate sensitivity and environmental effects make the analysis of mechanisms fairly complex, and have resulted in conflicting conclusions. One way to simplify mechanistic analysis would be to test a set of metals which do not exhibit one or more of these disadvantages, for example, testing metals which are not prone to be environmental influence; in addition, such metals are also more likely to be used in devices if their other mechanical properties prove sufficient. Noble metals are the set of metals which are most resistant to corrosion and oxidation, most typically noted as silver, gold, platinum, palladium, rhodium and tantalum. These noble metals have a face-centered cubic (FCC) crystal structure (with the exception of tantalum which is body-centered cubic) and are relatively rare (platinum for example is only found in 5 ppb in the earths crust), which tends to make them relatively expensive. When pure, polycrystalline, and annealed, these metals have an elastic modulus of about 100 GPa (Silver is the lowest at 74 GPa and rhodium is the exception at 360 GPa) and yield points typically less than 10% of the ultimate tensile strength (typically <100 MPa) [37]. Although their mechanical properties and high costs limit their viability in pure micrograined form, thin layers of these pure metals can be produced inexpensively and would have significantly improved mechanical properties.

There are very few investigations of the properties of nanocrystalline noble metal films, and the majority of those investigations are limited to nanoindentation tests [38-40]. These investigations must assume a Poisson's ratio for the material they test and produced data is typically limited to elastic modulus and hardness. There are a few reports of tension tests conducted on nanocrystalline noble metals which are both more reliable, and easier to compare with the tension test reported on in this work. Sharpe et al,

tension tested 3 gold films of varying thicknesses (1000, 500 and 150 nm). They found that elastic modulus decreased with thickness, reporting an elastic modulus of 73, 65 and 51 GPa respectively. Yield strength did not correlate with grain size, and varied between 328 and 371 MPa, about one and a half times the yield strength of microcrystalline gold of 205 MPa [23]. Chasiotis et al measured the strain sensitivity of gold films of varying thickness (2800, 650 and 500 nm). They found the gold films to be strongly rate sensitive, with each film having its highest value of yield strength (220, 295 and 240 respectively) at the fastest strain rate. They found a similar dependence on the ultimate tensile strength (260, 265 and 305 respectively) and an inverse relationship for strain to failure [41]. Wang et al conducted similar strain rate sensitivity tests on their gold samples. They noted their samples, which were 1000, 500 and 250 nm thick had grain sizes of 100, 50 and 40 nm respectively. Although they did not find an elastic modulus dependence on thickness or grain size, they did find similar strain rate results, noting that the highest yield strengths achieved (277, 355 and 390 MPa respectively) and lowest strain to failure were achieved at the highest strain rates [42]. Samuel et al conducted room temperature relaxation tests on gold thin films inside an SEM chamber. They concluded there was a significant size effect on the relaxation scale, noting the relaxation time constant of nanocrystalline gold was 180-200 seconds, orders of magnitude higher than microcrystalline gold [43]. Sanders et al conducted tensile experiments on nanocrystalline palladium thin film sheets. They reported that their films' grain sizes of 54, 38 and 16 nm showed a correlation in elastic modulus, reporting 193, 123 and 117 GPa respectively, all lower than the elastic modulus of microcrystalline palladium (132 GPa) [32]. These tests help establish some general characteristic on nanocrystalline noble metals: they follow the Hall-Petch relationship for the grain sizes tested, they typically show a lower elastic modulus than microcrystalline samples, and they typically show an increased strain rate sensitivity and room temperature relaxation when compared to microcrystalline samples. These conclusions, in particular the latter three, reinforce the idea that there may be a shift in the mechanism governing plastic deformation of nanocrystalline metals.

It is clear that not enough research has been done in this area to fully characterize noble metals' mechanical response especially taking into consideration the lack of testing of silver, rhodium and tantalum specimens. In addition to this, the mechanical properties of materials are not limited to their response to a single applied load. Equally important (if not more) is a material's response to cyclic loads. A material's response to cyclic loading is known as its fatigue behavior, and can be used to predict the lifetime of the material. The following section will detail the testing methodologies and fatigue response of micrograined and nanocrystalline materials.

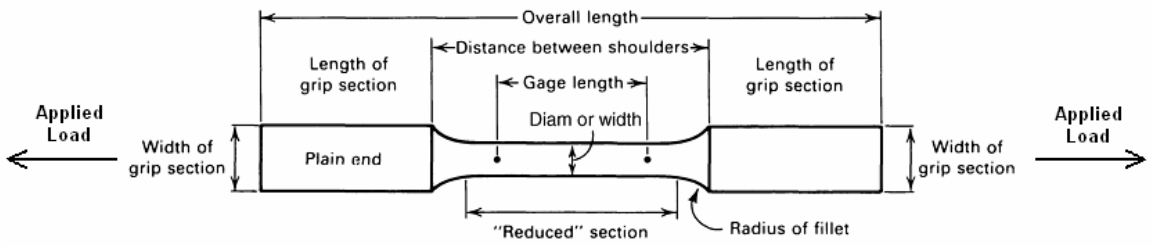

Figure **1-4**: Schematic of tension testing specimen nomenclature modified to show to direction of applied force [15].

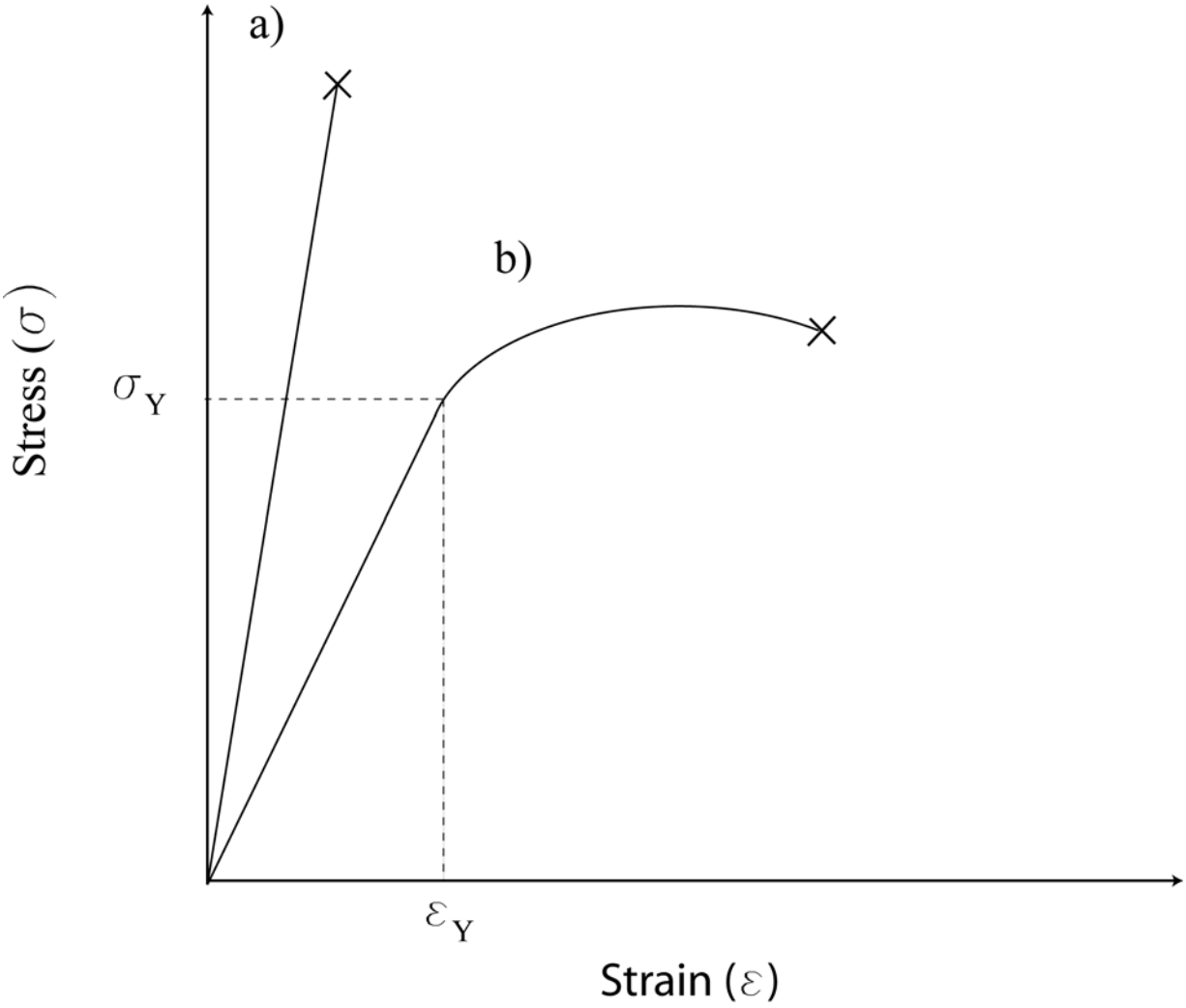

Figure **1-5**: Typical engineering stress-strain curve of (a) a ceramic material showing no plastic deformation and (b) a micrograined metal showing some plastic deformation prior to failure. The yield stress and strain of the metal, the point at which plastic mechanisms dominate the mechanical response, are marked.

1.4 General Fatigue Response of Thin Films

In many common applications, materials are loaded and unloaded numerous times over the course of their use. Fatigue testing is a mechanical testing technique which provides important information about the reliability of a material under such cyclic loads. The complications inherent in tensile testing of thin films are also present in fatigue testing, in addition to several other complications specific to fatigue testing. This section will discuss fatigue testing methodologies and typical fatigue response of micrograined metallic material systems.

Fatigue is the process whereby stresses or strains are repeatedly applied to a material and cause cracking and/or failure (Figure **1-6**). Much in the same way that tension testing techniques had to modified to accommodate thin films samples (i.e. gripping, strain tracking etc), conventional fatigue tests of thin films must be similarly modified but the specimen must now withstand the repetitive loading and unloading inherent to fatigue. New issues arise regarding the control of the experiment; aside from the necessity of controlling the more complex cyclic waveform (sinusoidal, square, etc), further difficulties are caused by the specimen's reaction to fatigue. Mechanical responses such as strain hardening, strain softening, as well changes in compliance due to crack propagation, make controlling the experiment even more difficult.

Mechanisms for fatigue crack growth and failure have generally been subdivided into two main categories: fatigue of intrinsically toughened materials and fatigue of extrinsically toughened materials (Figure **1-7)**. The first category is usually related to ductile metals, and the second to brittle ceramics. While fatigue of structural materials can often be attributed to combinations of these classes of mechanisms, the unique features of these general groups allow broad interpretation and mechanistic views to be developed.

The first category of fatigue behavior occurs mainly in micrograined ductile metals in which grain size is typically on the order of micrometers to millimeters. Three modes of crack advance exist in this fatigue behavior – threshold growth, stable crack growth, and fast fracture. These regions are termed regime I, regime II, and regime III

respectively [44]. Regime I is known as the threshold regime where cracking is initiated. This regime shows a large influence of microstructure, mean stress, and environmental conditions. Regime II, also known as the power law or Paris regime follows the relationship shown in Equation. **2**:

$$\frac{da}{dN} = C(\Delta \mathrm{K})^m \qquad \mathbf{2}$$

where $\frac{da}{dN}$ is the fatigue crack growth rate, ΔK is the stress intensity range, m is the power law exponent and C is a scaling constant. This crack growth region is dominated by cyclic dislocation motion along glide systems at the crack tip. The stress intensity factor range is typically 1 to 100 MPa √m and typical power law exponent values m are 2 to 4 and has a strong dependence on the ratio of minimum to maximum applied load, load ratio (typically noted as R), microstructure, and environment [45]. This failure mode may leave behind distinct fatigue striations which can be seen on the fracture path [45]. The third regime is accelerating crack growth and where gross plastic deformation of the specimen occurs. The second category of fatigue behavior occurs mainly in micrograined brittle ceramics. For these materials, plastic deformation is associated with a breakdown of crack-tip shielding mechanisms (e.g., crack closure, microcracking, and phase transformations [18]). Unlike in ductile metals, brittle ceramics exhibit a more limited range of subcritical crack growth, typically 1 to 10 MPa √m, and the associated power law exponent is higher, typically 10 to 50 [45].

More recently, length scale dependent fatigue mechanisms have been closely investigated. This third type of fatigue deals primarily with scenarios exclusive to nanocrystalline or thin film metals in which grains are no longer large enough to contain dislocations or surface layer mediated crack initiation and growth is complicated by the increased surface-to-interior ratio in thin films. The fatigue of micrograined materials has been investigated for over a century, but the fatigue properties of nanocrystalline solids and of thin films has only been studied for four decades and so there is far less available data on their mechanical properties and even less data of the fatigue properties of these materials. Very limited experimental work on fatigue of pure nanocrystalline metals can

be found. The earliest of these works is by Witney et al who conducted tension-tension fatigue on nanocrystalline copper which was prepared by inert gas condensation [46]. Witney induced several hundreds of thousands of cycles with stress ranging from 10 MPa to 80% of the yield stress. Witney noted that the cyclic deformation appeared to be elastic, despite elongation and an approximately 30% growth in grain size during the test. A study conducted by Vinogradov et al on ultrafine grained titanium which was prepared by equal channel angular pressing (ECAP) [47]. Vinogradov noted a considerable increase in both the fatigue life and the fatigue limit when testing under constant load testing when compared with microcrystalline titanium. Vinogradov concluded that the Hall-Petch strengthening played an important role in the resulting properties. Hanlon et al investigated the fatigue properties of electrodeposited ultrafinecrystalline and nanocrystalline nickel as well as ultrafinecrystalline titanium produced by ECAP. Figure **1-8** shows one of the plots from the investigation, illustrating the differences in crack growth rates between ultrafinecrystalline and nanocrystalline nickel. The study noted three major observations from the fatigue of these materials: grain refinement to a nanocrystalline microstructure leads to an increase in total life under stress controlled fatigue, increasing load ratio had a 'deleterious' effect on fatigue crack growth, and that grain refinement generally led to 'smoothening' of fracture surface path and features [48, 49]. This study also noted that crack closure, an interaction of the two crack wake fronts serving to reduce stress at the crack tip may have played a role in the fatigue process, and that these effects may have been caused by environmental factors such as oxidation. A good review of these results and several others on different materials systems such as steels and metallic alloys was written by Meyers et al [27]. All of the experimental works show good agreement, even across different material systems. They all conclude that as grain size is decreased, fatigue life is enhanced, and all of the studies imply that constitutive relationships can be predicted from the microcrystalline metals.

Of late, several mathematical models [50], molecular dynamic simulations [51-53], and finite element models [54] have been developed to predict and explain the deformation mechanisms of nanocrystalline metals. Several review papers summarize the modeling work done [24-27] and all concluded that these models, albeit dealing with

ideal conditions, are reliable, but need to be complemented with experimental work. Most of these models dealt with tensile loading, leading to a major lacking point in a quantitative prediction of the fatigue response of metals. One set of investigations by D. Farkas of the fatigue in nanocrystalline metals based on the first principles of nickel predicts crack growth dominated by nano and microvoid formation ahead of the crack tip [48, 49]. Despite the prediction of intergranular failure, the two molecular dynamic simulation data points achieved using simulations of much smaller grains with different orientation led Farkas to claim that the results were aligned with experimental data, citing the nanocrystalline nickel study done by Hanlon. None of these investigations predict the type of a change in mechanism that this study will show occurs in nanocrystalline platinum – an initially grain boundary dominated deformation mechanism, which transitions to a grain interior dominated deformation mechanism. Given the pros and cons of modeling, models can be used a basis for the prediction of behavior, but must be validated by experimental work.

In order to be able to create reliable 'next generation' MEMS, the fatigue properties of the materials which make them up must be evaluated. There is increasing evidence to support the theory that plastic deformation mechanisms in nanocrystalline metals differ from their micrograined counterparts despite experimental work which points to the contrary – that mechanical behavior of nanocrystalline metals can be predicted from their microcrystalline counterparts. Only experimental testing of free standing nanocrystalline metallic films can help shed light on the deformation mechanism. The following section will discuss platinum as a new model material which can be experimentally tested to establish such fatigue behavior and deformation mechanism.

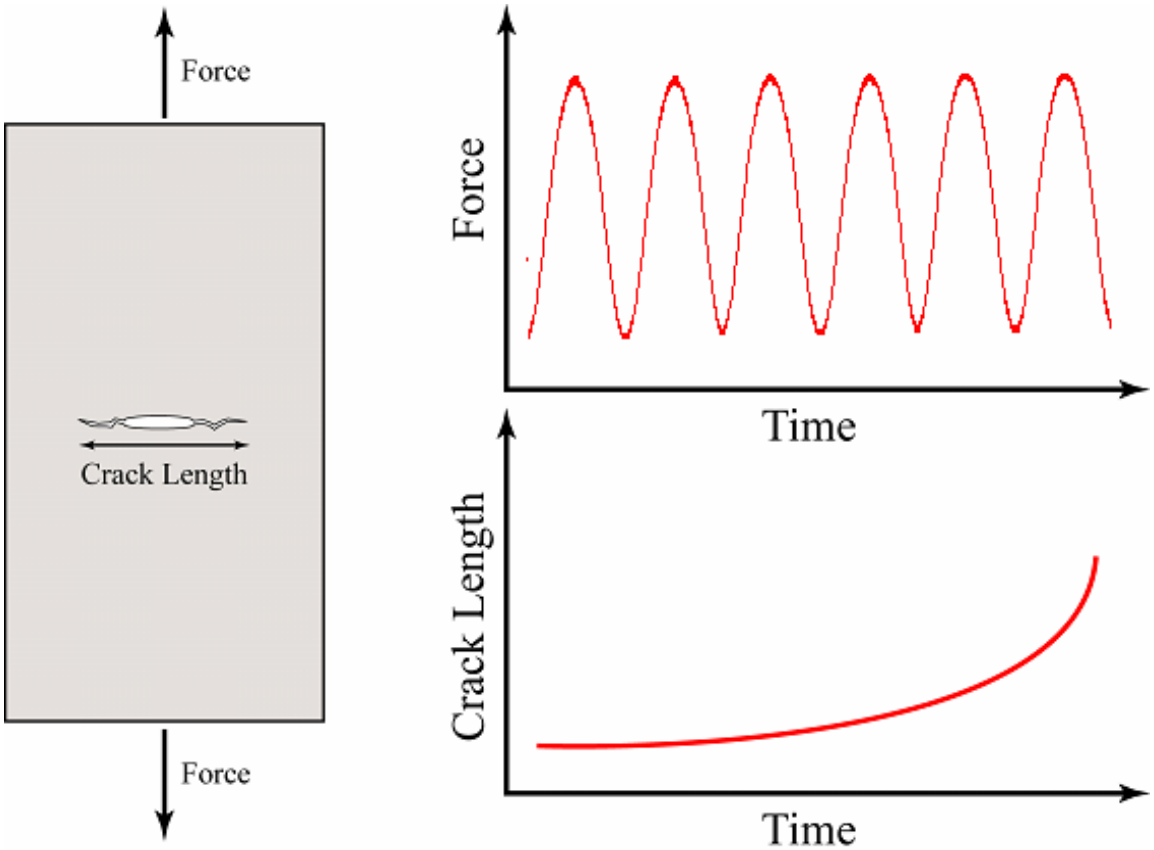

Figure **1-6**: schematic showing a sinusoidal waveform of applied force applied to a thin film causing fatigue crack growth (crack extension)

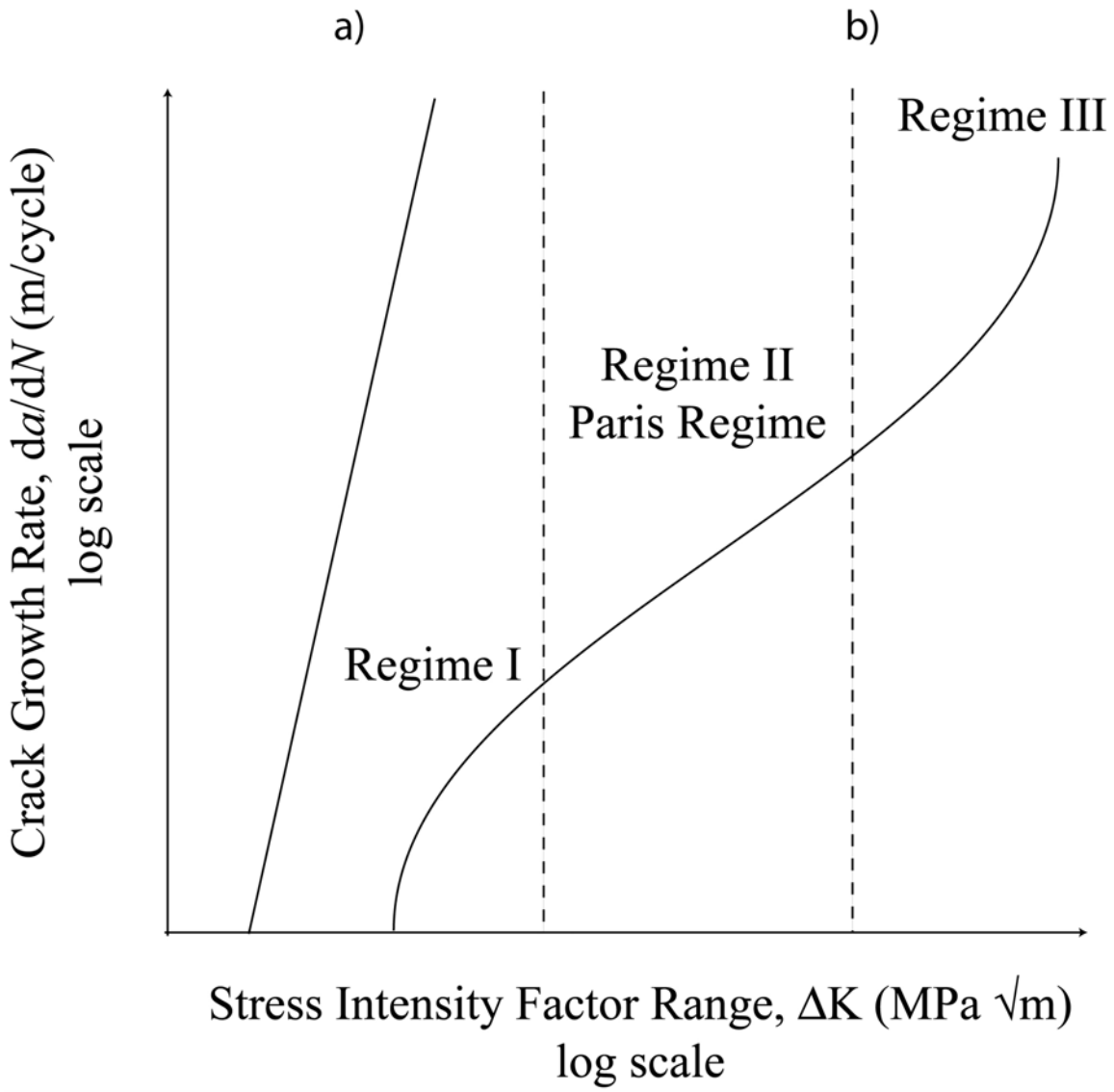

Figure **1-7**: Fatigue crack growth rate curves for (a) brittle materials such as ceramics and ordered intermetallics and (b) ductile materials such as metals

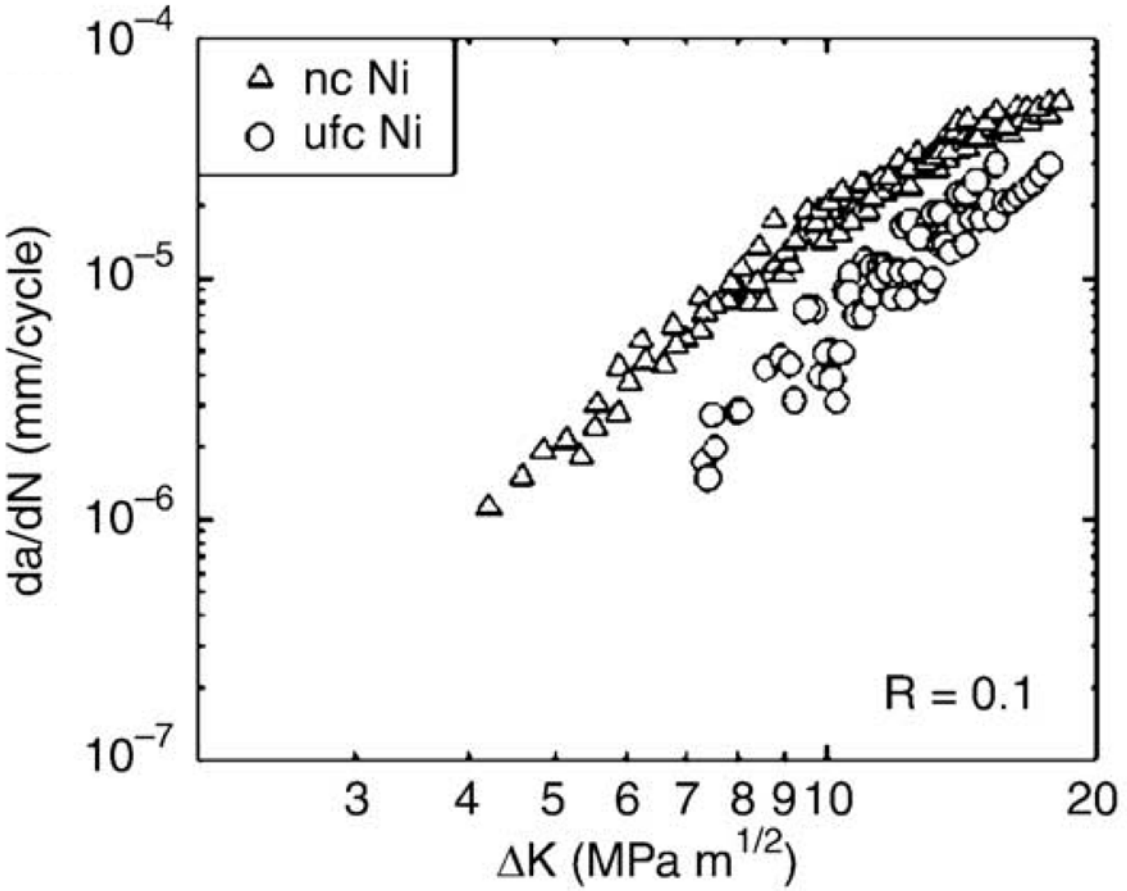

Figure **1-8**: Crack growth rate as a function of the stress intensity factor in ultrafinecrystalline (ufc) and nanocrystalline (nc) nickel under a load ratio of 0.1 [49]. Although these results show a decrease in K_{th} and an increase in crack growth rate for a given stress intensity when compared to microcrystalline nickel, the constitutive relationships are still the same, with a slope m, of about 2.

1.5 Platinum: A New Model System

In order to establish the fatigue response of nanocrystalline metallic thin films, a model material system should be selected. With the majority of previous work focusing on nickel [48, 49], it may be wise to select an alternate metallic system, but in order for the new studies to complement the previous experimental and modeling work, this new model system must be sufficiently similar. Thus, the new model should be a nanocrystalline, face centered cubic metal, preferably with grain sizes larger than 10 nm (analogous to the modeling work) but smaller than 100 nm (analagous to the nickel work). In order to match the modeling work further, the nanometer sized grains would ideally be columnar [51-53]. In order to reduce environmental effects, such as those of oxide induced crack closure, specifically mentioned to play a role in the fatigue of nickel, selecting a system which is naturtally resistant to oxidation would be greatly beneficial. From these few criterions, nanocrystalline platinum was selected. In addition to the aforementioned characteristics, platinum is also a refractory metal, having a melting point of 2041 K [16], and it is already in use in several thin film devices such as those mentioned in **Section 1.2**. It is an ideal metallic system with which to establish the fatigue behavior of nanocrystalline metals.

The fatigue of microcrystalline platinum provides a good example of typical fatigue behavior of a microcrystalline metal and will later provide a good comparison to fatigue testing of nanocrystalline platinum reported in this thesis. One paper [55] denotes four fatigue experiments carried out on micrograined platinum (presumed from the processing conditions) samples with typical dimensions 10mm × 60mm × 100 mm - it is worthwhile mentioning that each such sample would cost about $70,000 in today's market, while a sample of rhodium of similar size would cost almost 6 times as much, perhaps explaining why not many such tests are conducted on large samples composed of noble metals. Of the four fatigue tests, two were conducted in air, one in a 5M NaCl solution, and one in vacuum (Figure **1-9**). In all cases the power law exponent was estimated to be 3.5. The data shown in the report was closure corrected, making regime I of the fatigue curve difficult to see. The fatigue test in vacuum, which has a load ratio, *R*

= 0, did show some evidence of a threshold despite this closure correction. It was noted in the report that only in vacuum was ‘fine crack branching’ observed whereas in the other tests the crack was ‘single and straight’; which goes to show that there may be an environmental effect on materials, even in the case of noble metals. These fatigue tests largely show that microcrystalline platinum behaves as a typical microcrystalline metal. The fatigue properties of the nanocrystalline platinum investigated in this study show that nanocrystalline platinum behaves in some ways more like a brittle ceramic than a ductile metal and illustrates that the plastic deformation mechanism operating during fatigue cycling is measurably different than that of micrograined platinum.

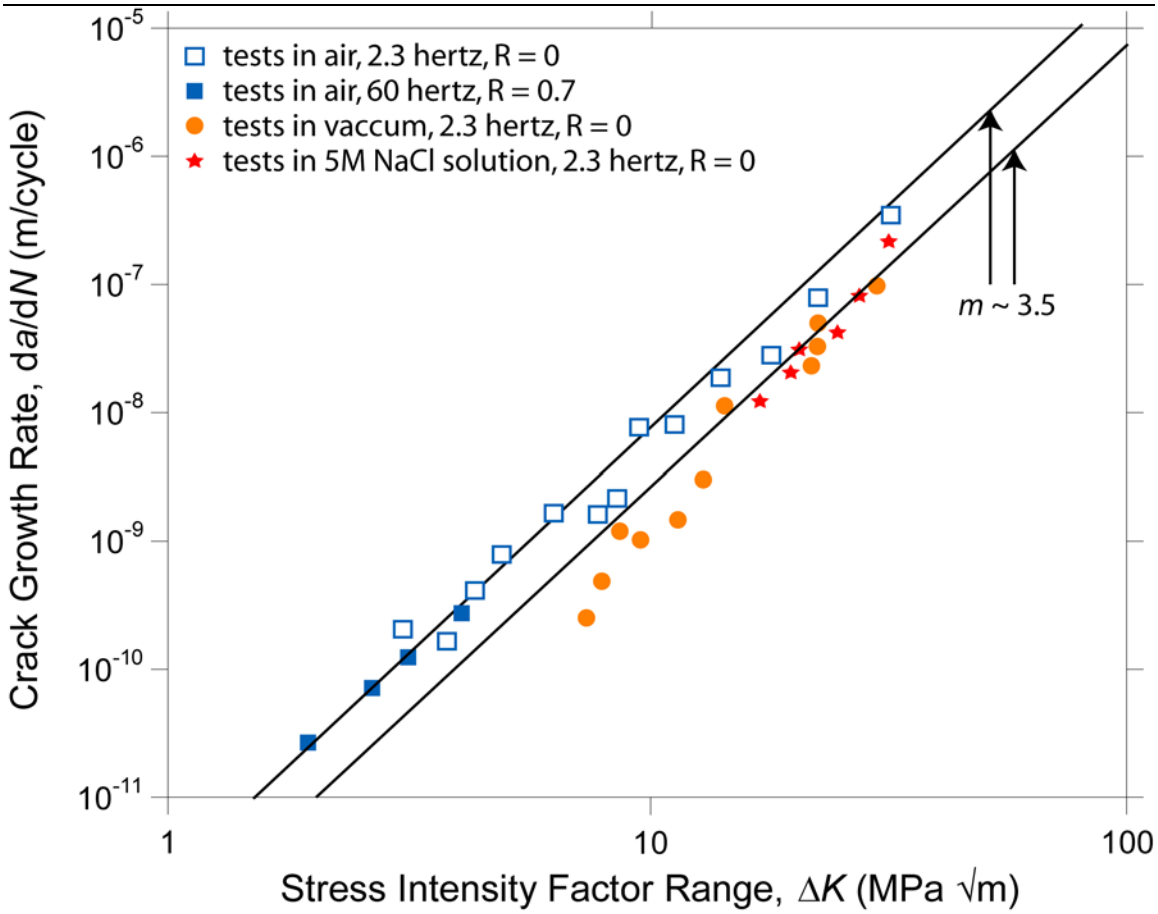

Figure **1-10**: Fatigue tests conducted on microcrystalline platinum samples showing typical fatigue behavior for a microcrystalline metal [55].

1.6 Structure of Thesis

Chapter 2 will discuss the materials and methods used in this study. The section will open with a deposition techniques used in fabricating the test specimens. Characterization techniques, including optical microscopy for inspecting specimen fabrication, atomic force microscopy (AFM) to determine surface roughness, X-ray diffraction (XRD) to determine texture, transmission electron microscopy (TEM) to determine orientation, energy dispersive spectroscopy (EDS), electron energy loss spectroscopy (EELS) and secondary ion mass spectrometry (SIMS) to quantify the relative purity of the films. Further details about the physical specimens such as geometry, surface roughness, and physical dimensions, all of which affect the results of testing will be discussed. The mechanical characterization system will be fully outlined; all the various parts necessary to conduct a test will be detailed. The methodologies involved in the reported tension test and four fatigue tests will be listed. The analysis methods used to analyze each test will be discussed. Finally, post-testing characterization of the samples will be discussed, including preparation of samples for field emission scanning electron microscopy (FE-SEM).

Chapter 3 will feature the results and discussion. The result of a tensile test performed on a notched specimen will be discussed. Results from fatigue testing, including crack length vs. cycle and crack growth rate vs. stress intensity will be highlighted. A discussion of the compliance-based inspection for crack closure will follow, highlighting the apparent lack of crack closure. Results of FE-SEM analysis of the fatigue fracture surfaces highlighting a velocity-dependant crack mechanism will be discussed in order to give a partial explanation for the testing results. A comparison will be made between the results found in this work with observations documented in the literature and mechanisms for the new findings will be proposed in order to explain behavior which cannot be fully characterized by conventional explanations. The last section of the chapter will be an analysis of the crystallography of slip within a textured FCC metal such as platinum providing an alternate hypothesis for the observed fracture path.

Chapter 4 will wrap up the thesis by listing the conclusions of the study. Using evidence gathered by a variety of characterization tools, as well tensile testing of the films, a conclusion will be drawn regarding the purity and integrity of the platinum thin films. Following results of fatigue testing of the film, conclusions will be drawn regarding the fatigue behavior of platinum, including crack growth rate curves which are more reminiscent of ceramic materials, a reduction in fracture toughness, and velocity-dependence of fatigue crack growth mechanism. A conclusion will also be presented about the lack of crack closure seen for platinum. Conclusions will be drawn regarding the fracture surfaces produced by these fatigue tests, highlighting a transition in the fracture path from an intergranular mode to a transgranular mode. The last portion of the thesis will list several recommendations by the author as per future tests which can be conducted using the current technology and testing system in order to further test the proposed mechanisms, as well as explore other parameters relevant to mechanical behavior.

Chapter 2

Materials and Methods

This chapter will discuss the materials and methods used in this study. In order to understand the material which is being tested, the chapter will open with a brief discussion of deposition environment and technique which was used in its fabrication. The physical properties of the specimen finished specimens as evaluated by a variety of techniques will follow. The surface roughness, as evaluated optically and by atomic force microscopy (AFM) and its relevance to tension testing will be discussed. Results of this analysis will show that specimens have a very smooth surface free of optically visible features, ideal conditions for tracking crack growth through a specimen but complicating the processes of measuring strain. A discussion of texture analysis by X-ray diffraction (XRD) will follow. This analysis will show that the platinum films are composed of primarily (111) oriented platinum grains. Analysis of thinned down sections of the film by transmission electron microscopy (TEM) will confirm results found by XRD, and will also show that the interior of the film is composed of columnar grains 25-40 nm in diameter. This technique will also confirm that no gross voiding or cracking can be detected within the film. Further analysis of these films by energy dispersive spectroscopy (EDS), electron energy loss spectroscopy (EELS) and secondary ion mass spectroscopy (SIMS) will show that the film is free from contamination up to the detectability limits of the instruments. Further details about the physical specimens such as geometry and physical dimensions, as measured by several techniques will be also discussed.

The mechanical characterization system and testing procedure will be detailed, beginning with a sample still connected to the substrate and describing its path to and through testing. A table will list all the parameters relevant to individual tests, as many changes were made as the testing technique was expanded and improved. The methodologies involved in the reported tension test and four fatigue tests will be listed.

The analysis methods used to analyze each test will be discussed, as the results from these analyses will be discussed in a later section. Finally, post-testing characterization of the samples will be discussed, including preparation of samples for field emission scanning electron microscopy (FE-SEM).

2.1 Samples

The fatigue degradation behavior of a noble, nanograined metal was explored using pure Pt films. The free-standing, 430 nm thick, Pt films on top of a 20 nm Ti adhesion layer were produced in the Army Research Laboratories. This section will detail the fabrication techniques employed by Ronald Polcawich for the creation of the free-standing specimens used in this study. Following fabrication details, the resulting specimens' surface roughness, texture, crystallography, and geometry will be discussed.

2.1.1 Deposition

The samples tested in this study were fabricated by Ron Polcawhich at the Army Research Laboratory's Specialty Electronic Materials and Sensors Cleanroom Facility in Adelphi, MD. Fabrication began with a 100mm diameter single crystal silicon wafer (100) substrate with a resistivity of 1 – 30 Ohm-cm. All films were sputtered onto the substrate using a Unaxis Clusterline 200 deposition system configured with individual chambers for Ti and Pt deposition. The first layer deposited onto the silicon substrate was a 20nm thick titanium layer. This layer served as an adhesive layer for the platinum layer to follow. The second layer deposited at the conclusion of the titanium sputtering was the 430nm platinum layer. The deposition parameters are listed in Table **2-1**. All depositions occurred at 50ºC in order to prevent the formation of platinum silicides.

In order to pattern the platinum films into the specimen design, a thin film resist (Clariant AZ5200) was first spun onto the entirety of the wafer surface and exposed using contact lithography with a Karl-Suss MA/BA-6 aligner. After exposure and resulting resist development, the wafer underwent a two minute oxygen descum process in a Metroline ML4 asher to remove any residual organics. Following, the resist was cured at 220ºC along with a dose of ultra-violent radiation in an Axcellis Photostabilizer. The UV cure process improves the photoresist resistance to ion-bombardment damage during the argon ion-milling procedure. After the resist has been cured, the undesired regions of platinum were removed with argon ion-milling using a Commonwealth ion-mill system (see Table **2-2** for milling parameters). After milling, the resist was removed by exposure to oxygen plasma for 25 minutes (see Table **2-3** for plasma parameters).

Each tensile specimen die had 6 individual specimens. A Disco Dicing Saw was used to separate each die on the wafer. With the wafer coated in photoresist, die separation was done using a Disco Dicing Saw with a 150 μm wide blade using a 3 mm/s feed rate. Following the wafer sawing process, individual die were cleaned using a series of solutions: acetone, methanol, isopropyl alcohol, and deionized water. Clean die were dried using blowing nitrogen.

Next, the dry die were placed into a Xactix Xetch system to facilitate the release of the tensile specimens by removing the silicon from underneath of the specimens. In this process, 2 Torr of XeF_2 was combined with 20 T of N_2 and subsequently transferred to the wafer chamber for a 20 second etch. This process was repeated until the specimens were released from the substrate and supported by the tethers in the specimen gripping region. The packed die were then placed into individual Gel-pak^{TM} carriers and delivered by courier to Pennsylvania State University for testing.

Table **2-1**: Deposition conditions for all sputtered metals

Material	**Ar (sccm)**	**O_2 (sccm)**	**Pressure (mTorr)**	**Temp (ºC)**	**Power (W)**
Ti	30	0	5	50	1000
Pt	50	0	5	50	500

Table **2-2**: Parameters used for ion-milling Pt thin films

Item	**Voltage (V)**	**Current (mA)**
Cathode	11.5	14
Discharge	40	2.5
Beam	500	300
Accelerator	100	34
Neutralizer		500
Bias	36	
Ar (sccm)	10	10
Operating Pressure (Torr)	7×10^{-4}	7×10^{-4}
Chuck rotation (rpm)	5	5

Table **2-3**: Parameters for oxygen plasma processes

Description	**O_2 (sccm)**	**Pressure (mTorr)**	**Temp (ºC)**	**Power (W)**
Descum	200	525	~70	200
Resist removal (ash)	500	1000	~160	400

2.1.2 Texture and Crystallography

Each specimen arriving to Penn State was individually examined under an optical microscope and inspected for flaws such as surface cracks, bend contours, plastic deformation such as dents or crinkles, malformed or broken samples, improperly released samples, and surface debris. This optical characterization however, represents only a small fraction of the characterization of these specimens. The following section will describe the texture and crystallography characterization of the specimens by using Atomic Force Microscopy (AFM) to analyze surface roughness, X-ray diffraction (XRD) to determine texture, transmission electron microscopy (TEM) to determine orientation, and energy dispersive spectroscopy (EDS), electron energy loss spectroscopy (EELS) and secondary ion mass spectrometry (SIMS) to quantify the relative purity of the films.

2.1.2.1 Atomic Force Microscopy Analysis of Surface Roughness

The surface of the samples is of critical importance as the first indicator of flaws in a specimen. For tensile testing, this roughness is also a measure of visible features on the surface that can be used to track strain in the sample. This section will provide some details and results of the optical and atomic force microscopy analysis of the surface of the platinum samples.

Samples which were properly formed and released as a result of good fabrication runs most commonly exhibited a clean and visibly flat surface devoid of flaws such as surface cracks, bend contours, and plastic deformation such as dents or crinkles. An atomic force microscopy study was conducted on the nanocrystalline platinum samples to gauge their roughness. The study was conducted using a Dimension 3100 atomic force microscope produced by Veeco, and using tips produced by Nanosensors. Further instrument parameters which were used to obtain the results are listed in Table **2-4**. One studied sample exhibited a root mean square (RMS) value of 2.615 nm over a 1 μm^2 area

(Figure **2-1**). As all samples came from the same chip and were deposited at the same time, the surface of all platinum samples is assumed to be nominally flat to about the same value. The features seen on the top layer of the platinum sample were measured using point to point comparison using Photoshop® CS2, a graphics editor from Adobe Systems, and found to be approximately 10nm in size. Analysis of the interior of the film detailed in a future section will show that the average size of a grain on the interior of the film is closer to 35nm, and thus, the features on the surface of the film are not indicative of the grain size in the interior.

Although having such a surface is a great benefit to tracking crack growth via surface viewing, it makes strain measurement via digital image correlation (DIC) very difficult. DIC is a technique which is capable of measuring changes in the distances between features in an image – not having any features is an obvious disadvantage in using this method. Although this problem was worked out in future specimens by adding surface features through a spray-staining technique, no strain measurements could be made during tension tests of these samples.

Table **2-4**: Atomic Force Microscopy Running Parameters

Mode	Scan Size	Aspect Ratio	Scan Rate	Samples/ Line	Integral Gain	Proportional Gain
Tapping	1μm	1:1	1 Hz	512	.4	1.0

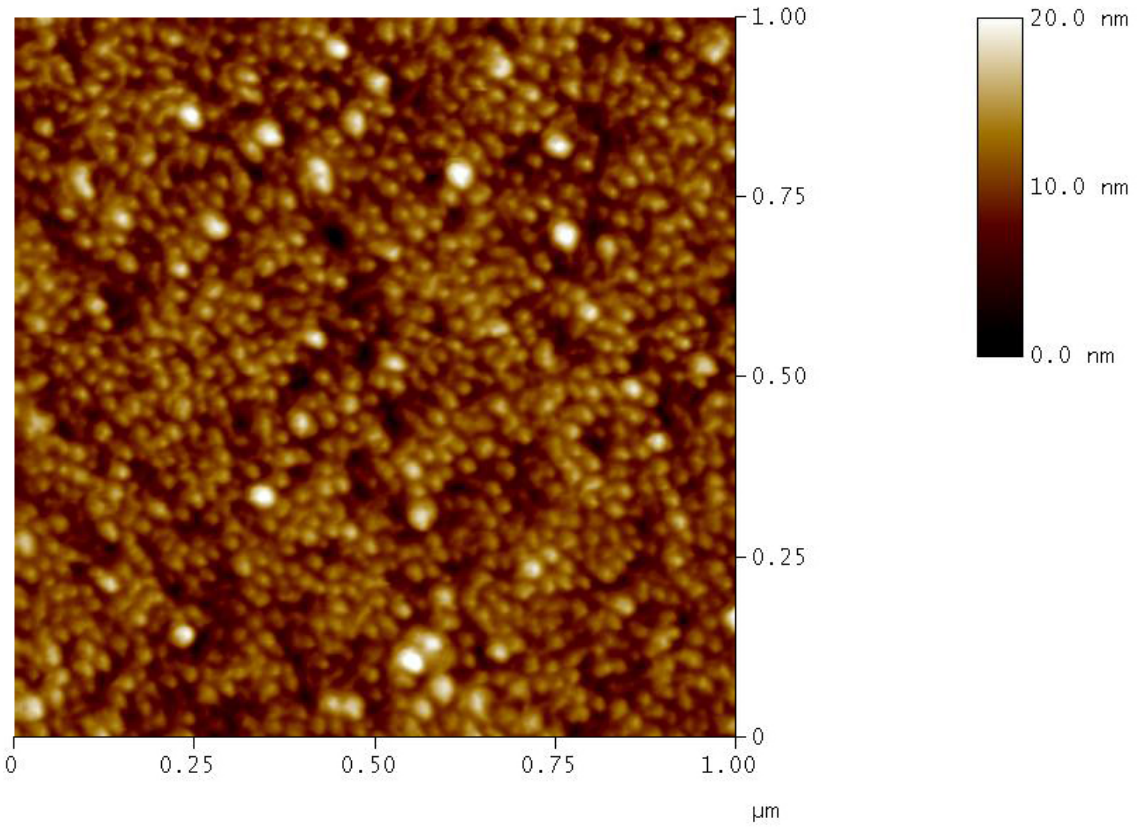

Figure **2-1**: Atomic force microscope topographic map of the surface of a platinum sample. This surface has an RMS of 2.615nm and is optically pristine. The surface features shown were measured to be ~10nm and are not indicative of the grain size in the interior of the film.

2.1.2.2 X-Ray Diffraction Analysis of Grain Orientation

Atomic force microscopy did not provide sufficient details about the orientation of the platinum grains. One method which was used to analyze the interior of the film was X-ray diffraction (XRD). This section will provide some details and results of XRD testing of the platinum films which were still adhered to the silicon substrates.

X-ray diffraction (XRD) was used to characterize the texture of the Pt film. A theta-theta scan (10 to 120º, step size 0.02º, count time of 2.5 seconds) using a quartz sample holder (cut 6 degrees of the c-axis so as not to produce any peaks in the measured range) was conducted using a Scintag model X2 with copper Kα source. The resulting spectra shown in Figure **2-2** overlays both the theta-theta scan (shown in black) and the grazing angle scan (shown in blue). At the bottom of the spectrum are predicted peak locations for platinum (marked in red), and predicted silicon peaks (blue). Results indicated the platinum film to be primarily (111) oriented (having dominant (111) and (222) peaks) with some (311) and (331) orientation. The (311) and (331) orientations both show up more predominantly in the grazing angle scans, which may mean that grains nearest the top of the film are more likely to differ from the (111) orientation. The silicon substrate is (100) oriented, and the titanium layer could not be characterized because its peaks overlapped the dominating platinum peaks.

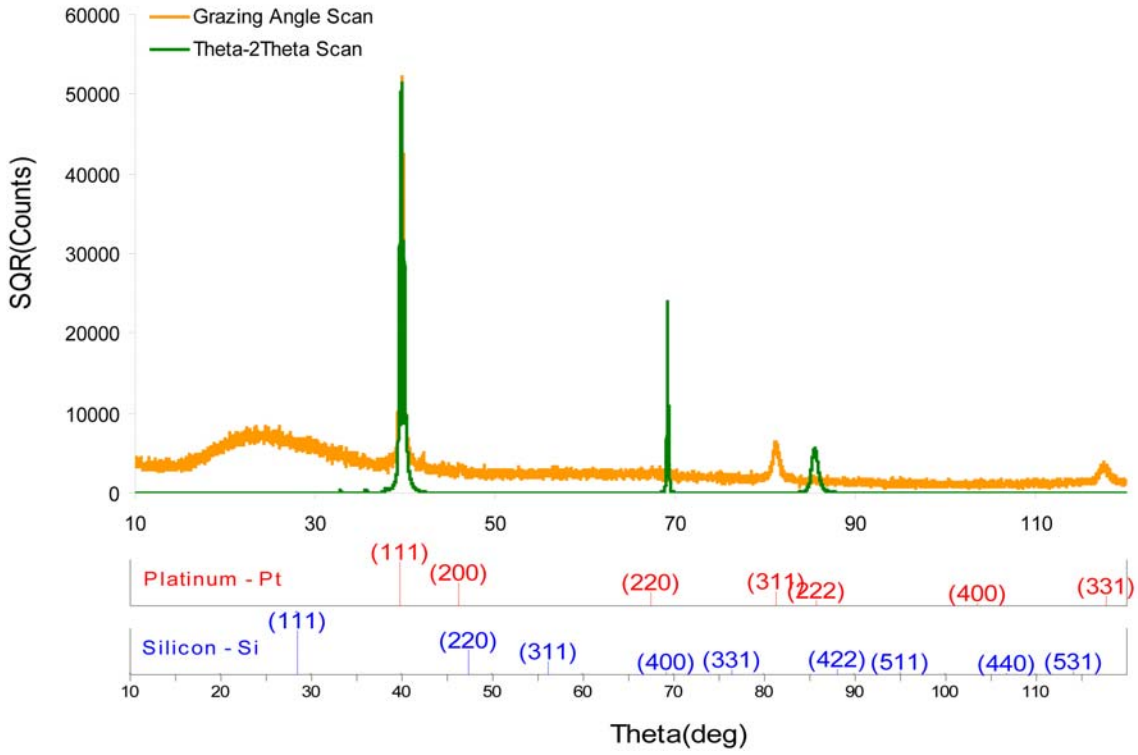

Figure **2-2**: X-Ray Diffraction pattern of a theta-theta scan on the TiPt sample on a silicon substrate. This scan shows 3 primary peaks, two attributed to the (111) orientation of the platinum grains, and 1 attributed to the (100) orientation of the silicon wafer.

2.1.2.3 Transmission Electron Microscopy Analysis of Texture

Having established the orientation of the platinum grains is a major, but not final step in characterizing the texture of the film. In order to get information regarding the size and distribution of grains, an additional characterization method was used. Transmission electron microscopy (TEM) was used on platinum films still attached to the silicon substrate after the samples has undergone processing to be thinned down to electron transparency. This section will provide some details and results of TEM testing.

The nanostructure and chemistry of the Pt films were evaluated with the help of Trevor Clark, using two 200kV JEOL TEM that were outfitted with energy dispersive spectrometers (EDS): 1) a JEM 2010F, equipped with a field-emission electron source, STEM unit and Gatan Enfina electron energy loss spectrometer (EELS) and 2) a JEM 2010 equipped with a LaB_6 emitter. Electron transparent cross-sections of the film were produced with assistance from Josh Meier by using conventional mechanical and ion milling techniques in which sections were polished to approximately 10 μm thickness using a succession of diamond lapping film ranging in grit from 30 to 1 μm. After adhering the polished section to a copper TEM grid, a Gatan model 691 precision ion milling system was used to perforate the film, creating a thickness gradient emanating radially such that areas nearest the hole were electron transparent, and samples furthest from the hole retained their full thickness. Samples were then plasma cleaned for 10 minutes prior to evaluation to minimize carbon contamination of exposed surfaces.

TEM analysis on areas which were not fully electron transparent confirmed a thickness of about 450 nm for the film (Figure **2-3**). Analysis on electron transparent sections revealed a columnar grain structure with grains measured by point to point comparison to be roughly 25 to 40nm in diameter (Figure **2-4**). Close inspection of platinum grain boundaries did not reveal any voiding or cracking (Figure **2-5**). Diffraction patterns acquired at this magnification indicate a lattice spacing of 2.26nm, matching a (111) structure in the platinum film (Figure **2-6**) [56].

EDS spectra were acquired for 1200 seconds in several grain boundary locations within the film. These scans were focused on identifying the grain boundary segregation of species such as Ti, Si, and their oxides and compounds in the nanograined Pt (Figure **2-7**). These scans found platinum to be the only element detected within grain boundaries, when sampled near and far from the titanium adhesion layer.

EELS spectra were acquired in several locations in the platinum sample, including with grain boundaries. This technique identified titanium only within the region corresponding to the titanium adhesion layer. Silicon, carbon, oxygen, xenon and titanium were below detection limits when sampling within the platinum layer (Figure **2-8**).

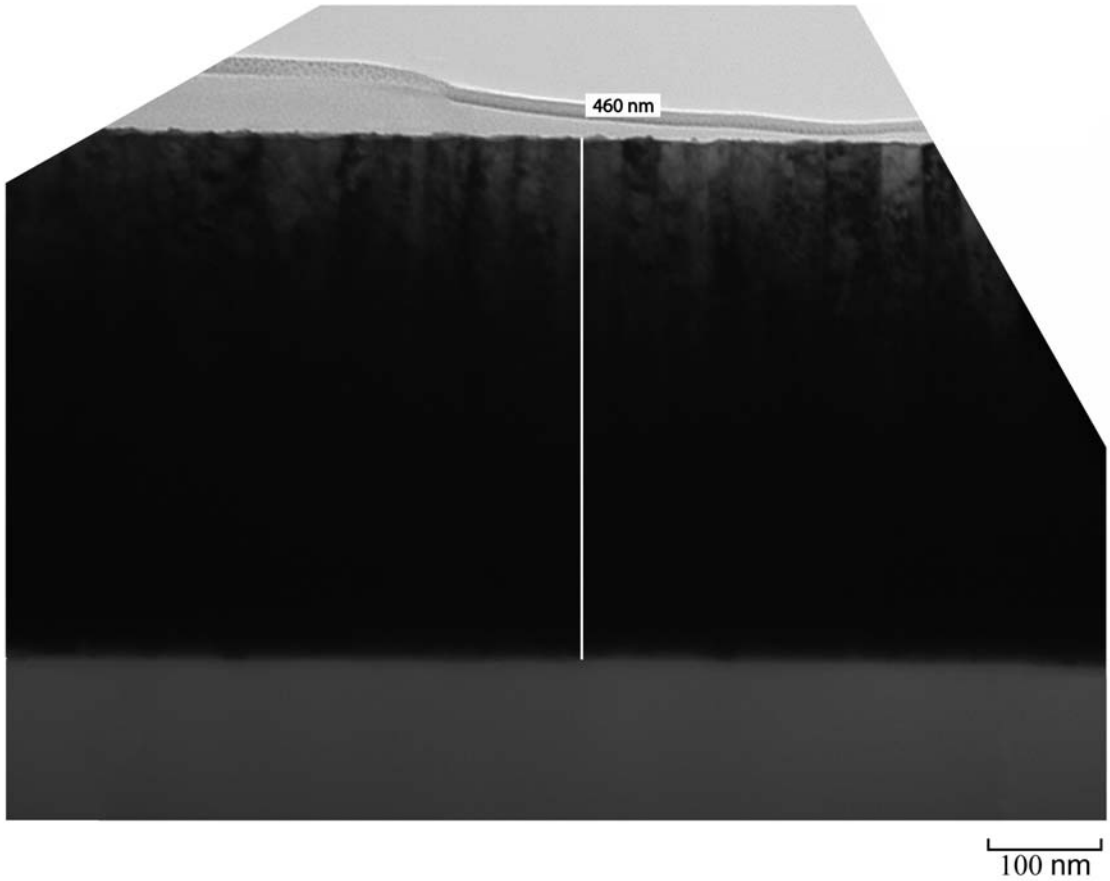

Figure **2-3**: Transmission electron micrograph of pt sample which has not been thinned down. This micrograph shows the full thickness of the film. The layer at the top of the film is a residual epoxy used in the sample preparation.

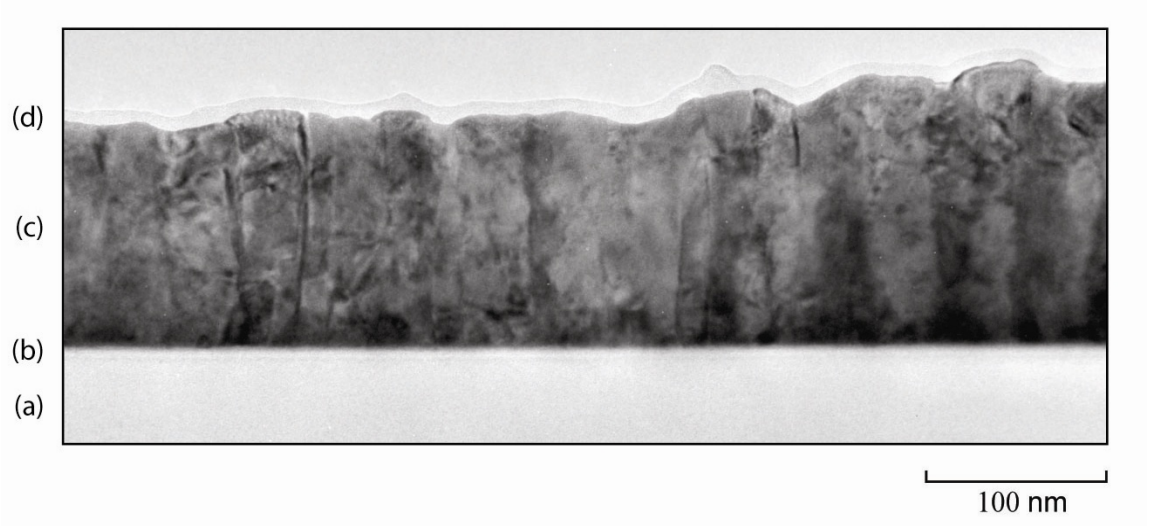

Figure **2-4**: Transmission electron micrograph of a Pt sample on Si substrate that has been thinned down to electron-transparency (hence not showing full thickness). Sections (a) show the Si substrate, (b) the titanium adhesion layer, (c) the 25-40 nm diameter, nanoscale, columnar Pt grains and (d) an adsorbed oxygen layer from the thinning process.

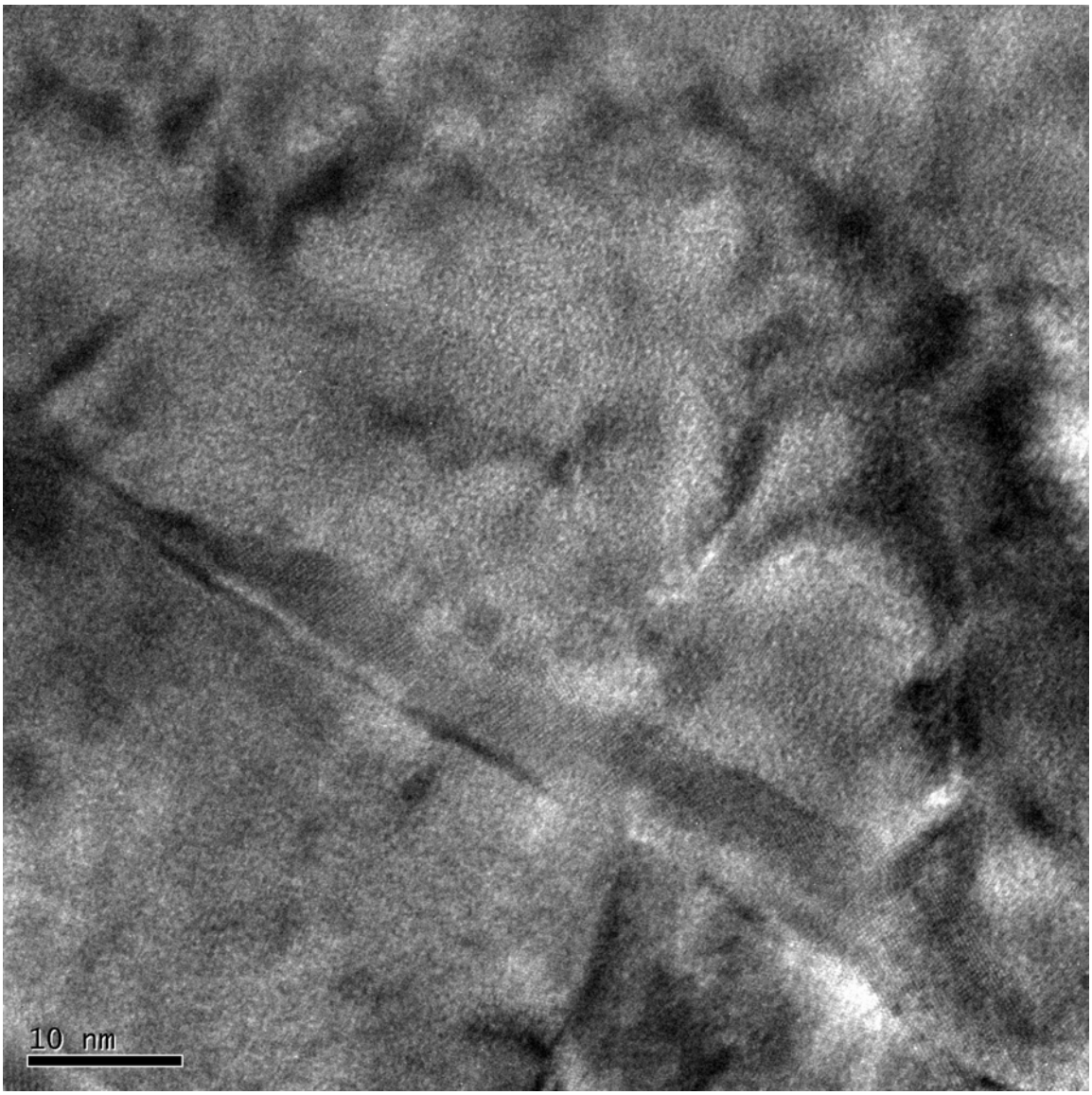

Figure **2-5**: Transmission electron micrograph of a platinum grain boundary within a TiPt thin film. Lattice fringes can be seen nearest the grain boundary. No significant volume of voids can be seen.

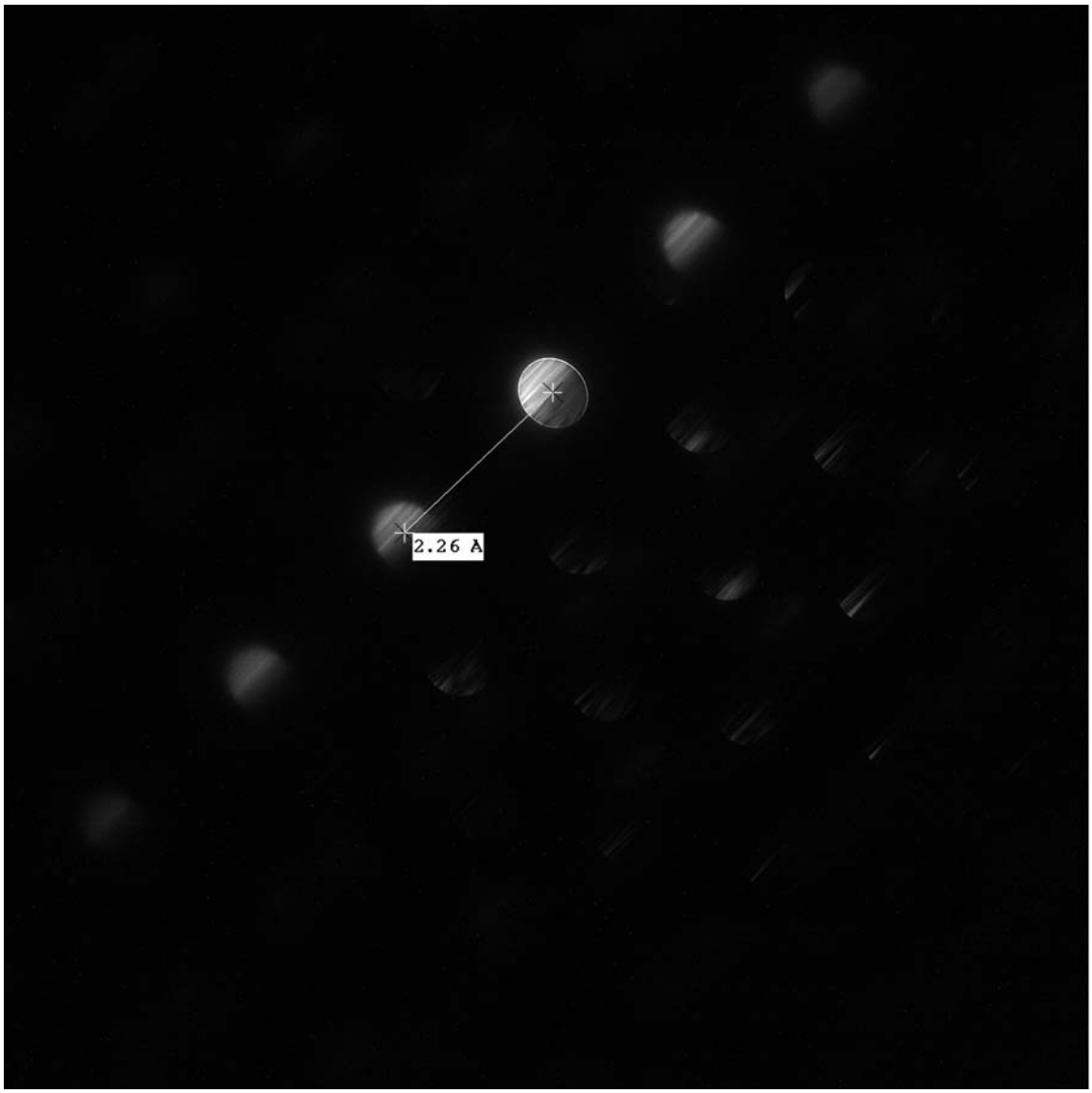

Figure **2-6**: Platinum diffraction pattern produced in the TEM indicating a (111) structure in the platinum film.

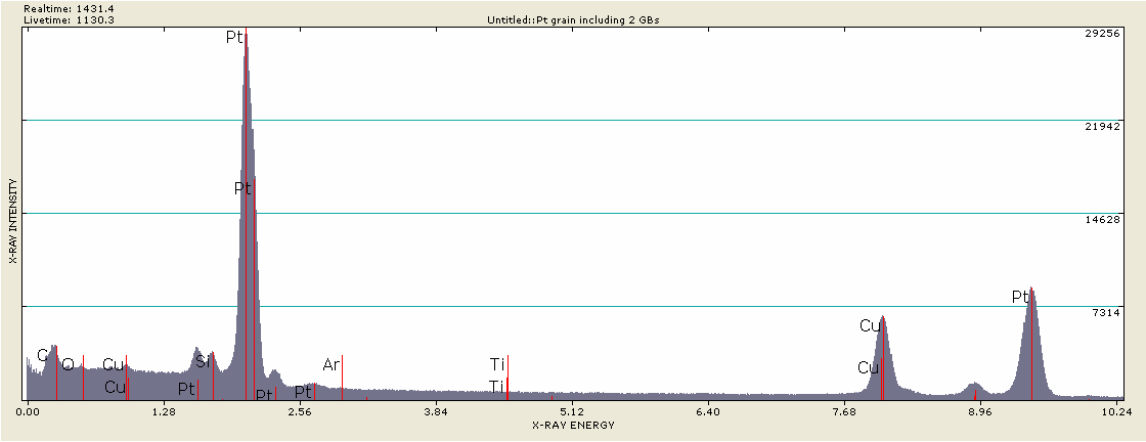

Figure **2-7**: Energy dispersive spectrometry (EDS) of the film confirmed the presence of the Pt structural film and the Ti adhesion layer. Additional spectra collected within the grains, along grain boundaries, and near the Ti adhesion layer interface identified Pt as the only element present, within the 0.1 atomic % detectability limit of the techniques.

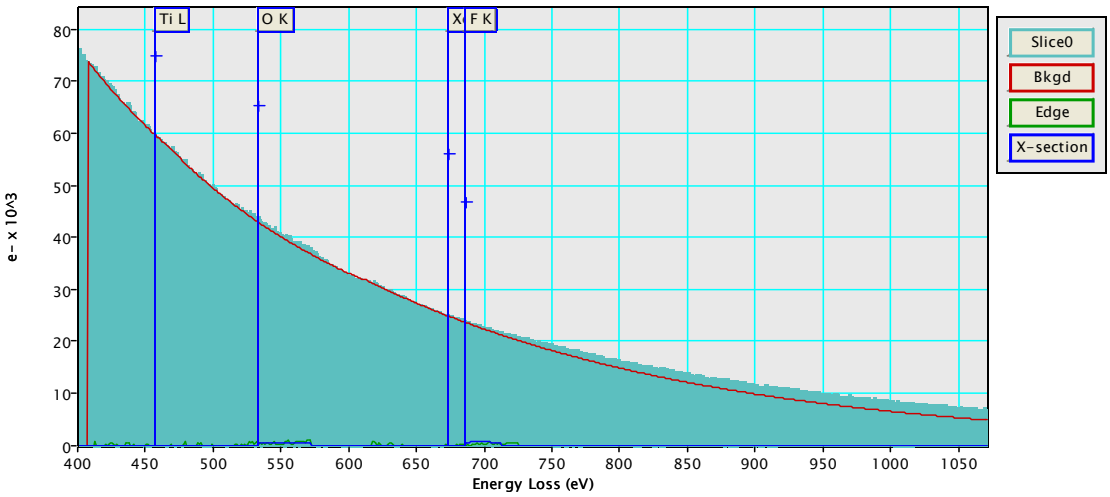

Figure **2-8**: EELS Spectra of platinum grain boundary near the titanium adhesion layer. No titanium, xenon, oxygen or fluorine was detected.

2.1.2.4 Secondary Ion Mass Spectrometry Analysis of Trace Elements

Although EDS and EELS are both very accurate methods of analysis for detecting the presence of elements, secondary ion mass spectrometry (SIMS) has comparable resolution for trace elements, and has the distinct advantage of sampling the entirety of the film, whereas EDS and EELS are both localized measures. Platinum samples were sent Evans Analytical Group in East Windsor, NJ to acquire concentration depth profiles of all elements present within a section of film still adhered to the substrate. This section will provide some details and results of SIMS testing of the platinum thin films still adhered to the silicon substrates.

A Quadrupole Mass Spectrometer was used in two different runs such that both positive ions and negative ions could be evaluated (see Table **2-5** for parameters). Ions selected for SIMS analysis were based on their likelihood of being present. Xenon and fluorine were selected based on their use as an etchant, carbon and oxygen were selected due to the predominance in ambient environments.

Both positive (Figure **2-9**) and negative (Figure **2-10**) ion analysis showed that all measured elements were present at or near the detection limits of the instrument. From the surface, the initial 50 nm had erroneously high values of all measured quantities as a result of normalizing counts; this normalization was not complete until a certain number of counts was reached, resulting in an erroneous high contamination count near the surface which quickly stabilized, at a baseline value at around 50 nm. Between 50 and 400 nm, values of all measured species, carbon, fluorine, oxygen, titanium and xenon were steady or decreasing and were present at or below the detection limits of the instrument for the elements. The detection limit for each element is different, but varied between 10^{17} atoms per cm^3 and 10^{18} atoms per cm^3, equivalent to about .1 and .01 atomic percent. Although the titanium layer was first exposed at 430 nm, mass interference effects on other measured elements began to show around 400 nm. Although it is possible that some titanium has diffused into the platinum layer, or that the platinum layer is not as thick as predicted, the most likely explanation is that the crater associated

with the destructive sputtering of the sampling was not uniformly flat causing some portion of the titanium layer to be exposed while still registering an average crater depth shallower than the minimum depth. Between 430 and 450 nm, titanium peaks, causing peaks in all elements due to mass interference, particularly in the negative ion scan. Below 450 nm, all elements but silicon quickly ebb. The sample to sample variation of concentration measurement of the SIMS analysis was reported to be approximately 20 percent. The instrument was calibrated against NIST traceable reference standards for silicon, and results for other materials are typically calibrated against consensus standards in those materials, however, no such standard exists for platinum.

Table **2-5**: SIMS Sampling Parameters

Condition Number	1	2
Secondary Ion Polarity	Negative	Positive
Elements Monitored	C, O, F	Xe, Ti
Primary Ion Beam	Cs	Cs
Primary Ion Energy	4keV	4keV
Incident Angle	60°	60°
Oxygen Leak	No	No
Charge Neutralization	No	No
Surface Conductive Coating	None	None
Liquid Nitrogen Cold Trap	No	No

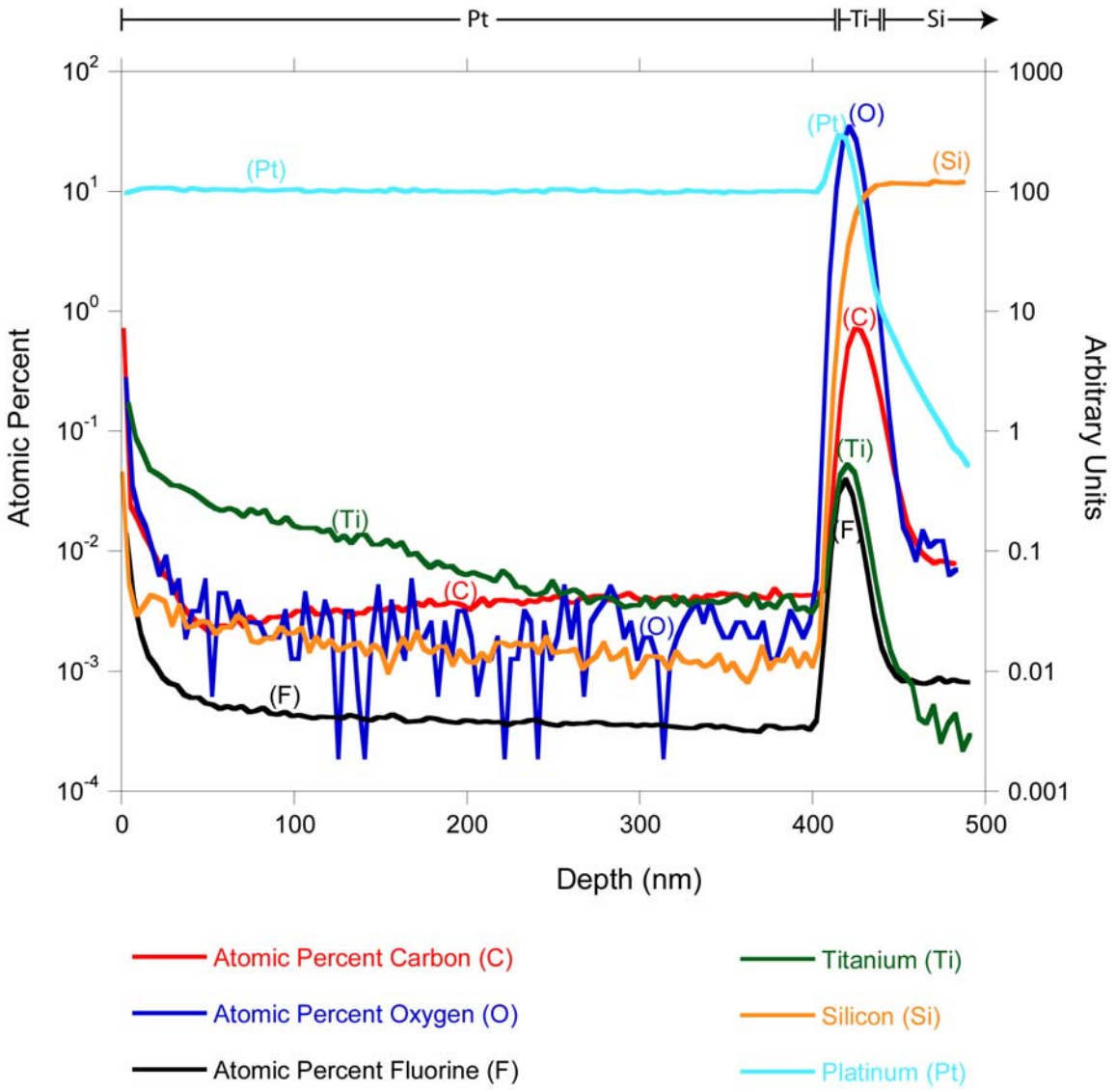

Figure **2-9**: Negative ion analysis by SIMS is best for detection of carbon, fluorine and oxygen, although they are all influenced by the presence of titanium [57] – this effect is characterized by false peaks at around 440nm (the center of the titanium layer). These results confirm that carbon, fluorine and oxygen are only present at or around the detection limits of the instruments. Platinum, silicon and titanium are plotted on arbitrary units, normalized with respect to silicon counts.

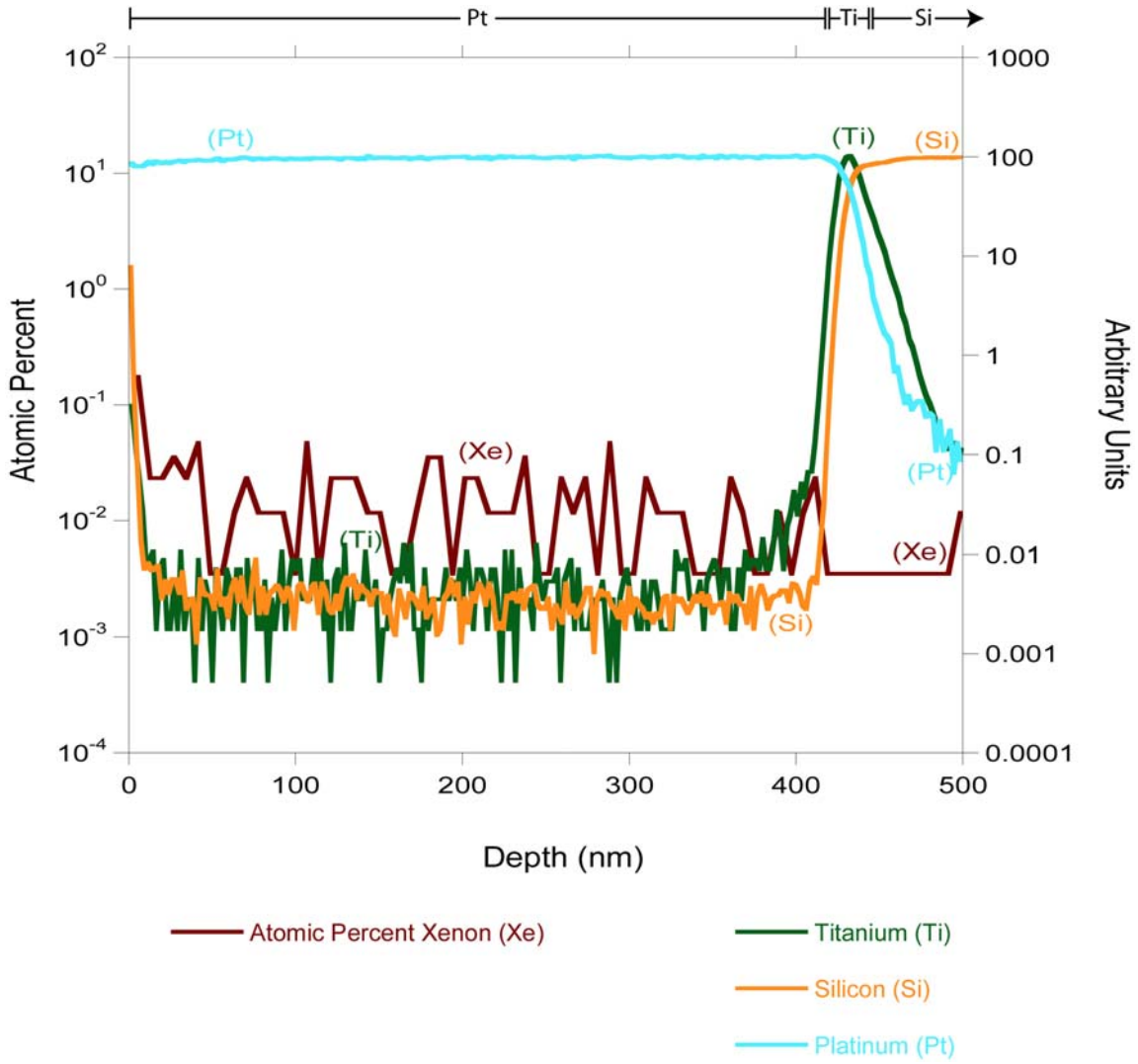

Figure **2-10**: Positive ion analysis by SIMS is best for detection of titanium and xenon [57]. These results confirm that xenon is only present at or around the detection limits of the instruments within the platinum layer. Platinum, silicon and titanium are plotted on arbitrary units, normalized with respect to silicon counts.

2.1.2.5 Summary of Material System Characterization

Several characterization tools were used in order to evaluate the films used in this study. Using TEM, it was established the platinum films were 430nm of platinum on top of a 20 nm titanium layer. Using AFM, the top platinum layer was to found to have an RMS value of 2.615 nm. Using TEM and XRD, the platinum was found to be nanocrystalline, with columnar grains roughly 25 to 40nm with a primarily (111) orientation. EDS, EELS, and SIMS confirmed that the platinum films were free from contamination to the resolution of the instruments. The following section will conclude detailing the films in detailing the specimen geometry.

2.1.2.6 Geometry

The geometry of the tested specimens is of crucial importance for both testing conditions and data analysis. The mechanical properties of the platinum films were investigated using sample geometry and testing methods that were established for uniaxial tension-tension of macroscopic specimens in ASTM E 647 [58]. This section will provide details regarding the geometry of the specimens used in this study.

The tensile and fatigue properties were measured using center cracked sheet specimens that were freestanding at one end and bound to a (100) single crystal silicon substrate at the other. Figure **2-11** shows a scanning electron microscope image of the sample, along with a close up of the gage section highlighting the notch. Gauge sections were 2 mm long, having 200, 160 and 100μm widths, and slots with semicircular ends which spanned 33% of the gauge widths and had a 3μm root radius. The thickness of the films was reported to be 480nm of platinum on top of a 20nm titanium adhesion layer, however, TEM, SIMS and cross-sectional scanning electron microscopy indicated the thickness of the film composite to be 450nm, and this value was used in all calculations.

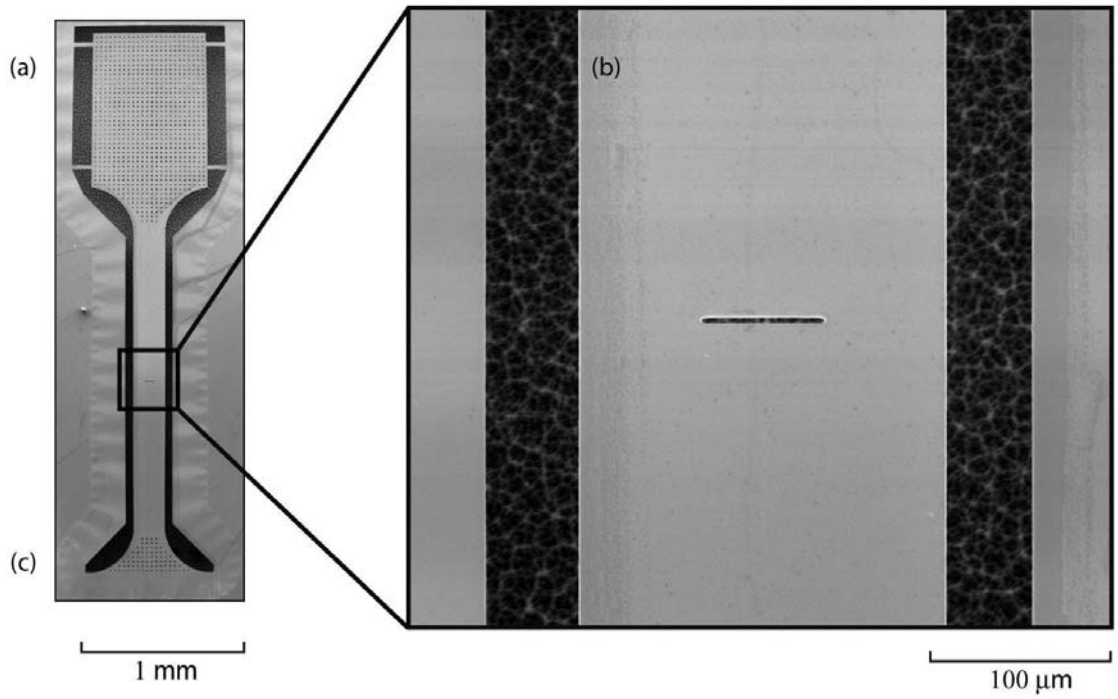

Figure **2-11**: A scanning electron micrograph of a center-cracked sheet fatigue crack growth characterization specimen showing (a) the free standing grip section with tethers, (b) the free standing gauge section with slot, and (c) the 'anchor' portion attached to the substrate.

2.2 Mechanical Testing System

In order to characterize the mechanical properties of nanocrystalline platinum thin films, a mechanical testing system was designed. The testing system comprises of three main parts: a displacement stage, a load cell, and a camera. Although these main systems parts have remained the same, several periphery accessories have undergone many changes over the course of this study in order to make improvements to the setup. Before a sample can be tested in either tension or fatigue, the specimen must be detached from the tethers binding it to the substrate, it must be gripped, and it must be tested under controlled conditions, while several parameters of interest are monitored and recorded. The following is a detailing of the steps which were followed in order to test each specimen. In following with the description of the system, refer to Figure **2-12** for a basic schematic of the setup.

In all testing cases, the 4 tethers connecting the substrate to the film were broken prior to testing. In some cases, these tethers were broken prior to gripping the sample using a tungsten probe with a 20 μm tip diameter, and in others the sample was first gripped, and then the tethers were broken by the tensile forces applied to them by the slight motion of the specimen away from the substrate. This second method greatly reduced the number of samples damaged by tether breaking, or lost in the transfer between the probe station to the testing system. Details regarding which method was used, as well as several test-specific parameters are presented in Table **2-6**.

The silicon chip containing the samples was adhered with double sided (Scotch™) tape to a piezoelectric translating stage (PI P620) providing a total of 250 μm of displacement with sub nanometer resolution, in turn mounted on a 3 axis stage capable of tilt, pitch and rotation (Newport PO80N). The displacement stage was controlled by a closed-loop external conditioning box (PI E-665) which allowed digital or manual control of the stage. A 200 μm diameter optical fiber or 20 μm tip diameter tungsten needle (see Table **2-6**) was affixed to a gripping fixture, the head of an Icy Pentel 0.5 mm lead pencil for the fiber, and a pin-jack probe holder (American Technologies 745-SAI) for the

needle. Initially, the optical fiber was used because it was thought that the transparency of the fiber would be conducive to curing regions of the glue underneath the fiber, however, it was discovered that the curing system was sufficiently powerful to cure all regions of the glue, even when using an opaque needle. The transition to the needle was also advantageous in creating a stiffer load train, and thus lowering system compliance. The gripping fixture was in turn connected to either a 10 gram load cell (Transducer Techniques GSO-10) capable of force measurements with 0.005 N resolution or a 50 gram load cell (Sensotec Model 31) capable of force measurements with 0.0005 N resolution (Table **2-6**). This transition was made for the advantageous higher capacity and resolution of the second load cell. The load cell and attachments sit on top of two stages (Edmund Optics NT56-339, NT55-028) capable of three orthogonal displacements and rotation about the vertical axis. The sample was aligned with the grip system using all the available axes of freedom so that a uniaxial loading mode will result.

Initially, samples were mounted directly onto the flat surface of the displacement stage, i.e. at a 0° offset from the needle. Although this was thought to be ideal for the application of pure tensile forces, it was difficult attaching the fiber to the sample. The initial solution was to mount the fiber at an angle and owing to the high compliance of the fiber, the fiber and sample system would realign when stressed, thus bending the sample at the film/substrate hinge. Although this was not ideal, because no deformation was ever seen at this hinge, the results were still considered valid. However, when the transition was made to the needle, its holder did not allow for it to be mounted at an angle. As a solution to this problem, an adapter was developed so that chips could be mounted at a 10° offset from the needle (Appendix A). UV-adhesive glue (Dymax OP-24-REV-B) was applied to the tip the fiber or needle. It was then lowered on to the free-floating gripping region of the dog-bone. A hand held UV spot curing system (Electro-Lite ELC-410) was used for 2 minutes to completely cure the glue. The sample was then realigned by raising the sample to the point where it is flat, resulting in the ability to apply purely tensile forces.

A high resolution monochrome CCD digital camera (Pulnix TM-9701) connected to an image acquisition card (National Instruments NI PCI-1422) which sits on top of two

stages (Newport m-562, Newport 813S) and damping rod (Newport 45) so that 5 axes of tilt and translation allowed the camera to be positioned perpendicular to the surface of the gage section of the sample. Long working distance Mitutoyo infinity-corrected long working distance lenses (Edmund Optics NT46), either 20× objectives having a resolution of 0.7 μm, or a 100× objectives having a resolution of 0.4 μm, were used in conjunction to the camera in order to image and record the region of interest (Table **2-6**). The objective lenses were attached to the camera via an additional stage (PI P-725.2CD) which allowed vertical displacement of the objective lens using a signal sent from an external conditioning box (PI E-665). This attachment allowed the user to change the focus of the objectives whenever necessary without disturbing the system. An image of the region of interest was recorded for later calculation of the crack lengths during testing (Table **2-6**). Coaxial illumination for the camera was provided by a variable intensity light source with fiber-optic guide (Dolan-Jenner DC950). The entire system was situated on top of a bench top vibration isolation system (Minus K BM-4). After fatigue test 2, an unexpected power failure caused the abrupt failure of a fatigue test; as a result all electronic instruments were subsequently plugged into an uninterruptible power source (Tripp-Lite SU3000XL) to prevent power outages from ending tests.

The testing software was developed in LabView 7.0, with certain portions of code, primarily those developed for the control of the camera, developed by James Collins. The program controlling tensile tests was based on sending voltage signals to the displacement stage's conditioning box at quick successive intervals. The conditioning box used the voltage signals in order to determine a target displacement, and set the voltage required to do so in a closed loop format in real time. This process caused a smooth ramping of the displacement stage away from the load cell, effectively loading the sample in tension. The program was capable of accepting user input for ramp rate, and frequency of imaging. The program recorded load cell output for each displacement increase, along with user specified input. The program controlling fatigue testing has undergone numerous evolutions. Initially, the program was capable of accepting user input for frequency and displacement and was run in displacement control, in a similar fashion to the tensile test described above. The latest version of the software runs in force

control, taking voltages from the force transducer to calculate appropriate motion of the displacement stage, and allows several user parameters to be entered, including force amplitude, mean force, frequency when cycling, frequency when recording, number of data points to be recorded and frequency of recording of data and images. Figure **2-13** is a simplified flowchart of program logic followed during a tensile or fatigue test.

Typically, as cracks grow during a fatigue test, samples become more compliant. This increase in compliance during a displacement controlled test is an effect known as load shedding. The resulting progressive decrease in force amplitude affect the driving force for crack progression and in turn can lead to a reduction in crack advance rate or crack arrest entirely. This effect is seen very prominently in samples which exhibit gross plastic deformation. Fortunately, neither gross plastic deformation nor load shedding was a problem in the fatigue testing of platinum; this was confirmed by recording maximum and minimum forces during fatigue tests, and is later explained in the compliance analysis section and the crack growth rate section. The first 3 tests were run using this program (Table **2-6)**, recording displacements, forces and images as specified. A major evolution of this program occurred when testing of gold samples (not reported in this thesis) was hindered by severe plastic deformation of the sample. The program was modified to be load controlled. The latest version of the program controlled the displacement automatically in order to match the desired parameters. The load control card (National Instruments NI PCI-7340) used the voltage signal of the load cell and several feedback parameters (Table **2-7**) as input in order to calculate an appropriate output signal to the displacement stage conditioning box, all in real time. The latest version of this program was capable of accepting user input for frequency, mean load, load amplitude and imaging parameters and outputs entire waveforms for displacement and forces, as well as images, all at user specified intervals.

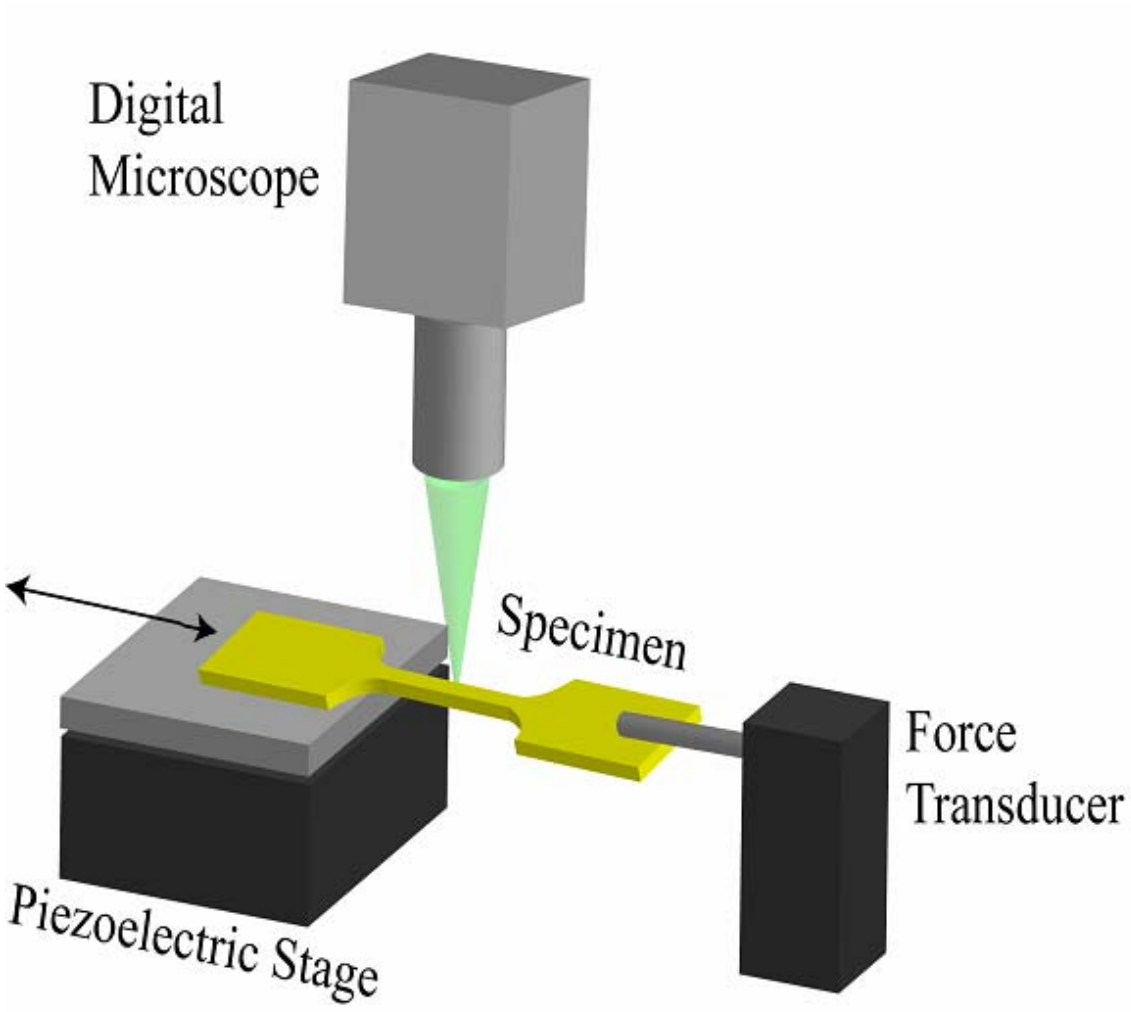

Figure **2-12**: A basic schematic of the testing system showing the 3 major components of the system, a piezoelectric displacement stage to which the specimen die is affixed, a force transducer connected to the sample via an optical fiber or a needle, a digital microscope capable of imaging and recording the region of interest in real time.

Table **2-6**: Test Specific Parameters

Parameter	**Tensile Test**	**Fatigue Test 1**	**Fatigue Test 2**	**Fatigue Test 3**	**Fatigue Test 4**
Load Cell	GSO-10	GSO-10	GSO-10	GSO-10	Sensotec Model 31
Load Readout	SCXI	SCXI	SCXI	SCXI	Load control card
Lens	20×	20×	20×	100×	100×
Control Mode	Displacement	Displacement	Displacement	Displacement	Load
Grip	Optical Fiber	Optical Fiber	Optical Fiber	Needle	Needle
Incline	0°	0°	0°	-10°	-10°
Image Frequency	1 micron of displacement	30 seconds	Cycle	60 cycles	300 cycles
Rate	.1 μm/s	-	-	-	-
Loading Frequency	-	1 Hz	1 Hz	1 Hz	1 Hz
Load ratio	-	0.1	0.1	0.1	0.1
Loading wave	Linear ramp	Sine	Sine	Sine	Sine
Gage Width	150	200	150	100	100
Ambient Environment	Air	Air	Air	Air	Air
Temperature	22±2°C	22±2°C	22±2°C	22±2°C	22±2°C

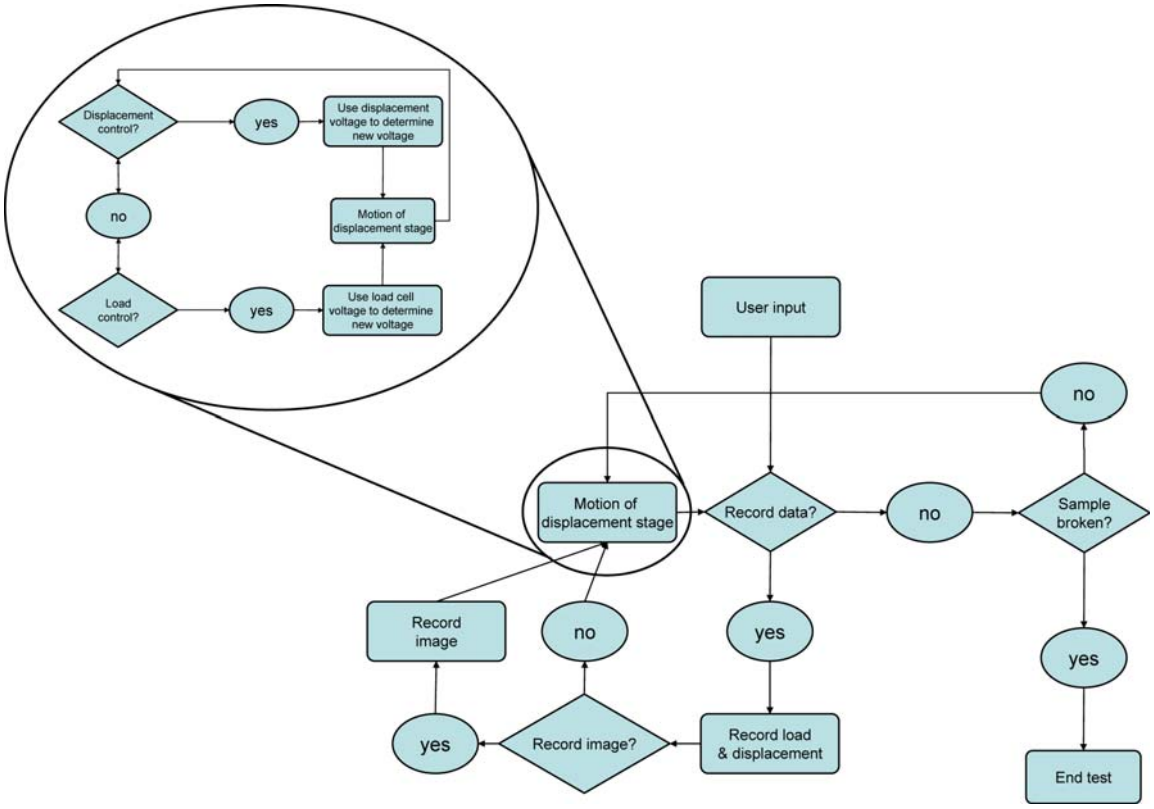

Figure **2-13**: Basic flowchart of program logic followed during a tensile or fatigue test. Program begins with user input, records initial load, initial displacement, and initial image, then changes the motion of the displacement stage based on load or displacement control, either in a ramp or cyclic fashion, records data at regular intervals until the sample breaks.

Table **2-7**: Feedback Parameters

Proportional Gain, Kp	5
Integral Gain, Ki	20
Integration Limit, IL	1000
Derivative Gain, Kd	0
Derivative Sampling Period, Td	0
Velocity Feedback Gain, Kv	0
Velocity Feedforward, Vff	0
Acceleration Feedforward, Aff	0

2.3 Analysis Methodologies

The raw recorded data (i.e. displacements, forces, and images) produced during the tests allowed for the examination of some of the basic behaviors of the films. Several analysis tools and formulas were used to organize the raw data into constitutive relationships. Analysis of data was largely performed in Excel® 2002 a spreadsheet application from Microsoft. All final curves were graphed and fitted using Levenberg-Marquardt algorithm of version 3.52 of Kaleidograph®, a data analysis and graphic presentation software tool from Synergy Software. The following section will detail how data was analyzed.

2.3.1 Tensile Testing

All platinum samples having no notches and which were tested in displacement control failed outside of the gauge section, presumably due to stress concentrations resulting from too high a filet angle (Figure **2-14**). It should be noted that this problem was addressed in future fabrication of different films by the reduction of the taper angle. In order to overcome the fact that the platinum samples would not fail at the gauge section, a notched platinum sample was tensile tested. The stress concentration provided by the notch overcame other flaws in the material and resulted in proper fracture in the gauge. The test was run in displacement control, at a displacement rate of 0.1 μm per second, in lab air (22±2°C). Due to the uniaxial tension nature of the experiment, stress was calculated by simply dividing the applied force by the cross sectional area of the gauge and by multiplying the applied nominal stress by the stress concentration factor of the notch. The stress concentration factor of the notch was both calculated by finite element modeling and confirmed by experimental photoelastic testing to be roughly equal to 5 [59]. This value is valid for elastic strain only, and as such, represents an upper bound for the stress concentration of the notch.

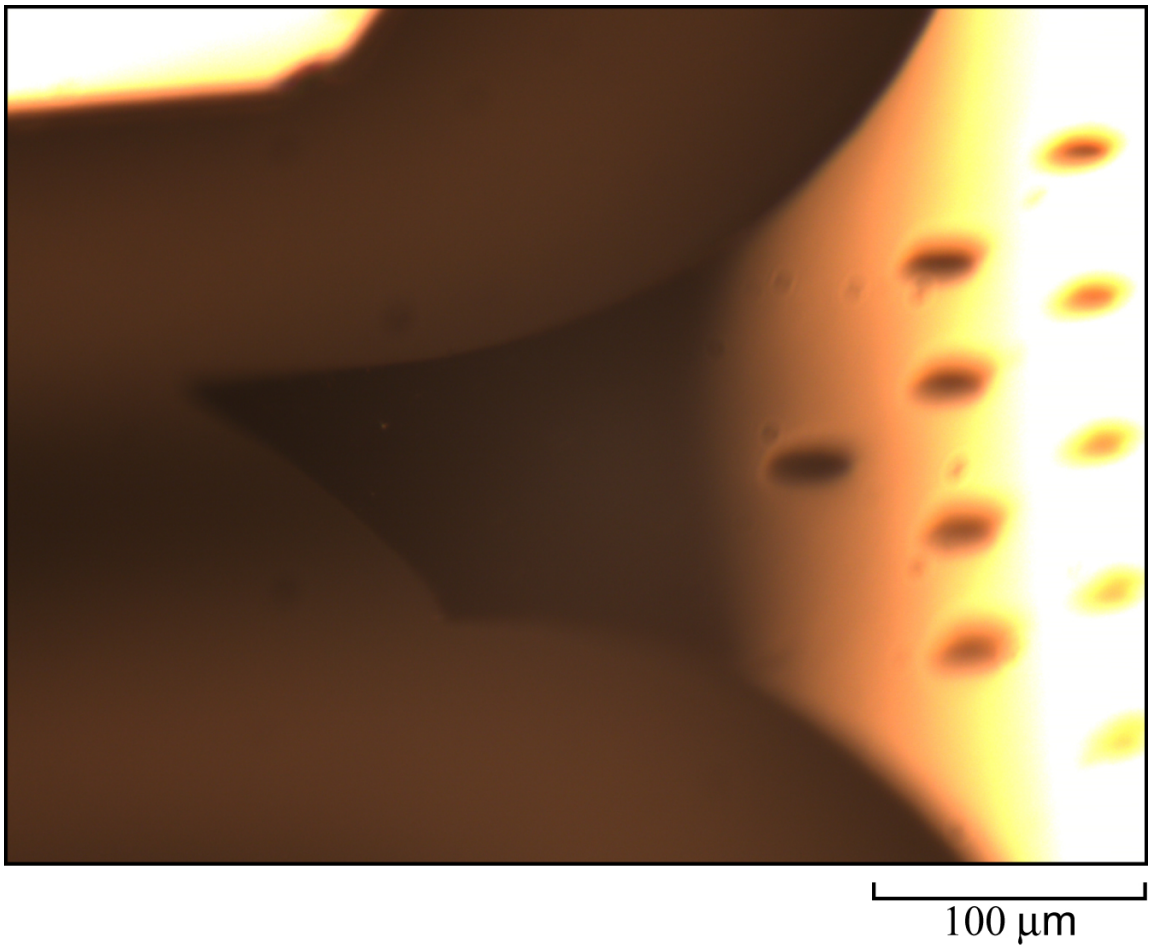

Figure **2-14**: Failure outside of the gauge section, typical in platinum samples which were not notched. The distorted light reflections are strictly a result of the specimen not being parallel to the plane of the camera (i.e. it is out of focus).

2.3.2 Fatigue Testing

Four constant stress amplitude (load ratio $\sigma_{min}/\sigma_{max}$, R = 0.1, sinusoidal, 1 Hz) fatigue tests were conducted in laboratory air (22±2°C). In order to quantify the fatigue crack growth behavior of the samples, several components of the behavior were measured and/or calculated. The following section will detail how crack lengths were measured, and how stress intensities, crack growth rates, and crack closure were calculated.

2.3.2.1 Crack Length Measurement

The measurement of crack lengths is a vital part of fatigue testing for several reasons. Crack length measurement allows for accurate assessment of stress intensities and crack growth rates, but also provides a good check for test progress and specimen response. Making an accurate measurement of crack length can be achieved by two methods: optical comparison, and compliance. The following sections will describe how both of these methods were used to measure crack length for the fatigue tests reported on in this study.

2.3.2.1.1 Optical Measurements of Crack Length

Images captured for the duration of the test allowed for measurement of crack growth by optical analysis. This method is lens-specific and has a maximum resolution of 4 pixels (2 pixel from each measured end), which at the highest lens objective (100×) correlates to 500 nanometers, close to the resolving power of the lens itself. Although this method has a very high theoretical resolution limit, it should be noted that long before this resolution limit is reached, the objectiveness of the user in determining the length to

be measured comes in to play – the user must decide what he believes he should be measuring, which arguably, has a significantly higher error given picture quality, sub-surface cracking and human error.

By opening an image in Photoshop® CS2, a measurement can be taken of any line length. This measurement, in pixels, can be correlated using a known pixel-meter conversion which was found using a plate stage micrometer (VWR #82026-613) having a 0.05 micron resolution. This was performed on numerous images acquired during fatigue tests. In order to select a decent sample size from the many images acquired during each test, images were selected such that there was a measurable crack advance, i.e. at least one pixel of advance (equaling a 250 nanometer crack extension), between two consecutive analyzed images.

2.3.2.1.2 Compliance-Based Measurement of Crack Length

As cracks advance through a material, its compliance changed. By recording the compliance of the platinum samples as it varied through the test, it was possible to correlate the compliance value to a crack length. Compliances of the specimen and system were calculated by fitting a slope through a plot of force vs. displacement comprised of all (one hundred) recorded data points within the initial fatigue cycle. Raw measured values of compliance showed the compliance of both the system and the sample together.

Theoretical compliance of the specimen only was found using Equation **3**, a solution provided by Tada et al [60]:

$$C = \frac{1}{BE}\left[\frac{2a}{b} \times V_2\left(a/b\right) + \frac{h}{b}\right] \qquad \mathbf{3}$$

where a = crack length (initially ½ notch width), b = ½ gage width, h = ½ gage length and $V_2\left(a/b\right)$ was found using Equation **4**, another solution provided by Tada et al [60]:

$$V_2\left(a/b\right) = -1.071 + 0.250\left(a/b\right) - 0.357\left(a/b\right)^2 + 0.121\left(a/b\right)^3 - 0.047\left(a/b\right)^4 + 0.008\left(a/b\right)^5 - 1.071\frac{1}{a/b}\ln\left(1 - a/b\right) \qquad \mathbf{4}$$

By subtracting the theoretical value of specimen compliance from the measured compliance, system compliance was determined to be 5.42×10^{-5} m/N. By subtracting out the system compliance from the measured compliance, the initial value of measured compliance matches the theoretical value of specimen compliance. By multiplying the measured values of compliance by a constant, in our case, equivalent to multiplying the values of thickness and elastic modulus by 0.47, it was possible to match the theoretical compliance with the experimental compliance to a close degree. Using the measured compliance after correction, a value of crack length can be estimated from each value of compliance measured (Figure **2-15**), however, the error for the estimate is dependant on the crack length, that is, error was initially large, and decreased as crack length increased. Values of compliance for the specimen showed that the initial platinum compliance was 1.33×10^{-4} m/N, and progressed throughout the test, ending at 1.40×10^{-4} m/N. This small change of compliance is the main reason why load shedding was not a significant problem in displacement controlled fatigue testing of the films.

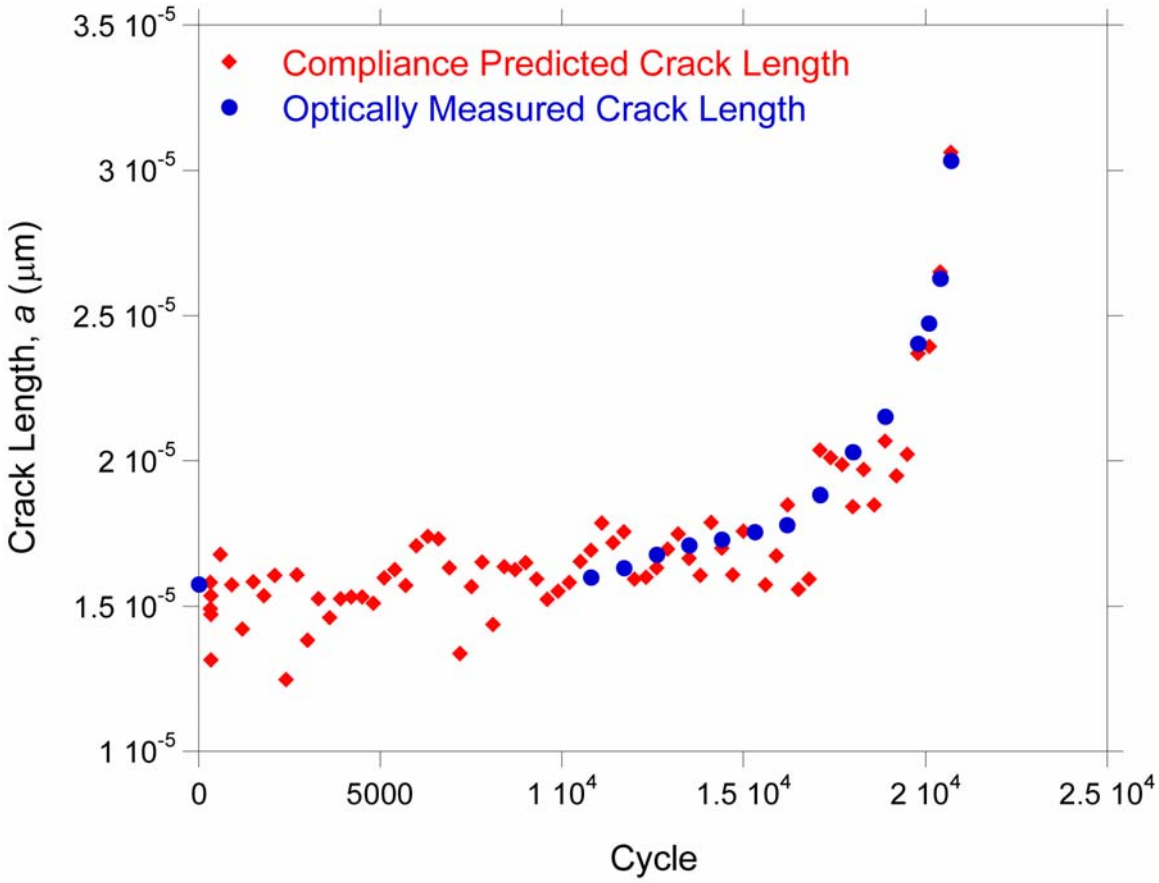

Figure **2-15**: Plot of compliance-based predicted crack length (red) as a function of cycle, plotted along the optically measured crack length (blue) as a function of cycle. This plot shows that the compliance based predictions of crack length match well with the measured lengths, but show significant scatter.

2.3.2.2 Stress Intensity Factor Calculation

Stress intensity factor, a measure of the driving force of crack advance was found using Equation **5**:

$$\Delta K = \Delta\sigma \cdot \sqrt{\pi \cdot a} \cdot f\left(a/b\right) \qquad \mathbf{5}$$

where a = crack length (initially ½ notch width), b = ½ gage width, $\Delta\sigma = \sigma_{max} - \sigma_{min}$ as determined from load cell forces and $f\left(a/b\right)$ was found using Equation **6,** a solution provided by Tada et al [60].

$$f\left(a/b\right) = \left\{1 - 0.025\left(a/b\right)^2 + 0.06\left(a/b\right)^4\right\}\sqrt{\sec\left(\frac{\pi \cdot a}{2 \cdot b}\right)} \qquad \mathbf{6}$$

Due to the symmetric crack growth from both ends of the notch (as will be reported in a future section), the stress intensity factors from the two ends of the notch were combined to form an average stress intensity factor.

2.3.2.3 Crack Growth Rate Measurement

Crack growth rates were calculated by dividing the change in the optically measured crack length by the change in cycle (secant method, 3 point, 50% overlap [58]). Due to the noisy and scattered nature of the compliance measurement, compliance based crack lengths predictions exhibited an equally scattered nature. Although these predictions have excellent correlation to the optically measured crack lengths, the scatter hinders the secant method from being used, as negative crack growth rates (‘crack healing’) would be falsely computed.

2.3.2.4 Closure Analysis

It has been shown that mechanisms occurring in the crack wake can influence the driving force for crack propagation and in turn, the rate of crack advance [18, 45]. These closure mechanisms are more dominant at lower ΔK and low load ratios due to the smaller crack opening displacements. Significant crack closure would result in higher stresses generated at the initial crack opening in a cycle – a deviation from linearity having higher slopes at the lowest displacements. Closure analysis was performed for the fourth fatigue test. This analysis was performed by measuring the linearity of the full force vs. displacement curves throughout the test. This linearity measure was taken by plotting force vs. displacement for full cycles throughout the test and fitting the resulting plot with a linear fit (Figure **2-16)**. The R value, a good measure of the correlation of the linear fit was recorded for cycles throughout the test.

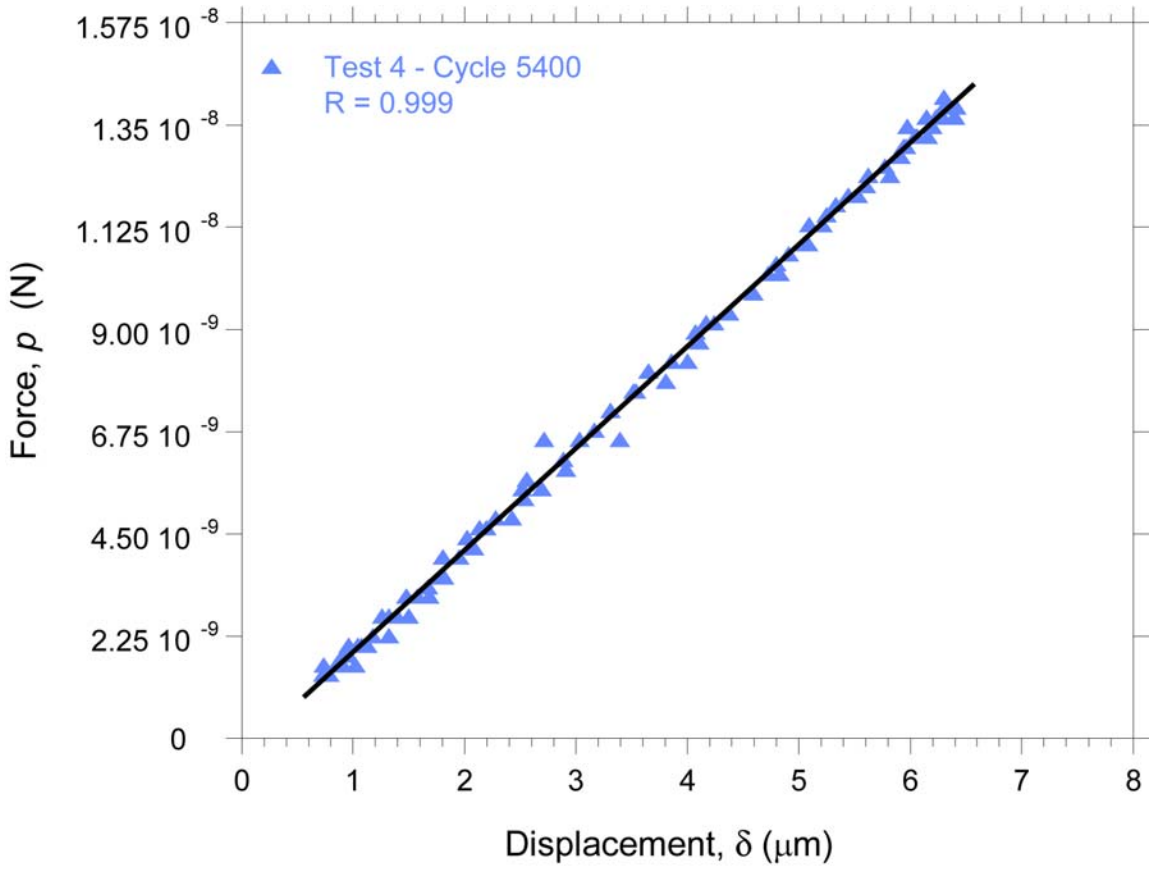

Figure **2-16**: Typical force-displacement curve from fatigue test 4. Slopes and correlation values (R) were recorded for several cycles throughout the test.

2.3.3 Field Emission Scanning Electron Microscopy

After fatigue failure, resulting fracture surfaces were imaged in a field emission scanning electron microscope (FE-SEM). Two versions of the stub holding the fracture surfaces were used; neither mounting technique required alteration of the sample or fracture surfaces for image clarity. Fractography of failed specimens was performed using a JEOL JSM-6700F FE-SEM operating at a range kV (from 5 to 15, depending on best results). The following section will detail the mounting technique used to mount the fatigue fracture samples.

After several unsuccessful mounts of samples, including a fatigue sample from test 1, a sample from test 2 was successfully mounted on a 45 degree inclined aluminum stub and adhered to it with carbon glue. Viewing of the sample was difficult but was achieved via inclining the stub up to 20 degrees further within the instrument (Figure **2-17**). A modified stub was created specifically for the mounting of thin film fracture surfaces on tungsten needles. Holes matching the diameter the needle were drilled into aluminum stubs which were hollowed midway through the stub, allowing needles to be placed vertically into the stub and exposing the fracture surface directly. The underside of the needle protrudes from the hollowed out end, and is further fixed in place by the application of silver paint on the underside, thus keeping the fracture surface far from any glue (Figure **2-18**). A schematic of this stub will be included in Appendix B.

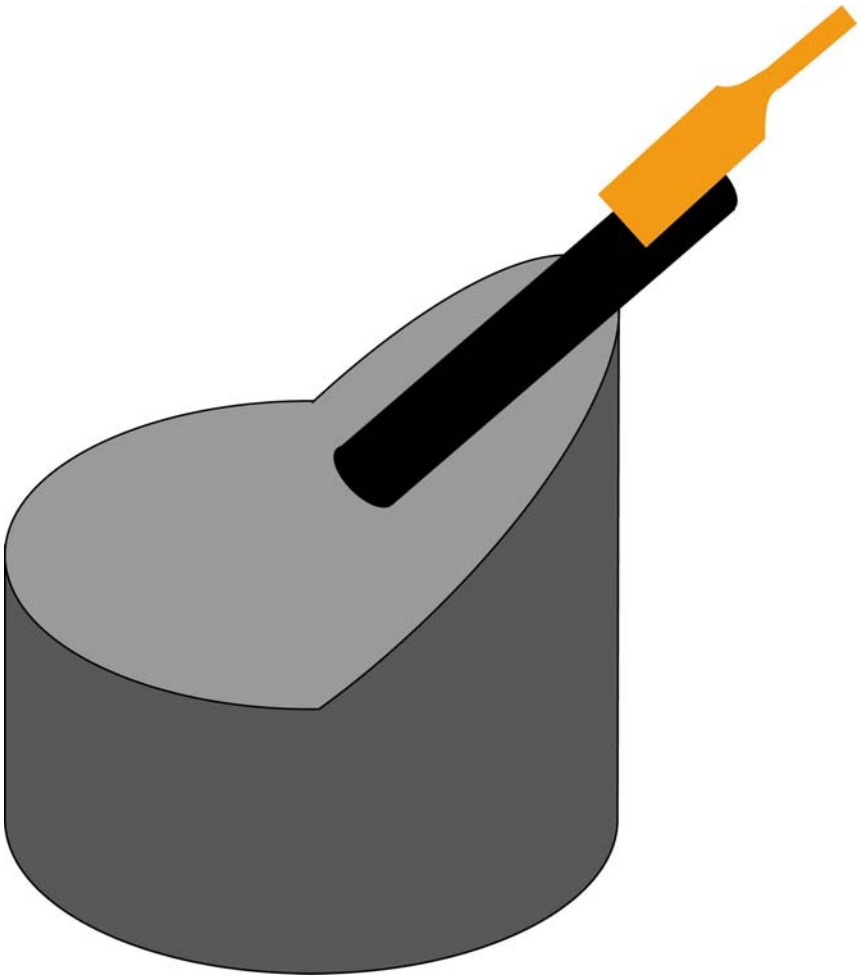

Figure **2-17**: Schematic of the 45 degree inclined stub used to hold a fatigue fracture surface from test 2. Carbon glue was used in the region where the needle (shown in black) met the stub (shown in the light gray).

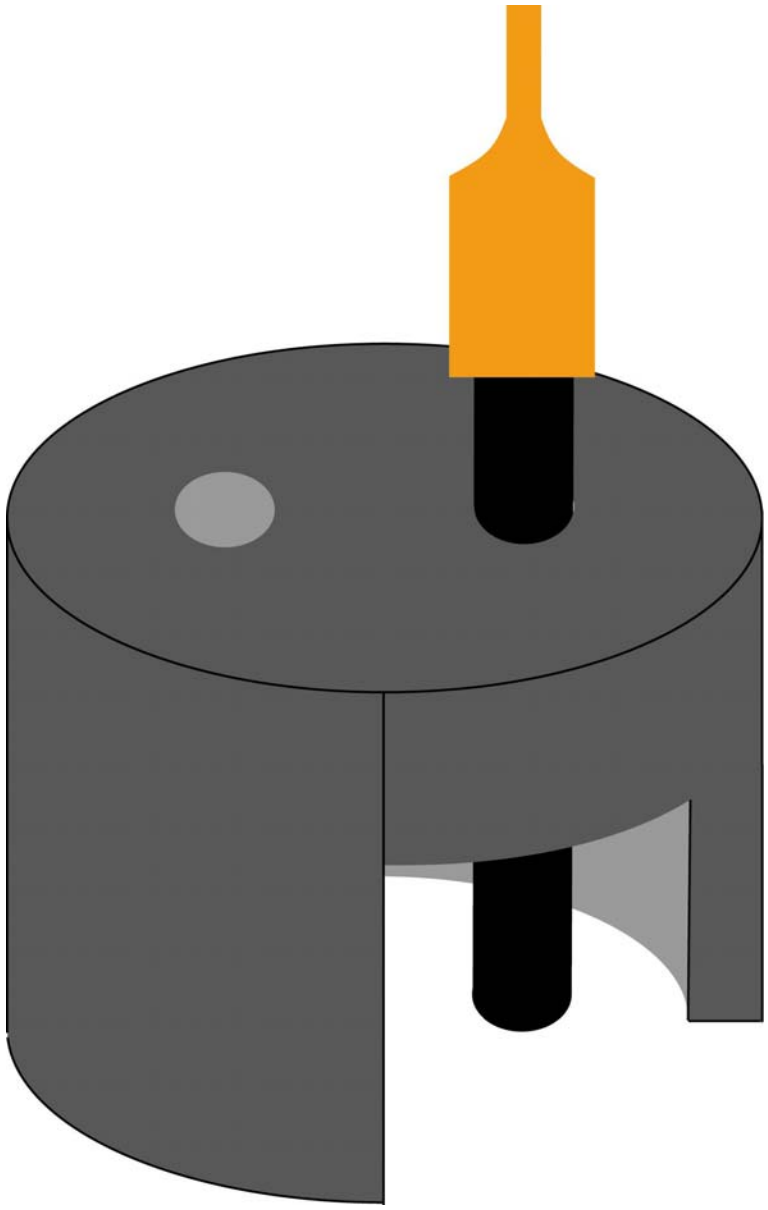

Figure **2-18**: Schematic of the vertical specimen stub specifically designed to hold fatigue fracture surfaces such as those from tests 3 and 4. Silver paint was used where the needle (shown in black) protruded from the underside of the stub (not visible).

Chapter 3

Results and Discussion

This section will open with a detailing of results from the tensile test performed on the platinum sample. Results will show the thin film nanocrystalline platinum has a higher ultimate tensile strength than microcrystalline platinum. The section will transition to reporting about the four fatigue tests performed on the platinum samples. Crack lengths tracked throughout the tests will be reported and discussed. A discussion of crack growth rates will follow. These crack growth rate curves will show that platinum behaves in an unexpected manner, unique from other FCC metals. Mechanical testing results will conclude with a discussion of crack closure for the fatigue tests. At the conclusion of results stemming directly from testing, there will be an analysis of fracture surfaces examined by FE-SEM. Results from this analysis will show that the mechanism which is driving crack growth in the nanocrystalline platinum has led to intergranular failure at low crack velocities, and transitions to transgranular fracture at higher velocities. In order to attempt to explain the results observed in this study, mechanisms will be proposed and discussed. The section will also feature an in-depth discussion of mechanisms for intergranular failure observed and predicted in metals. In addition to the literature findings, a review of the crystallography of slip relating to a (111) oriented FCC metal will follow, noting the likelihood of an alternate hypothesis which explains the apparent intergranular failure.

3.1 Tensile Behavior

This section will discuss the results of the tension test performed on a centrally notched platinum sample. By using the far field stress and the stress concentration factor of the notch, it was possible to calculate the effective stress at the tip of the notch. Results will show that the nanograined platinum films are significantly stronger than microcrystalline platinum. Reasons are also given for the lack of a stress-strain curve typically resulting from a tensile test.

The general yielding of the specimen has been suppressed by concentrating the deformation at the notch roots as indicated by the linearity of the force-displacement response (Figure **3-1)**. Some film buckling is apparent during the test, introducing a slight, but unavoidable error into the test; buckled regions during the test appear flat after fracture, suggesting that this buckling is purely elastic. After some ductile tearing at the notch, fracture occurred via a shear mechanism that proceeded on surfaces inclined to the loading direction at an angle of about 45º (Figure **3-2**).

By using the largest force recorded during the tensile test, and dividing it by the cross-sectional area, the nominal stress was found to be 681.6 MPa. By calculating the stress concentration provided by the notch [59], the maximum stress at the tip of notch was calculated. This value of ultimate tensile strength (UTS) was found to be 3.4 GPa. Because it is likely that some plastic deformation occurred at the crack tip prior to failure, this value represents an upper bound estimate on the UTS. In comparison, nanoindentation of these thin films while still attached to the substrate have found a yield strength of 1.97 GPa [61], and unpublished results of tensile testing of these free standing thin films have found a yield strength of 1.47 GPa [23], although the latter finding is based on the reported thickness of the films (500 nm) whereas our studies have measured this value directly to be (450 nm). In either way, both the experimental yield strengths, and the upper bound value of UTS is significantly larger (more than an order of magnitude) than that of microcrystalline platinum which has a yield strength of 185 MPa and a UTS of 240 MPa [16], confirming trends relating to the Hall-Petch relationship.

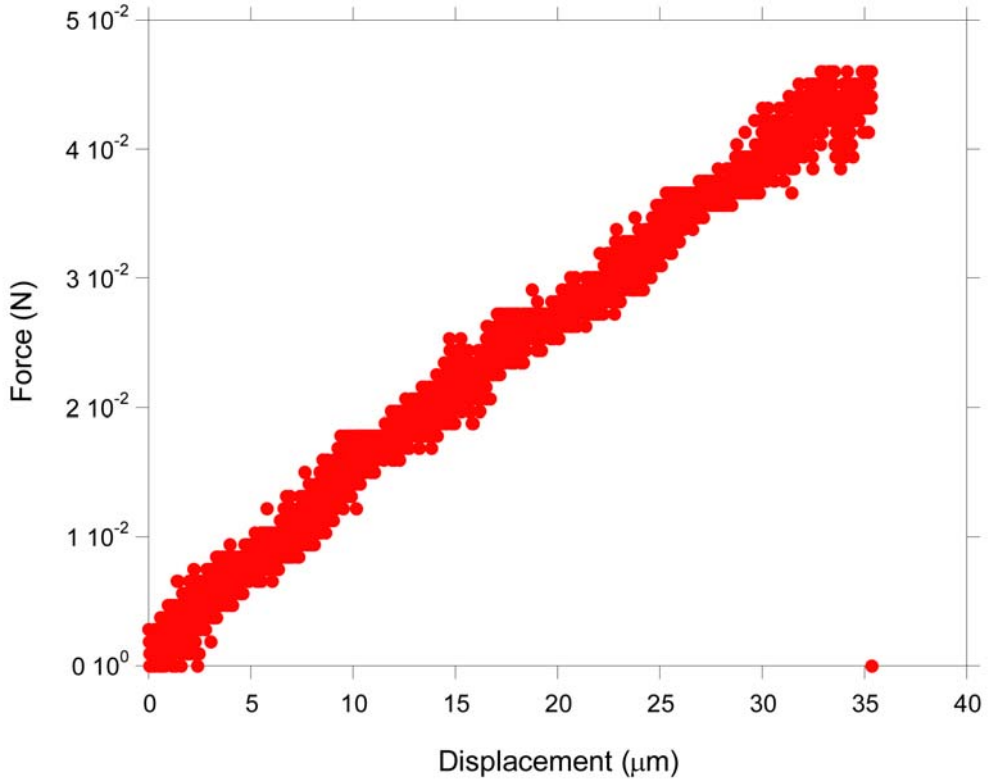

Figure **3-1**: Force-crosshead displacement curve for a uniaxial tensile test conducted on a 150 μm wide, center-notched micromachined platinum specimen (the last point marks specimen failure). The upper bound for the ultimate tensile force of this specimen was calculated to be 3.4 GPa once the stress concentration factor of the notch was taken into account.

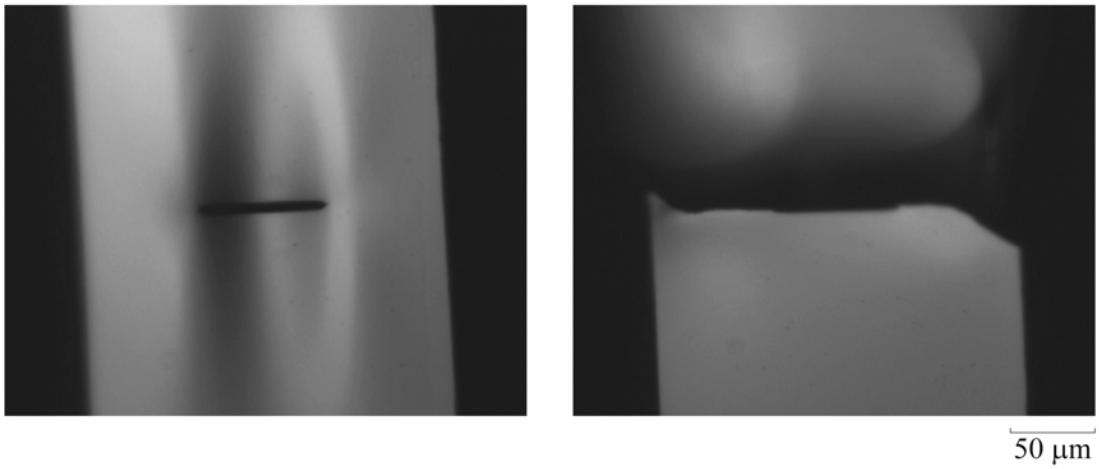

Figure **3-2**: Optical micrographs of a notched tensile specimen of Pt during testing (left) and immediately after failure (right). After some ductile tearing at the notch (flat portions on either side of the notch), fracture occurred via a shear mechanism that proceeded on surfaces inclined to the loading direction (45º slanted portions on either end of the flat portions).

3.2 Fatigue Crack Length as a Function of Fatigue Cycle

This section will discuss crack extension during fatigue cycling of the platinum films. Cracks extended symmetrically from the central notch and propagated at similar growth rates. Due to the crack symmetry, average crack length, averaging crack length from both ends of the notch, is reported for two tests in which the initial notch spanned the same percent of the sample width but where stress amplitude was measurably different.

During the fatigue crack growth tests, cracks grew symmetrically from the notches and exhibited straight (i.e., nominally mode I) crack paths, and surface distortions associated with the development of the plastic zone were not observed. Final rupture of the specimens occurred on paths that were inclined 45° from the tensile loading axis after an unknown amount of stable, ductile tearing. (Figure **3-3**). The symmetry of the crack extension from both ends allows for reasonable averaging of the two crack lengths. (Figure **3-4**) This symmetric growth is also a testament to the uniaxial conditions of the testing setup, as well as the overall uniform material properties of the nanocrystalline platinum.

Stress amplitude, initial average crack length, final average crack length, and sample lifetime results are summarized in Table **3-1**. Stress amplitude varied between 300 MPa and 332 MPa, all above the ultimate tensile strength of microcrystalline platinum, but ranging roughly between 9 and 10% of the ultimate tensile strength of nanocrystalline platinum (3.4 GPa) as was found in the previously described tensile test. Average initial crack sizes were all 33% of the gauge width, and ranged 51% to 63% of the gauge width just prior to failure. Final recorded lifetimes of samples ranged between 700 and 9900 cycles, although there may have been some final crack growth between the final recorded cycle and the actual cycle associated with failure (as not every cycle was recorded). It is apparent that an increase in initial stress intensity produces a decrease in overall lifetime as would be expected, and indicates that the testing methodology is

consistent and repeatable. Figure **3-5** shows the average crack length to specimen width ratio as a function of cycle of all four platinum fatigue tests.

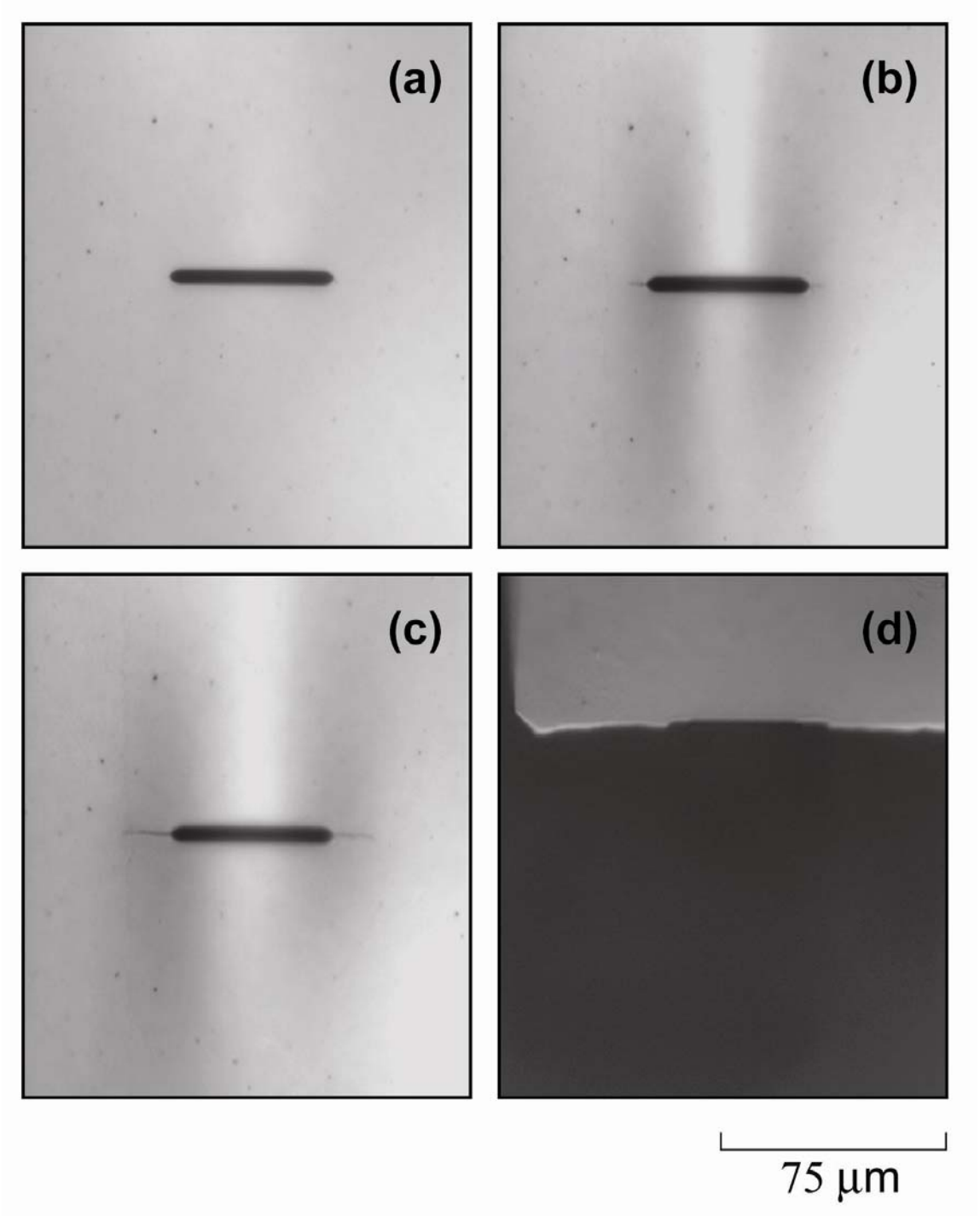

Figure **3-3**: Optical images acquired during fatigue testing of a nanocrystalline Pt film (test 3) showing (a) the initial slot, (b) a crack at 50% of the critical crack size, (c) a crack at 75% of the critical crack size, (d) the sample after fracture.

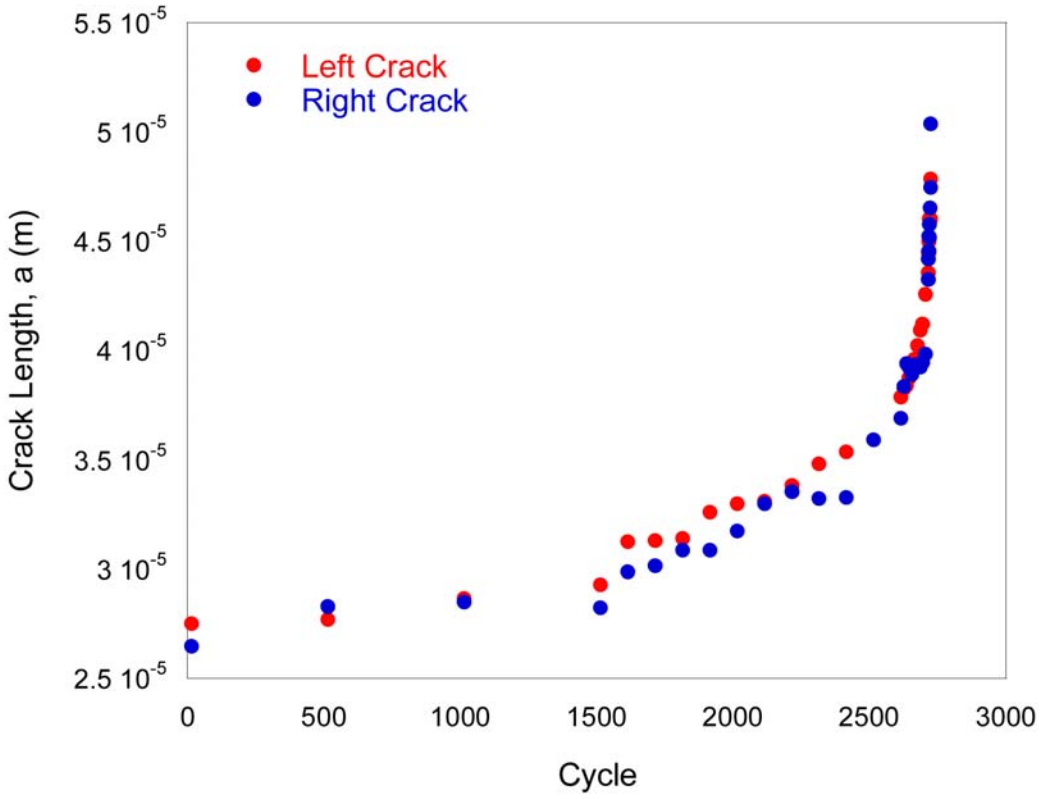

Figure **3-4**: Crack Length (as measured optically) as a function of cycle in fatigue test 2 showing that cracks from both ends of the notch grew at similar rates.

Table **3-1**: Summary of crack growth results of the 4 platinum fatigue tests

	Stress Amplitude, $\Delta\sigma$ (MPa)	Initial Average Crack Length, a (μm)	Final Average Crack Length, a (μm)	Final Crack Length to Gauge Width Ratio	Sample Lifetime (cycles)
Test 1	330	33.6	50.9	0.51:1	700
Test 2	300	27.0	49.1	0.61:1	2723
Test 3	332	26.2	47.6	0.61:1	790
Test 4	311	16.0	30.3	0.63:1	9900

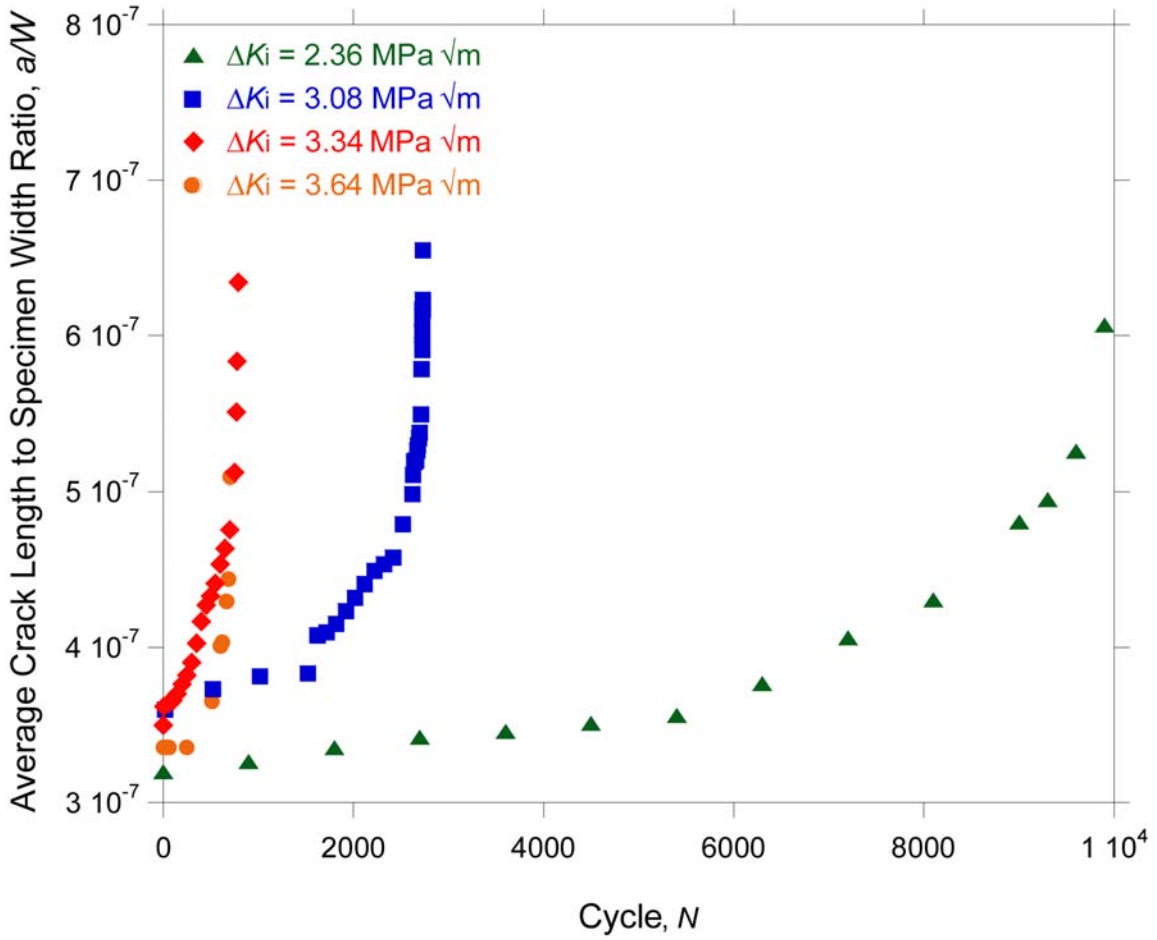

Figure **3-5**: Average crack length to specimen width ratio as a function of cycle in all four platinum fatigue tests. Note the correlation between a lower initial stress intensity (ΔK_i) and longer fatigue lifetime.

3.3 Average Crack Growth Rate as a Function of Average Stress Intensity Factor Range

This section will discuss the crack growth rates of the platinum films resulting from cyclic fatigue. The crack growth rate curve plotted against the stress intensity factor will be shown for each individual test. Their close agreement to each other allows the data from all 4 tests to be plotted at once; all 4 tests will be shown together and plotted beside the data for microcrystalline platinum tested in air [55]. The results will show the significant difference between the nanocrystalline and the microcrystalline platinum.

The measured fatigue crack growth rates as a function of the applied stress intensity factor ranges are shown in Figure **3-6**. An extremely limited range of stable fatigue crack growth was observed (~2.5 MPa √m), and a least squares curve fit of the data to a power law relationship between the fatigue crack growth rate da/dN and the applied stress intensity factor range, ΔK, (i.e., $da/dN = C(\Delta K)^m$) provided a large power law exponent, m, with values ranging between 7.9 and 15.3. The fracture toughness, K_q, estimated from K_{max} just prior to fracture ranged from 4.45 MPa √m to 4.88 MPa √m for the first 3 tested samples, and was 3.45 MPa √m on the fourth test. It is likely that there was a significant amount of additional stable crack growth after the last recorded data point and prior to failure in the fourth fatigue test; this growth was not captured due to the fact that data as recorded less often to minimize data volume during longer fatigue tests. Stress amplitude, scaling constants, power law exponents and fracture toughness are summarized in Table **3-2**.

In contrast to microcrystalline metals, the nanograined Pt films in this investigation exhibited fatigue crack growth rate trends that were reminiscent of extrinsically toughened structural ceramics and ordered intermetallics (i.e., $m > 10$). Consistent with this observation, the fracture toughness of the nanograined Pt film was exceptionally low – ~10 times less than the micrograined form of the material,

(Figure **3-7)**. The following section will examine fatigue fracture surfaces and relate the crack growth rates to fracture features and mechanisms.

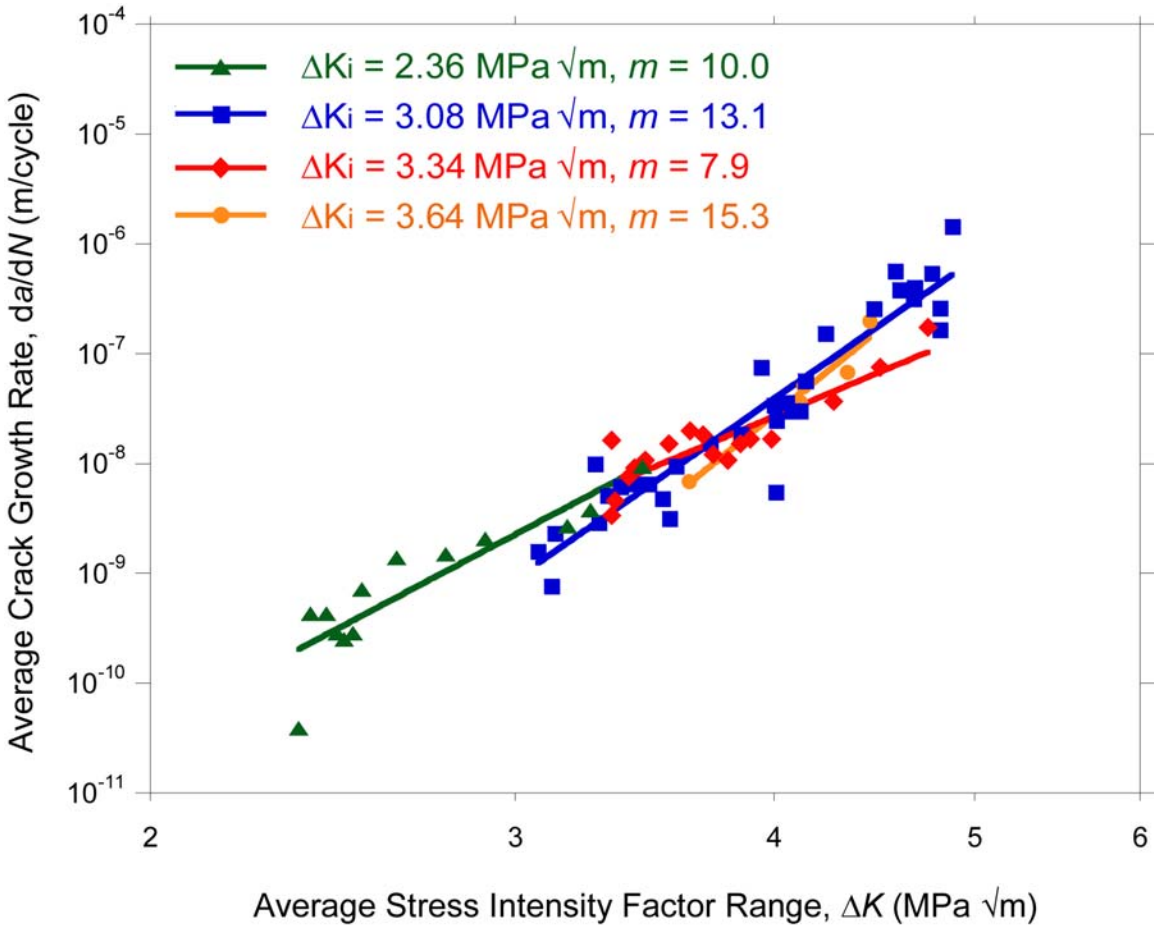

Figure **3-6**: Empirically measured fatigue crack growth behavior of nanograined platinum films. Four tests are plotted individually and noted by their initial stress intensities (ΔK_i). The power law fit of the nanograined Pt indicates a high power law exponent (m ranging from ~8 to ~15).

Table **3-2**: Summary of crack growth rate results of the 4 platinum fatigue tests

	Stress Amplitude, $\Delta\sigma$ (MPa)	Scaling Constant, C	Power Law Exponent, m	Fracture Toughness, K_q, (MPa $\sqrt{m}$)
Test 1	330	1.80×10^{-17}	15.3	4.45
Test 2	300	4.77×10^{-16}	13.1	4.88
Test 3	332	4.59×10^{-13}	7.9	4.75
Test 4	311	3.83×10^{-14}	10.0	3.45

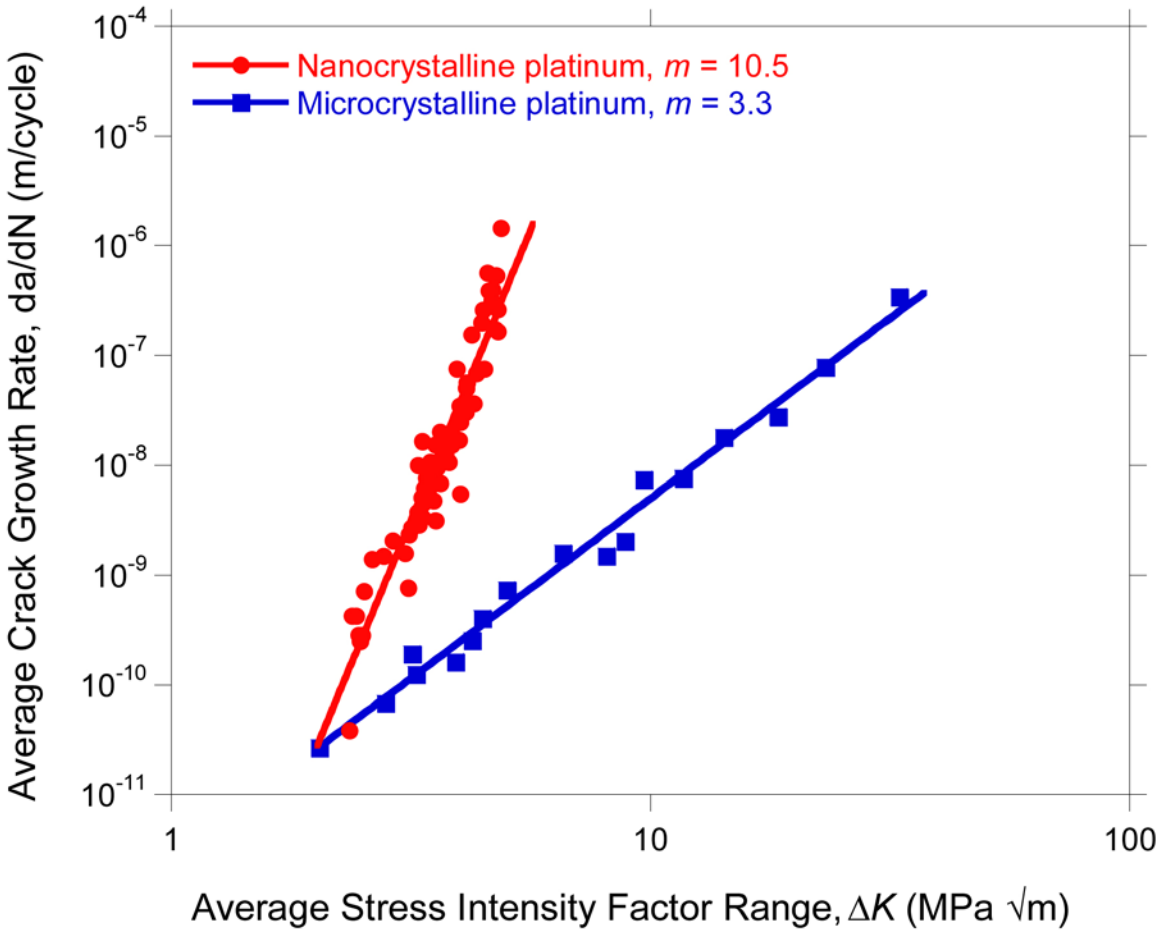

Figure **3-7**: Empirically measured fatigue crack growth behavior of nanograined Pt films (red circles) compared to a power law fit of previously published data for micrograined Pt by Speidel (blue circles) [55]. The power law fit of the nanograined Pt (solid line) indicates a high power law exponent (m = 10.5) when compared to the microcrystalline Pt behavior (m = 3.3). The absence of a conventional, sigmoidally-shaped fatigue crack growth curve is readily apparent in the nanograined Pt data.

3.4 Crack Closure Analysis

Materials such as ceramics or ordered intermetallics having high crack growth exponents such as those reported in the previous section typically show some degree of extrinsically induced crack closure. Crack closure is a toughening mechanism which acts in the wake of the growing cracks and acts to shield the crack tip from the far-field driving forces [45]. There are several mechanisms which contribute to crack closure, such as (but not limited to) 'wedging' (debris or surface roughness induced closure) and 'bridging' (ligament or fiber induced closure). As crack closure serves to shield the crack tip at the lowest displacements, a non linearity is typically noticeable at those displacements (Figure **3-8**). This closure is typically more dominant at low ΔK and lower load ratios due to the smaller crack opening displacements (and thus increased interaction of the two crack wake fronts). The overlap of the closure process zone and the crack wake grows larger as the crack grows (until stable state is reached when 100% of the process zone overlaps the crack wake) and so closure effects typically become more noticeable as the fatigue crack length increases. These effects can be observed by plotting and comparing the force-displacement curves throughout a fatigue test. The effects of crack closure on the fatigue crack growth rates are notoriously difficult to quantify due to the small fluctuations in microstructure along the path of the crack, and the dependence of crack closure on testing conditions (load ratio, environment etc.) [45]. The descriptions of the fatigue crack growth behavior in the previous sections relate the fatigue behavior of nanocrystalline platinum to the behavior of brittle ceramics which typically exhibit some crack closure effects. In order to examine this behavior further, an attempt was made to quantify the extent of crack closure in the nanocrystalline platinum thin films.

Data from the last fatigue test in which full force-displacement curves were available were analyzed for crack closure effects. Force-displacement data for cycles at various stages of the fatigue test were plotted. There was no apparent change in linearity in the compliance curves during a single cycle, and this linearity did not vary as the cracks extended throughout the course of the test (Figure **3-9**). The linear compliance

curve, measured for a relatively low load ratio of 0.1 would be indicative of a lack of crack closure effects in nanocrystalline platinum.

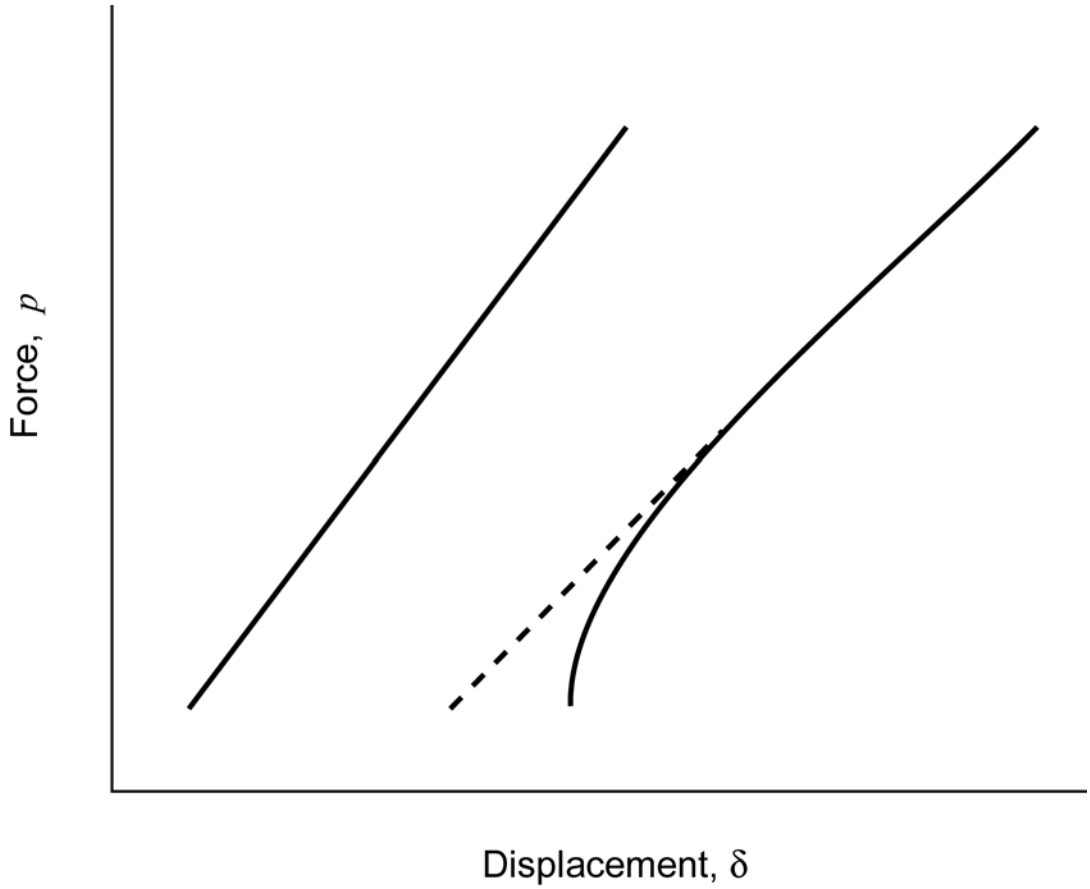

Figure **3-8**: A schematic of typical crack closure effects on force as a function of displacement plot. The relationship shown at the left is of an early cycle in a fatigue test where there has not been significant crack growth; the linearity is indicative of no significant amount of crack closure effects. A later cycle within the same fatigue test is shown at the right; notice the shift in data and a reduction in slope as a result of the increasing compliance of the specimen as the cracks advance, but also note the non linearity at the low crack opening displacement, indicative of crack closure effects.

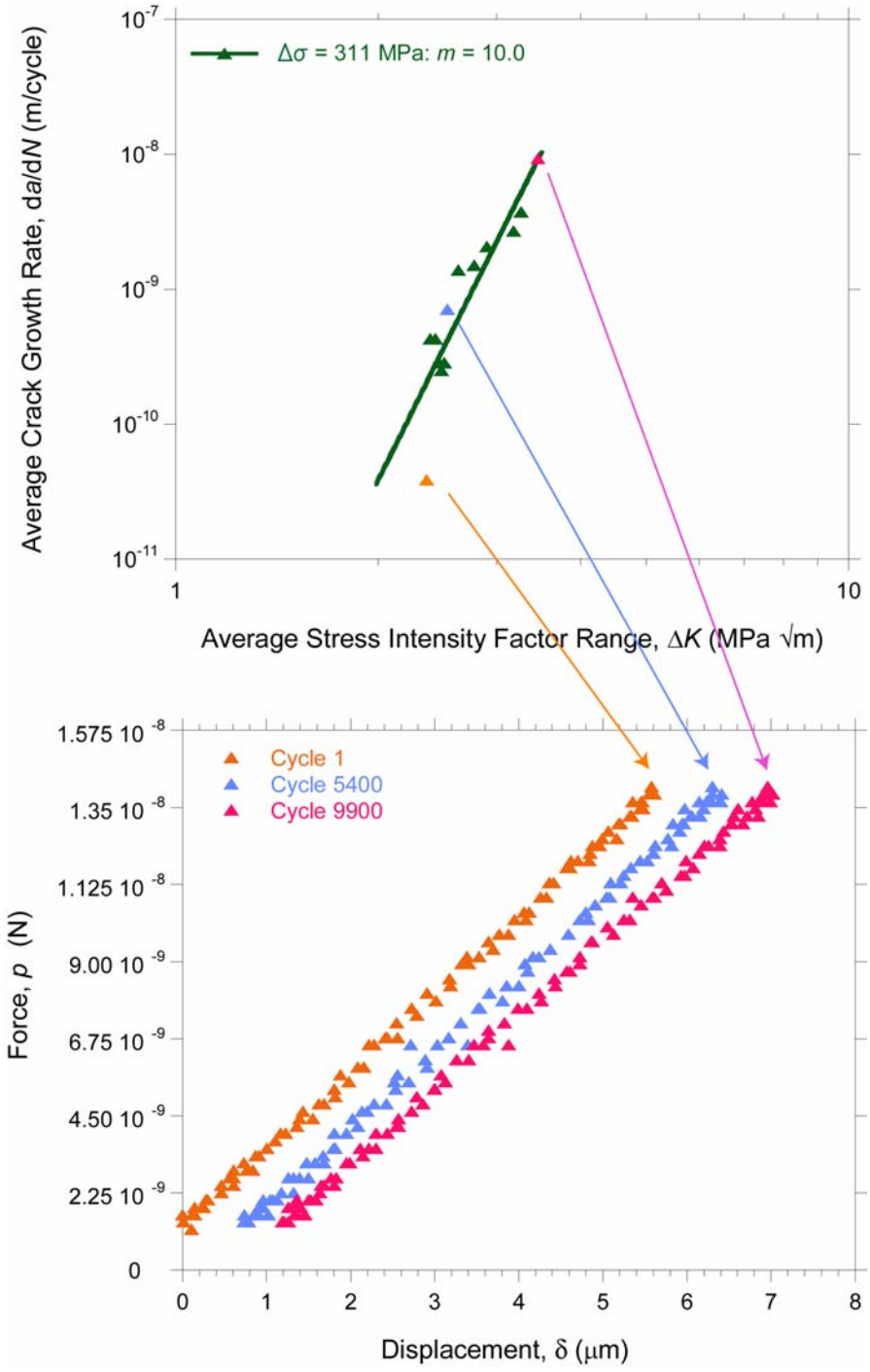

Figure **3-9**: Crack closure analysis comparing early, mid, and late cycles in fatigue test 4. No significant change in linearity can be seen. The shift in the data is due to a change in compliance as a result of crack growth.

3.5 Field Emission Scanning Electron Microscopy Analysis

This section will discuss results from microscopy work performed on the fracture surface. Fatigue fracture surfaces of the nanocrystalline platinum samples were mounted on a custom modified stub so as to allow the analysis of failed thin film specimens. Fracture surfaces were examined using a field emission scanning electron microscope (FE-SEM) to image the crack path. Microscopy of the failure surfaces of the revealed that the cracks in the nanograined platinum initially followed an intergranular path and transitioned to a transgranular path at higher crack growth rates.

The fatigue crack path occurring in areas nearest the notch and analogous to the near-threshold regime (i.e., growth rates below 10^{-9} m/cycle) and up to ~2×10^{-7} m/cycle was intergranular (Figure **3-10**). Images from this region reveal visible grains and secondary cracking. As the cracks grew in length and accelerated to ~3×10^{-7} m/cycle, they gradually transitioned to a transgranular path. During this transition, a fine ridge associated with localized transverse necking of the material developed in the center of the failure surfaces, parallel to the crack propagation direction. This relatively short section (Figure **3-11**) exhibited both visible grains associated with an intergranular crack path, as well the plastic sheer lip associated with a transgranular crack path. The transgranular mode dominated the crack path at growth rates larger than 4×10^{-7} m/cycle (Figure **3-12**). This crack path, most visibly designated by a central ridge associated with plastic deformation, persisted until final fracture occurred at K_{max} ~5 MPa √m. The fatigue crack growth rates of all 4 tests are correlated to the fracture surface in Figure **3-13**, and the three portions of the fracture surface are shown collectively in Figure **3-14**; the color scheme is consistent between the two aforementioned figures.

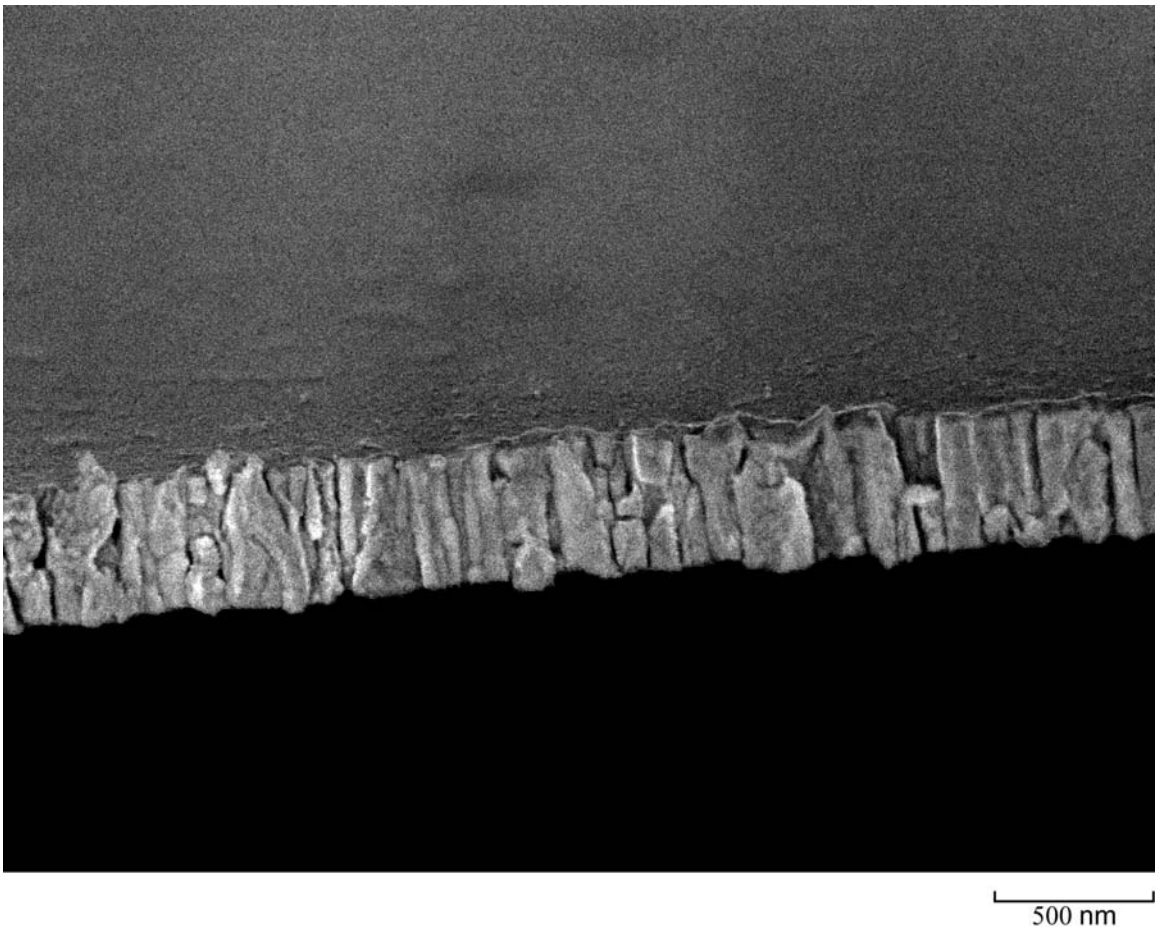

Figure **3-10**: Intergranular failure in an area roughly 3 μm from the notch. This crack path is characterized by visible columnar grains and microcracking. This image is representative of the early portions of crack growth. Taken from Test 3 (ΔK = 3.02 MPa $\sqrt{}$m, $da/dN = 7.62\times10^{-9}$)

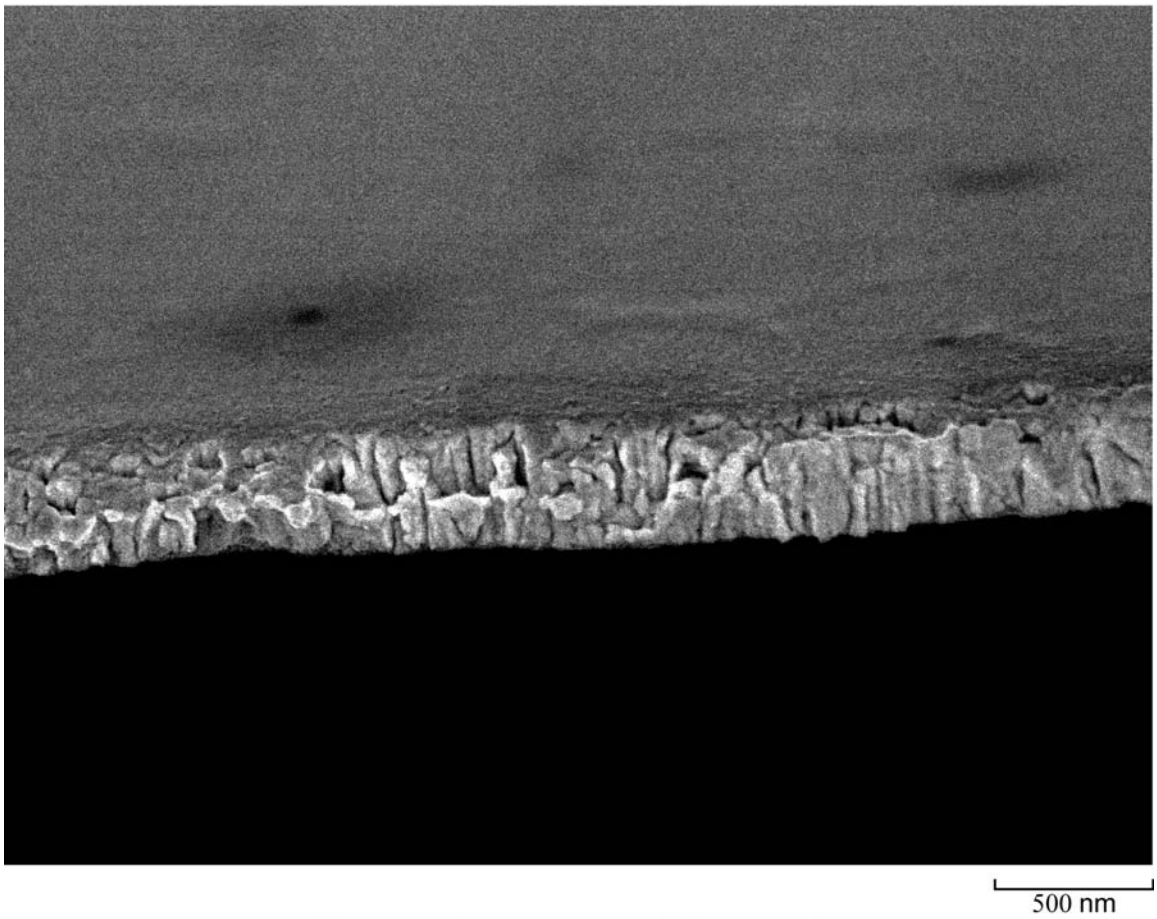

Figure **3-11**: Transitional cracking behavior in an area roughly 17 μm from the notch. This crack path is characterized by a gradual transition from an intergranular crack path to a transgranular one. Taken from Test 3 (ΔK = 4.05 MPa $\sqrt{m}$, $da/dN = 1.78\times10^{-7}$)

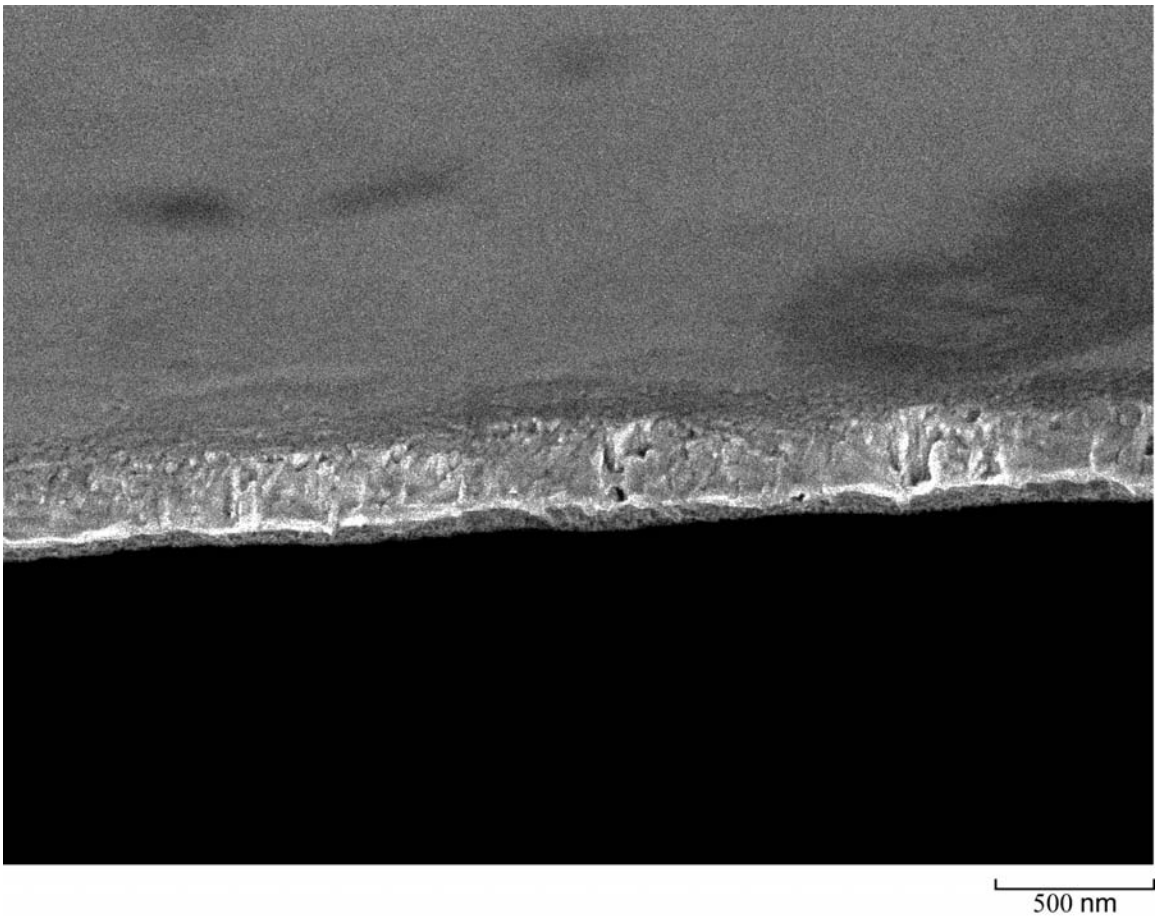

Figure **3-12**: Transgranular failure in an area roughly 21 μm from the notch. This crack path is characterized by a lack of apparent grain structure and a plastic sheer lip running across the center of the fracture path. This image is representative of the later portions of crack growth. Taken from Test 3 (ΔK = 4.27 MPa $\sqrt{m}$, $da/dN = 3.13\times10^{-7}$)

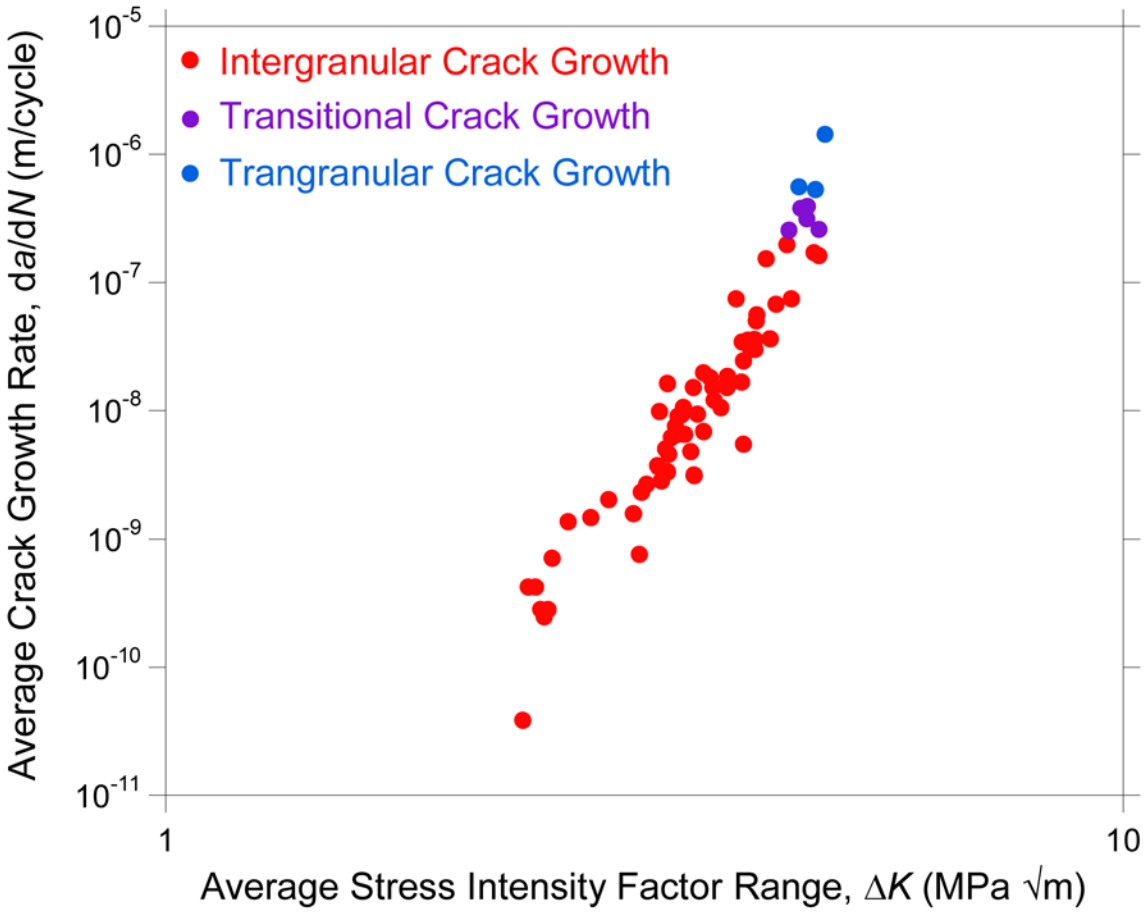

Figure **3-13**: Crack growth rate curves highlighting crack advance mechanisms: intergranular advance (red), transitional advance (purple), and transgranular advance (blue).

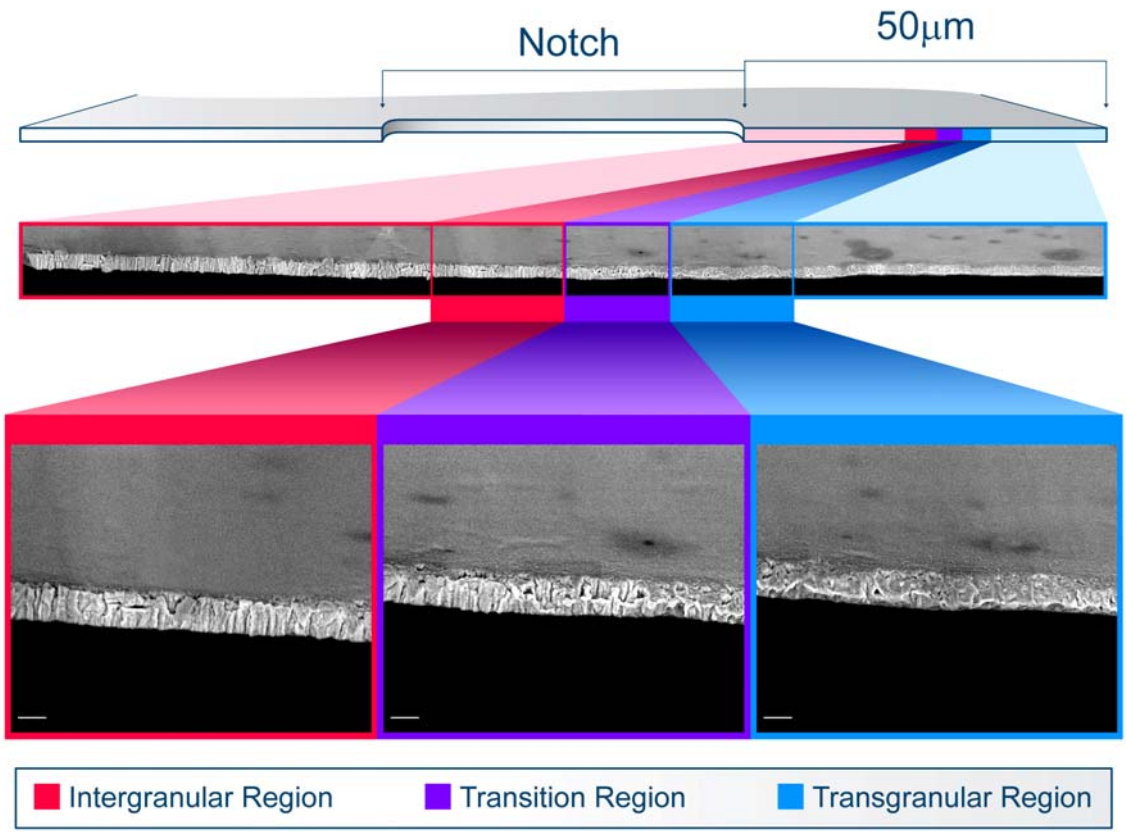

Figure **3-14**: Scanning electron micrographs of a typical Pt film fatigue failure surface in relation to the original sample. As the crack advanced from left to right, the crack propagated via an intergranular path (red). As the fatigue crack growth rate reached ~2×10^{-7} m/cycle, the growth mode transitioned to a mixed inter- and transgranular morphology (purple). Above ~3×10^{-7} m/cycle, the crack path was transgranular (blue) with a central ridge that was associated with localized necking. The scale bar in the images corresponds to 300 nm.

3.6 Proposed Mechanisms

Intergranular failure modes in face-centered cubic (FCC) metals are usually associated with boundaries that have been weakened by the presence of a secondary phase or atomic species [62], "active" (i.e., corrosive) service environments [63], or gross structural defects such as cracks and voids [34]. Extensive analysis by EDS, EELS and SIMS has revealed secondary phases at or below detection limits of the instruments, which means they are an unlikely cause of the unusual crack mechanism. No gross quantity of cracks or voids was detected by TEM. The high tensile strength confirms the film is strong. The transition from an intergranular crack path to a transgranular one indicated that the mechanism may be velocity dependant and not resulting of an impure or defective film.

3.6.1 Intergranular Failure in Literature

In order to better understand the mechanisms giving rise to intergranular cracking, an overview of reports of intergranular failure in metals, across all length scales, is presented in this section. The proposition that face centered cubic metals may fracture intergranularly is not foreign to the literature, but experimental accounts are few, and mechanistic explanations conflict with each other and with modeling work. Several investigations found evidence of intergranular cracking resulting from cyclic fatigue of polycrystalline copper [64-67]. These investigations cited the source of this intergranular cracking was a result of void coalescence at grain boundary and persistent slip band (PSB) junctions, citing that the theoretical shear stresses necessary to create voids at grain boundary and PSB junctions in polycrystalline copper are less than the real sheer stresses operating within a PSB. However, these studies also found that a reduction of grain size functioned to stifle this intergranular cracking. An additional investigation of the mechanism operating at the interaction of PSB with a grain boundary complemented their fatigue testing polycrystalline copper with a numerical model after closely studying the cracking under a scanning electron microscope [68]. By calculating the degree of

misorientation of grain boundaries, Liu et al showed that grain boundaries having the highest misorientations were the most susceptible to intergranular cracking due to the impingement of PSBs against the grain boundaries. Their model estimated that the minimum theoretical shear stress which is required to act in the PSBs for causing intergranular cracks were always smaller than the real shear stresses operating within a PSB. Like other models, this model failed to explain why not all PSB-grain boundary regions formed intergranular cracks. A later investigation on the same material system concluded that the intergranular cracking was a result of environmental reasons, citing no such cracking when this oxidation was limited by cathodic polarization [69]. These reports of intergranular failure in a microcrystalline metal are confined to copper, and have been shown to be a cause of environmental reasons. These findings are unlikely to relate to the mechanisms operating in nanocrystalline platinum due to the significant difference in grain size, and platinum's natural resistance to oxidation.

The experimental reports of intergranular cracks are limited to grain sizes in the micrometer range. Several experimental investigations on nanocrystalline and ultra-fine grain metallic system which did not directly report intergranular cracking have cited the possibility of grain boundary dominated plastic deformation for their unexpected results. Deviations from expected behavior in nickel [29], in gold [42], in aluminum and palladium [70], and copper and nickel [71] have all been attributed to a change in plastic deformation mechanism due to an increase in grain boundary dominated mechanisms such as grain boundary reorientation, sliding and creep. The investigation reported on this thesis would go to suggest that these models may be partially correct. In testing free standing nanocrystalline platinum samples, a plastic deformation mechanism which appears to be grain boundary dominated spans a large portion of the stable fatigue crack growth. However, in our study, this mechanism changes as the crack growth rate increases to become a grain interior dominated deformation mechanism, a transition which no experimental work has shown and no modeling work has predicted.

3.6.2 Crystallography of Slip

An alternate hypothesis which states that the fracture surfaces produced are in fact not intergranular, and rather faceted surfaces produced by typical crystallographic slip will be explored in this section. The most common mode of plastic deformation in metals is by the process of dislocation slip. Dislocation slip is the process whereby a dislocation will move through the material as a result of the gliding of close packed planes over one another. In face centered cubic (FCC) metals such as platinum, the close packed plane is the (111) plane; it has the greatest quanitity of atoms per unit area. Slip generally proceeds along the close packed direction within a close packed plane, in the case of the (111) plane, the [110] direction is the close packed direction [72]. Dislocations may slip from one close packed direction to another wthin the same plane; the [110] direction within a (111) plane are 60º rotated from one another, suggesting that within a plane, facets of up to ±60º (exactly) can be created as dislocations pass across the grain. The slip deformation process is hindered by obstacles in the lattice such as grain boundaries, necessitating a change in the direction of crack growth to an alternate close packed plane or close packed direction. The close packed planes in a textured film such as the platinum films used in this study suggests that (111) planes in different grains are parallel, however, the close packed directions within them are not necessarily parallel, and due to the three-fold roatational symmetry of the plane, may be as much as 30º off from one another (Figure **3-15**). This crack advance method suggests that the crack path will be serrated, having teeth-like features across the fracture surface.

This explanation for crack advance is consistent with the fracture portions tied to low crack growth rates. This mechanism assumes that the slip direction will change across grain boundaries in order to maintain the direction requiring the least amount of energy for slip, however, nearer the end of the test, more energy is available per area (as a result of a reduced area ahead of the crack tip), and maintaining this mode of cracking may not be necessary; dislocations may have enough energy to slip in multiple directions, eliminating the faceted features of the crack path. This explanation is also consistent with

the lack of facets towards the end of the testing, when crack growth rates are highest. Although this theory explains the features seen when viewing the fracture path with no tilt angle, additional information becomes available when viewing a fracture surface with tilt. Viewing the sample at angle allows for easier interpretation of the angles associated with the fracture as this viewing mode allows the three-dimensional nature of the fracture surface to be seen (Figure **3-16)**.

Figure **3-17** shows the fracture path of a fatigued platinum sample (test 2). Using this angled view, it is apparent that some features cannot be explained strictly using the crystallographic slip explanation. Some facets are angled, almost circular, and other are much sharper than the predicted maximum of 15º, suggesting that the fracture path is more likely to be intergranular. In order to conclusively differentiate between these two mechanisms, a new set of experiments and analysis is proposed in the following section.

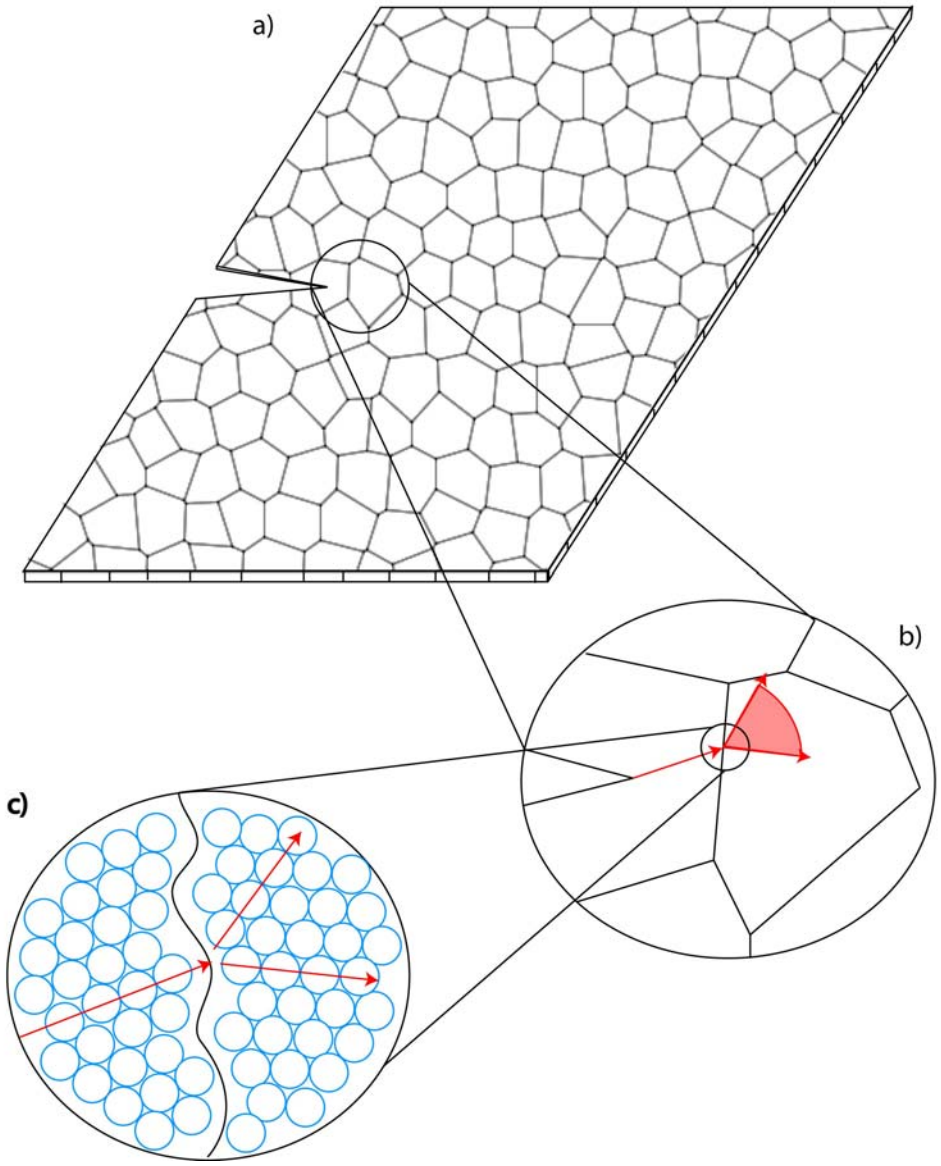

Figure **3-15**: A schematic of the microstructure within a columnar, (111) oriented film. The schematic in section a) shows the grain distribution within the polycrystalline film (not drawn to scale). The schematic in section b) is a close-up of the microstructure near the tip of an advancing crack and shows that the crack may deflect as much as 30º one way or another when crossing the grain boundary. The schematic in section c) is a close up of a grain boundary showing atomic distribution within an FCC lattice; this schematic highlights the maximum 30º misalignment of the [110] direction within the (111) plane that can occur across grain boundaries.

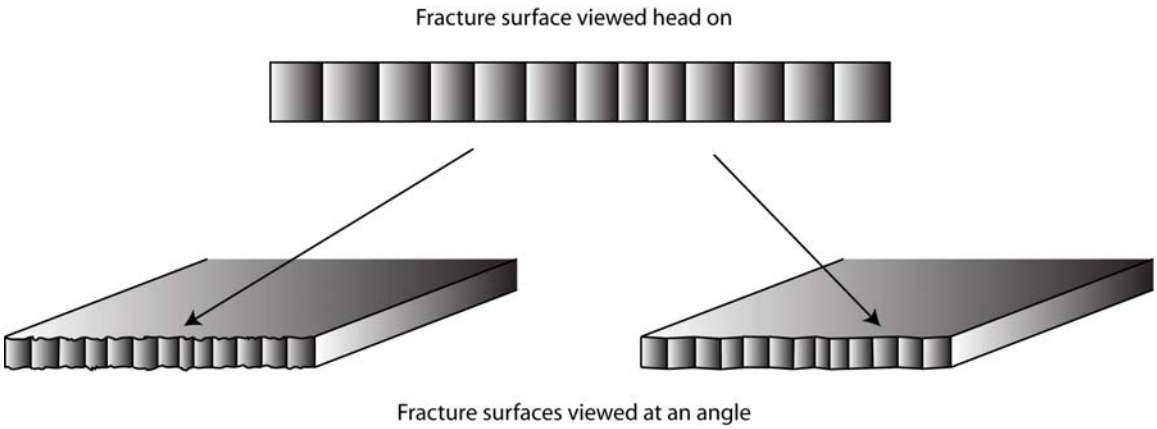

Figure **3-16**: Above, the fracture surface is shown as typically imaged – with no tilt; it is impossible to tell what angles are associated with the fracture surfaces. At the angled views beneath it, surfaces associated with the fracture can be seen. At the bottom left, fracture appears to have left jagged and convoluted surfaces behind it, suggesting it followed grain boundaries. At the bottom right, the surfaces are faceted and all angles are less than or equal to 30º, suggesting that crystallographic slip was the failure mechanism.

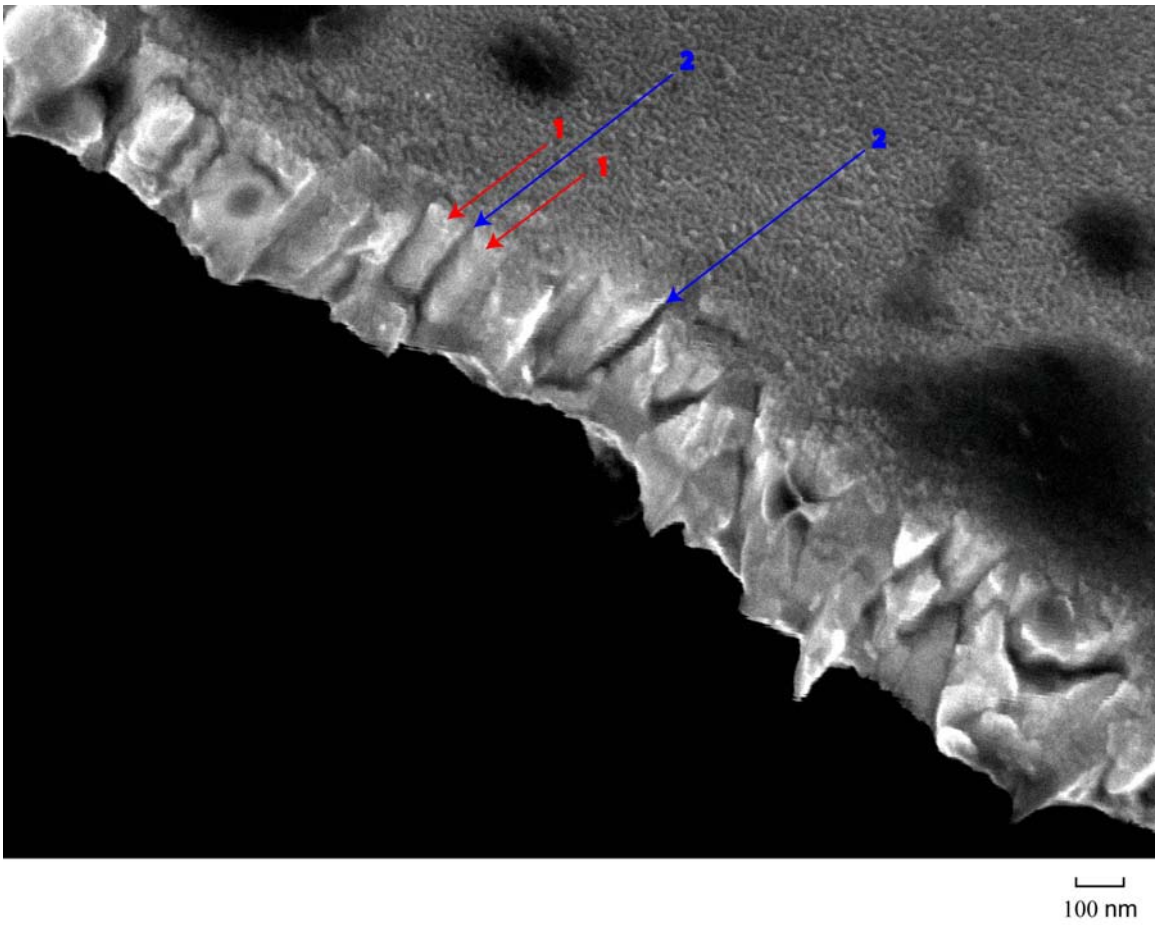

Figure **3-17**: An FE-SEM image showing features that are unlikely to be explained by typical crystallographic slip. The features marked "1" point to rounded features in the fracture surface, and those marked by "2" point to facets having larger than 60º offsets. These features would be harder to detect when not viewing the fracture surface at such an acute angle (typical fracture surfaces are observed 'head on', at a 0º angle offset).

3.6.3 Proposed Mechanism

The fracture surfaces of fatigued nanocrystalline platinum thin films have three distinct regions. The first region, closest to the starting notch, where crack growth is slowest, has a periodicity roughly correlated to the average grain size (25 – 40 nm). These periodic features closely resemble the faces of exposed columnar grains which comprise the sample, and as such, it was concluded in this study that the fracture path is intergranular. An alternative hypothesis was considered, relating these features to ones which would be produced by typical grain-interior crystallographic slip, but this consideration did not map with all features seen on the fracture surfaces (i.e. angles greater than 60º, rounded facets). Despite this, there was insufficient data to completely rule out this explanation. However, by implementing new methods in future tests, it may be possible to settle this dispute definitively. By using TEM on cracks which have not led to fracture, one could observe conditions at the crack tip and at the crack wake. Doing so will require thinning the samples down to electron transparency, without disturbing the crack tip or alternatively, testing electron transparent versions of the nanocrystalline platinum thin films. TEM observations of cracks below their critical lengths would allow for the characterization of the zone ahead of the crack tip (investigating dislocations and voiding for example), and would also allow for the investigation of grains structure in the crack wake (distinguishing between an intergranular and transgranular mode despite a similar crack path) by characterizing the diffraction patterns of grains across the crack path (Figure **3-18**).The second region of the crack path is transitional, marking a partial changeover to a secondary deformation mechanism. The transtion region is characterized by features of both the first and third region. The third region is a region of marked transgranular cracking having a central sheer lip. In this last region, there are no exposed grains, leaving no doubt that mode of cracking is dominated by processes which are grain interior. This change in mechasnism, between a grain boundary dominated process to a grain interior dominated process has not been observed in nanocrystalline metals, and has not been explained by modeling work.

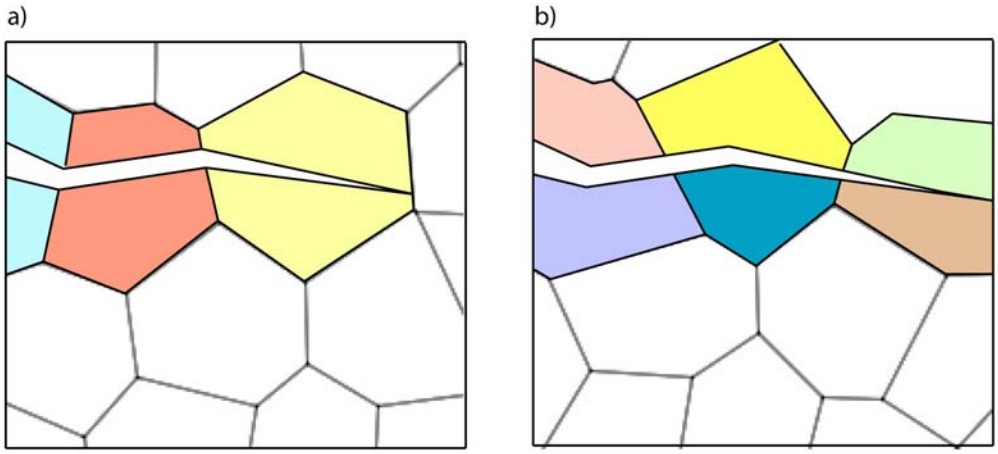

Figure **3-18**: Two different crack growth mechanisms that may be governing crack growth in the platinum films, with colors illustrating grain orientation. In the transgranular mechanism shown in part a), the grains across from the crack path will have the same orientation, suggesting that they were cleaved. In the intergranular mechanism shown in part b), the grains across from the crack path will have different orientation, suggesting they are separate grains. Note that the cracks in both these insets would have a crack profile which is indistinguishable when viewed by FE-SEM.

Chapter 4

Conclusions and Future Work

This final chapter of the thesis will detail the conclusions from this study. Following the conclusions, the final section will present suggestions for future work which may complement the findings of this study.

4.1 Conclusions

A study was conducted to determine the fatigue behavior of a nanocrystalline platinum thin film having a titanium adhesion layer. Microstructural analysis was performed on the samples to characterize their texture and crystallography. One tensile test and four constant stress amplitude fatigue tests were conducted on free standing platinum film specimens containing a central notch. Crack growth behavior and fracture toughness were evaluated from the fatigue tests. Following fracture of the specimens, fracture surfaces were examined with scanning electron microscopes to characterize the causes and mechanisms for the behavior.

1. Deposition conditions allow the fabrication of flat, 430nm platinum films having primarily (111) oriented columnar grains roughly 25-40 nm in diameter on a 20 nm titanium adhesion layer, in both a free-standing form and on top of a <100> oriented silicon chip. High-resolution TEM of the film established that the material was fully dense (i.e., no nanoscale voids or cracks were found) and no interphase regions between the grains were observed. Energy dispersive spectrometry (EDS), electron energy loss spectrometry (EELS) and secondary ion mass spectrometry (SIMS) of the film confirmed purity of the platinum structural film and the presence of a titanium adhesion layer. Additional spectra collected within the grains, along grain boundaries, near the Ti adhesion layer interface and

a top-down scan of the whole microstructure identified Platinum as the only element present, within the detectability limits of the techniques.

2. A tensile test performed at a rate of 0.1 μm per second was performed on centrally notched sample. An upper bound estimate for the ultimate tensile strength of the platinum using a calculation for the stress concentration of the notch was found to be 3.4 GPa. This upper bound value is consistent with nanoindentation studies [61] and tensile testing studies of the same films [23].The tensile strength value is more than order of magnitude higher than the microcrystalline value of 240 MPa [16] and even as an upper bound, indicates that the films are not inherently weak.

3. Constant stress amplitude (load ratio $\sigma_{min}/\sigma_{max} = R = 0.1$, sinusoidal waveforms at 1 Hz) fatigue tests were conducted on four samples in laboratory air (22±2°C). During the fatigue crack growth tests, cracks grew symmetrically from the notches and exhibited straight (i.e., nominally mode I) crack paths, and surface distortions associated with the development of the plastic zone were not observed. Final rupture of the specimens occurred on paths that were inclined 45° from the tensile loading axis after an unknown amount of stable, ductile tearing. An extremely limited range of stable fatigue crack growth was observed (< 2 MPa √m), and a least squares curve fit of the data to a power law relationship between the fatigue crack growth rate da/dN and the applied stress intensity factor range, ΔK, (i.e., $da/dN = C(\Delta K)^m$) provided a large power law exponent, m, of ~10.5. This power law exponent of the nanocrystalline platinum is significantly different from its polycrystalline value of ~3.5, and means that the nanocrystalline platinum's fatigue crack growth rate behavior is more similar to a ceramic or ordered intermetallic growth rate behavior than a pure metal.

4. The fracture toughness, K_q, estimated from K_{max} just prior to fracture ranged from 3.45 MPa √m to 4.88 MPa √m for the tested samples. The range of stable of

fatigue crack growth and fracture toughness were radically different from the behavior observed for micrograined platinum (K_q = 33.1 MPa √m) [46]. This nearly 10 fold reduction in K_q, is likely to be associated with the nanocrystalline microstructure of the thin films.

5. No crack closure was observed for nanocrystalline platinum. The linearity of the force-displacement plot which was carefully measured during the fourth fatigue test showed no indication of a significant change throughout the life of the fatigued sample. The lack of crack closure is indicative that intrinsic damage mechanisms are the dominant damage accumulation mode, despite a fatigue crack growth curve which is more similar to that of brittle materials where extrinsic toughening is dominant.

6. Scanning electron microscopy of the failure surfaces of the fatigue specimens revealed that the fatigue crack path from the near-threshold regime (i.e., growth rates below 10^{-9} m/cycle) up to ~2×10^{-7} m/cycle was *intergranular*, and secondary cracking was observed. As the cracks accelerated to ~3×10^{-7} m/cycle, they gradually transitioned to a transgranular path. During this transition, a fine ridge associated with localized (transverse) necking of the material developed in the center of the failure surfaces, parallel to the crack propagation direction. This transgranular mode with a central ridge persisted until final fracture occurred at K_{max} ~4 MPa √m. The observation of intergranular fatigue crack paths in a refractory, noble metal such as platinum demonstrates that fatigue crack growth mechanisms that operate in micrograined metals will not always persist as the grain size of the material is reduced to the nanoscale. This behavior may become more important as nanograined alloys are developed and the high strength of the grains further biases fatigue damage segregation to grain boundaries.

4.2 Recommendations for Future Work

The work presented in this thesis on nanocrystalline thin film platinum has shown evidence that platinum has fatigue properties more similar to ceramic and ordered intermetallics than its micrograined counterpart. More research is necessary in order to prove or disprove any of the mechanisms proposed in the previous section. As such, this section will provide several suggestions for experiments that could be run in order to complement the work presented in this thesis.

The frequency of fatigue should not be a factor in the crack growth rate in a non strain-rate dependent material such as platinum, assuming the properties of micrograined platinum. However, considering the substantial difference in fatigue properties observed in this study, and attributing those changes to the nanocrystalline microstructure, this assumption should be tested. In addition, the frequency of cyclic loading may be the easiest parameter to change with current system setup. Increasing the frequency and decreasing the driving force will also allow for testing at lower ΔK within reasonable timeframes (such that tests do not take months or years).

Investigating the relation between the velocity of crack advance and crack growth mechanism is another aspect that could benefit from additional testing. Running ΔK controlled tests should allow for the control of crack growth rates. This type of testing would require the implementation of real time predictions of crack length using compliance measurements. Although the coding might be somewhat difficult, the results will allow testing of the theory that crack growth rate is in direct relation to plastic deformation mechanism.

Variations in environment should not influence crack growth mechanisms in platinum significantly, as platinum is a noble metal strongly resistant to oxidation, however, Spediel's testing of microcrystalline platinum has shown some dependence on environment [55]. In addition, it may be the case that the results seen in this study are directly caused by platinum's natural oxidation resistance. Testing platinum's fatigue resistance under varying environments is another simple modification to the testing setup which can yield beneficial results. Varying the environment to include, for example, a

higher concentration of oxygen, may change crack closure and/or crack advance mechanisms and testing in vacuum, or a salt solution will allow for a direct comparison with Spediel's testing of micrograined platinum.

The results presented in this thesis are entirely restricted to the realm of nanocrystalline thin film platinum. Although comparisons can and were drawn regarding the nanocrystalline platinum and microcrystalline platinum, the results can not be easily compared with other material systems. One remedy to this would be to test other nanocrystalline thin films systems. Although numerous other such metallic systems can be tested, nanocrystalline thin film gold would make the best direct comparison, as gold and platinum share many mechanical properties, including crystal structure and oxidation resistance.

Bibliography

1. Smith, D.L., *Thin Film Deposition, Principles & Practice*. 1995: McGraw-Hill, Inc.

2. *The Opensource Handbook of Nanoscience and Nanotechnology*. 2007.

3. Horn, M., *Thin Film Deposition Class*. 2007.

4. Yeatman, E.M., *Design and performance analysis of thermally actuated MEMS circuit breakers.* Journal of Micromechanics and Microengineering, 2005. **15**(7): p. 109-115.

5. Larsen, K.P., Rasmussen, A.A., Ravnkilde, J.T., Ginnerup, M., and Hansen, O., *MEMS device for bending test: Measurements of fatigue and creep of electroplated nickel.* Sensors and Actuators, A: Physical, 2003. **103**(1-2): p. 156-164.

6. Hauptmann, P.R., *Selected examples of intelligent (micro) sensor systems: State-of-the-art and tendencies.* Measurement Science and Technology, 2006. **17**(3): p. 459-466.

7. Bell, D.J., Lu, T.J., Fleck, N.A., and Spearing, S.M., *MEMS actuators and sensors: Observations on their performance and selection for purpose.* Journal of Micromechanics and Microengineering, 2005. **15**(7): p. 153-164.

8. Allameh, S.M., Shrotriya, P., Butterwick, A., Brown, S.B., and Soboyejo, W.O., *Surface topography evolution and fatigue fracture in polysilicon MEMS structures.* Journal of Microelectromechanical Systems, 2003. **12**(3): p. 313-24.

9. Baghbanan, M., Erb, U., and Palumbo, G., *Towards the application of nanocrystalline metals in MEMS.* Physica Status Solidi (A) Applications and Materials, 2006. **203**(6): p. 1259-1264.

10. Rebeiz, G.M. *RF MEMS switches: status of the technology*. in *IEEE International Solid-State Sensors and Actuators Conference, 8-12 June 2003*. 2003. Boston, MA, USA: IEEE.

11. Newman, H.S. *RF MEMS switches and applications*. in *2002 IEEE International Reliability Physics Symposium Proceedings. 40th Annual, 7-11 April 2002*. 2002. Dallas, TX, USA: IEEE.

12. De Wolf, I. *The reliability of RF-MEMS: Failure modes, test procedures and instrumentation*. in *Reliability, Testing, and Characterization of MEMS/MOEMS III, Jan 26-28 2004*. 2004. San Jose, CA., United States: International Society for Optical Engineering, Bellingham, WA 98227-0010, United States.

13. Polcawich, R.G., Judy, D., Pulskamp, J.S., Trolier-McKinstry, S., and Dubey, M. *Advances in piezoelectrically actuated RF MEMS switches and phase shifters*. in *2007 IEEE MTT-S International Microwave Symposium, IMS 2007, Jun 3-8 2007*. 2007. Honolulu, HI, United States: Institute of Electrical and Electronics Engineers Inc., Piscataway, NJ 08855-1331, United States.

14. Polcawich, R.G., Pulskamp, J.S., Judy, D., Ranade, P., Trolier-McKinstry, S., and Dubey, M., *Surface Micromachined Microelectromechancial Ohmic Series Switch Using Thin-Film Piezoelectric Actuators.* IEEE TRANSACTIONS ON MICROWAVE THEORY AND TECHNIQUES, 2007. **55**(12).

15. *E8 - Standard Test Methods for Tension Testing for Tension Testing of Metallic Materials*, in *ASTM Standards*. 2002.

16. Callister, W.D.J., *Materials Science and Engineering, An Introduction*. Seventh Edition ed. 2007: John Wiley & Sons, Inc.

17. Soboyejo, W.O., *Mechanical Properties of Engineered Materials*. 2002: CRC.

18. Ritchie, R.O., *Mechanisms of fatigue-crack propagation in ductile and brittle solids.* International Journal of Fracture, 1999. **100**(1): p. 55-83.

19. Madou, M., *Fundamentals of Microfabrication*. 1997: CRC Press, LLC.

20. Ohmura, T., Matsuoka, S., Tanaka, K., and Yoshida, T., *Nanoindentation load-displacement behavior of pure face centered cubic metal thin films on a hard substrate.* Thin Solid Films, 2001. **385**(1-2): p. 198-204.

21. Tsuchiya, T., Hirata, M., Chiba, N., Udo, R., Yoshitomi, Y., Ando, T., Sato, K., Takashima, K., Higo, Y., Saotome, Y., Ogawa, H., and Ozaki, K., *Cross comparison of thin-film tensile-testing methods examined using single-crystal silicon, polysilicon, nickel, and titanium films.* Journal of Microelectromechanical Systems, 2005. **14**(5): p. 1178-1186.

22. Sharpe, W.N., Jr., Yuan, B., and Edwards, R.L., *A new technique for measuring the mechanical properties of thin films.* Journal of Microelectromechanical Systems, 1997. **6**(3): p. 193-9.

23. Sharpe, W.N., Jr., *ARO Symposium #3*. 2006.

24. Kumar, K.S., Van Swygenhoven, H., and Suresh, S., *Mechanical behavior of nanocrystalline metals and alloys.* Acta Materialia, 2003. **51**(19): p. 5743-5774.

25. Van Swygenhoven, H. and Weertman, J.R., *Deformation in nanocrystalline metals.* Materials Today, 2006. **9**(5): p. 24-31.

26. Weissmuller, J. and Markmann, J., *Deforming nanocrystalline metals: New insights, new puzzles.* Advanced Engineering Materials, 2005. **7**(4): p. 202-207.

27. Meyers, M.A., Mishra, A., and Benson, D.J., *Mechanical properties of nanocrystalline materials.* Progress in Materials Science, 2006. **51**(4): p. 427-556.

28. El-Sherik, A.M., Erb, U., Palumbo, G., and Aust, K.T., *Deviations from hall-petch behaviour in As-prepared nanocrystalline nickel.* Scripta Metallurgica et Materialia, 1992. **27**(9): p. 1185-1188.

29. Yim, T.H., Yoon, S.C., and Kim, H.S., *Tensile properties of electrodeposited nanocrystalline nickel.* Proceedings of the 12th International Conference on Rapidly Quenched & Metastable Materials, 2007. **449-451**: p. 836-840.

30. Ebrahimi, F., Ahmed, Z., and Li, H.Q., *Tensile properties of electrodeposited nanocrystalline FCC metals.* Materials and Manufacturing Processes, 2006. **21**(7): p. 687-693.

31. Siow, K.S., Tay, A.A.O., and Oruganti, P., *Mechanical properties of nanocrystalline copper and nickel.* Materials Science and Technology, 2004. **20**(3): p. 285-294.

32. Sanders, P.G., Eastman, J.A., and Weertman, J.R., *Elastic and tensile behavior of nanocrystalline copper and palladium.* Acta Materialia, 1997. **45**(10): p. 4019-4025.

33. Moser, B., Hanlon, T., Kumar, K.S., and Suresh, S., *Cyclic strain hardening of nanocrystalline nickel.* Scripta Materialia, 2006. **54**(6): p. 1151-1155.

34. Hugo, R.C., Kung, H., Weertman, J.R., Mitra, R., Knapp, J.A., and Follstaedt, D.M., *In-situ TEM tensile testing of DC magnetron sputtered and pulsed laser deposited Ni thin films.* Acta Materialia, 2003. **51**(7): p. 1937-43.

35. Cavaliere, P., *Strain rate sensitivity of ultra-fine and nanocrystalline metals and alloys.* Physica B, 2008. **403**(4): p. 569-75.

36. Kobiyama, M., Inami, T., and Okuda, S. *Mechanical behavior and thermal stability of nanocrystalline copper film prepared by gas deposition method*. in *5th International Conference on Nanostructured Materials (NANO 2000), 20-25 Aug. 2000*. 2001. Sendai, Japan: Elsevier for Board of Directors of Acta Metall.

37. *Matweb - searchable database of material properties*. 2008.

38. Cao, Y., Allameh, S., Nankivil, D., Sethiaraj, S., Otiti, T., and Soboyejo, W., *Nanoindentation measurements of the mechanical properties of polycrystalline Au and Ag thin films on silicon substrates: Effects of grain size and film thickness.* Materials Science and Engineering A, 2006. **427**(1-2): p. 232-240.

39. Sakai, S., Tanimoto, H., and Mizubayashi, H., *Mechanical behavior of high-density nanocrystalline gold prepared by gas deposition method.* Acta Materialia, 1998. **47**(1): p. 211-217.

40. Tokura, H., Window, B., Neely, D., and Swain, M., *Microstructure and mechanical properties of sputtered platinum films.* Proceedings of the 21st International Conference on Metallurgical Coatings and Thin Films, Apr 25-29 1994, 1994. **253**(1-2): p. 344-348.

41. Chasiotis, I., Bateson, C., Timpano, K., McCarty, A.S., Barker, N.S., and Stanec, J.R., *Strain rate effects on the mechanical behavior of nanocrystalline Au films.* Thin Solid Films, 2007. **515**(6): p. 3183-3189.

42. Wang, L. and Prorok, B.C., *Characterization of the strain rate dependent behavior of nanocrystalline gold films.* Journal of Materials Research, 2008. **23**(1): p. 55-65.

43. Samuel, B.A. and Haque, M.A., *Room temperature relaxation of freestanding nanocrystalline gold films.* Journal of Micromechanics and Microengineering, 2006. **16**(5): p. 929-934.

44. Stubbington, C.A. and Forsyth, P.J.E., *Some observations on microstructural damage produced by fatigue of aluminium-7.5% zinc-2.5% magnesium alloy at temperatures between room temperature and 250 C.* Acta Metallurgica, 1966. **14**(1): p. 5-12.

45. Suresh, S., *Fatigue of Materials*. Second ed. 1998: Cambridge University Press.

46. Witney, A.B., Sanders, P.G., Weertman, J.R., and Eastman, J.A., *Fatigue of nanocrystalline copper.* Scripta Metallurgica et Materialia, 1995. **33**(12): p. 2025-2030.

47. Vinogradov, A.Y., Stolyarov, V.V., Hashimoto, S., and Valiev, R.Z., *Cyclic behavior of ultrafine-grain titanium produced by severe plastic deformation.* Materials Science & Engineering A (Structural Materials: Properties, Microstructure and Processing), 2001. **A318**(1-2): p. 163-73.

48. Hanlon, T., Kwon, Y.-N., and Suresh, S., *Grain size effects on the fatigue response of nanocrystalline metals.* Scripta Materialia, 2003. **49**(7): p. 675-80.

49. Hanlon, T., Tabachnikova, E.D., and Suresh, S. *Fatigue behavior of nanocrystalline metals and alloys*. in *Fatigue Damage of Structural Materials V, Sep 19-24 2004*. 2005: Elsevier Ltd, Oxford, OX5 1GB, United Kingdom.

50. Hahn, H., Mondal, P., and Padmanabhan, K.A., *Plastic deformation of nanocrystalline materials.* Nanostructured Materials, 1997. **9**(1-8): p. 603-606.

51. Wolf, D., Yamakov, V., Phillpot, S.R., Mukherjee, A., and Gleiter, H., *Deformation of nanocrystalline materials by molecular-dynamics simulation: relationship to experiments?* Acta Materialia, 2005. **53**(1): p. 1-40.

52. Farkas, D., Van Swygenhoven, H., and Derlet, P.M., *Intergranular fracture in nanocrystalline metals.* Physical Review B (Condensed Matter and Materials Physics), 2002. **66**(6): p. 060101-1.

53. Farkas, D., Willemann, M., and Hyde, B., *Atomistic mechanisms of fatigue in nanocrystalline metals.* Physical Review Letters, 2005. **94**(16): p. 165502.

54. Wei, Y., Su, C., and Anand, L., *A computational study of the mechanical behavior of nanocrystalline fcc metals.* Acta Materialia, 2006. **54**(12): p. 3177-3190.

55. Speidel, M.O., *Resistance to Fatigue Crack Growth of the Platinum Metals.* Platinum Metals Review, 1981. **25**(1): p. 24-31.

56. *MinCryst - Crystallographic and Crystallochemical Database for Minerals and their Structural Analogues*. 2008.

57. Wilson, R.G., Stevie, F.A., and Magee, C.W., *Secondary Ion Mass Spectroscopy*. 1989: John Wiley & Sons.

58. *E 647 - Standard Test Method for Measurement of Fatigue Crack Growth Rates*, in *ASTM Standards*. 2005.

59. Laura, P.A., Reyes, J.A., and Rossi, R.E., *Numerical experiments on the determination of stress concentration factors.* Strain, 1974. **10**(2): p. 58-61.

60. Tada, H., Paris, P.C., and Irwin, G.R., *The stress analysis of cracks handbook*. 2000, New York: ASME Press.

61. Romasco, A., *Nanoindentation of Platinum Thin Films*, R. Meirom, Editor. 2008.

62. Agnew, S.R., Elliott, B.R., Youngdahl, C.J., Hemker, K.J., and Weertman, J.R., *Microstructure and mechanical behavior of nanocrystalline metals.* NSF Symposium on Micromechanic Modeling of Industrial Materials: In Honor of the 65th Birthday of Professor T. Mori, Jul 20-Jul 22 1998, 2000. **285**(1): p. 391-396.

63. Lin, H.T., Brady, M.P., Richards, R.K., and Layton, D.M., *Characterization of erosion and failure processes of spark plugs after field service in natural gas engines.* 15th International Conference on Wear of Materials, 2005. **259**(7-12): p. 1063-1067.

64. Christ, H.-J., *On the orientation of cyclic-slip-induced intergranular fatigue cracks in face-centred cubic metals.* Materials Science & Engineering A: Structural Materials: Properties, Microstructure and Processing, 1989. **A117**(1-2): p. 25-29.

65. Liang, F.-L. and Laird, C., *Control of intergranular fatigue cracking by slip homogeneity in copper. II. Effect of loading mode.* Materials Science & Engineering A (Structural Materials: Properties, Microstructure and Processing), 1989. **A117**: p. 103-13.

66. Liang, F.-L. and Laird, C., *Control of intergranular fatigue cracking by slip homogeneity in copper. I. Effect of grain size.* Materials Science & Engineering A (Structural Materials: Properties, Microstructure and Processing), 1989. **A117**: p. 95-102.

67. Zhang, Z.F. and Wang, Z.G., *Dependence of intergranular fatigue cracking on the interactions of persistent slip bands with grain boundaries.* Acta Materialia, 2003. **51**(2): p. 347-64.

68. Liu, W., Bayerlein, M., Mughrabi, H., Day, A., and Quested, P.N., *Crystallographic features of intergranular crack initiation in fatigued copper polycrystals.* Acta Metallurgica et Materialia, 1992. **40**(7): p. 1763-71.

69. Tromans, D. and Ruhong1, S., *Intergranular/transgranular fatigue of copper: influence of environment on crack path and propagation rates.* Materials Science & Engineering A (Structural Materials: Properties, Microstructure and Processing), 1996. **A219**(1-2): p. 56-65.

70. Noskova, N.I., *Deformation of nanocrystalline pure metals and alloys based on Fe and Al.* Journal of Alloys and Compounds, 2007. **434-435**(SPEC ISS): p. 307-310.

71. Nieman, G.W., Weertman, J.P., and Siegel, R.W., *Mechanical behavior of nanocrystalline metals.* Nanostructured Materials, 1992. **1**(2): p. 185.

72. Caruana, D.J. and Bannister, J.V., *Surface properties of fractured and polished platinum microelectrodes.* Journal of Electroanalytical Chemistry, 1997. **424**(1-2): p. 197-205.

Appendix A

Schematic of Inclined Adapter Plate

3D view

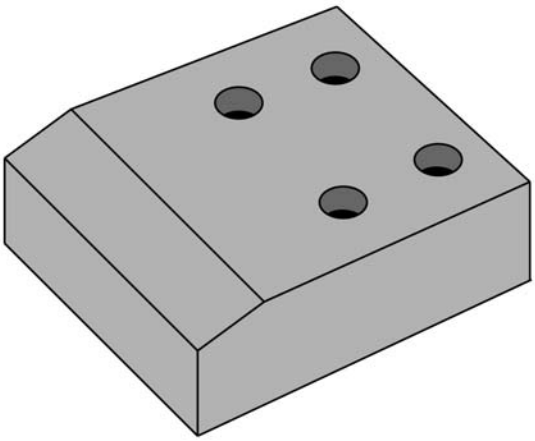

Material: Aluminum
Purpose: Inclined adapter gate
A = countersunk throughhole for screw dimensions noted below

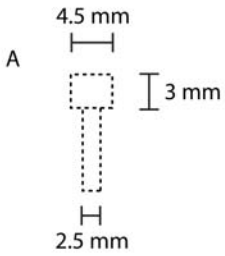

Side view

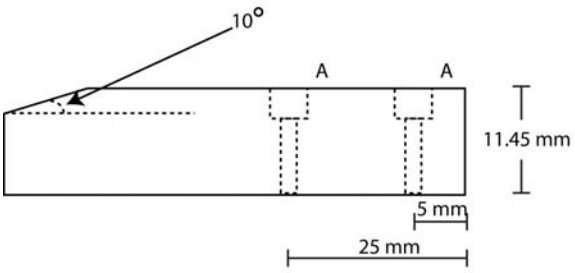

Top view

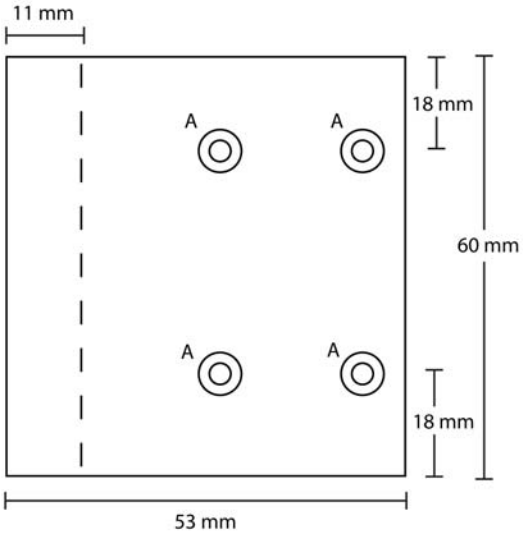

Appendix B

Schematic of Vertical FE-SEM Stub

3D view

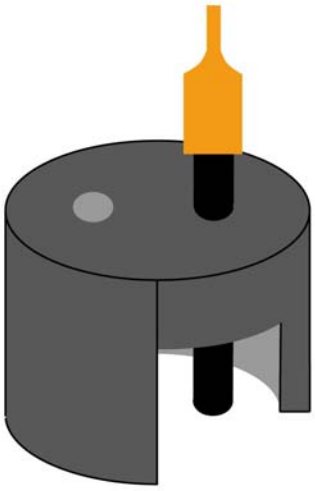

Material: Aluminum
Purpose: 90 degree FE-SEM Stub
All drilled holes are thru holes

Custom drill bits purchased for .25mm radius holes.

Side view

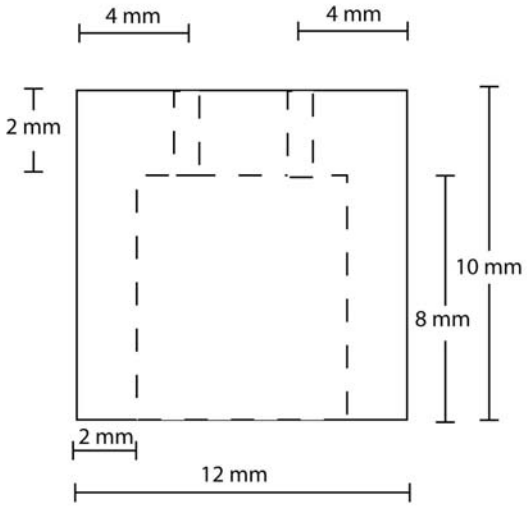

Top view